Light emitting microstructures in porous silicon

Squire, E. K.

Award date:
1999

Awarding institution:
University of Bath

LIGHT EMITTING MICROSTRUCTURES IN POROUS SILICON

Submitted by E.K. Squire

for the degree of

Doctor of Philosophy

of the University of Bath

1999

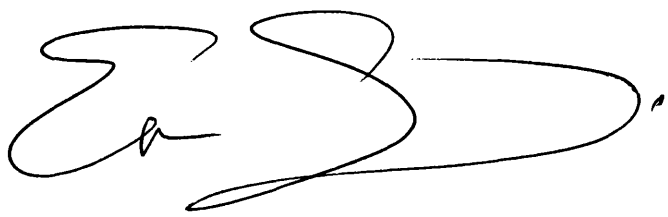

ProQuest LLC
789 East Eisenhower Parkway
P.O. Box 1346
Ann Arbor, MI 48106-1346

Abstract

Experimental and theoretical techniques are used to examine microstructuring effects on the optical properties of single layer, multilayer, single and multiple microcavity structures fabricated from porous silicon. Two important issues regarding the effects of the periodic structuring of this material are discussed. Firstly, the precise role played by this microstructuring, given that the luminescence is distributed throughout the entire structure and the low porosity layers are highly absorbing at short wavelengths. The second issue examined concerns the observed effects on the optical spectra of the samples owing to the emission bandwidth of the material being greater than the optical stopband of the structure.

Measurements of the reflectivity and photoluminescence spectra of different porous silicon microstructures are presented and discussed. The results are modelled using a transfer matrix technique. The matrix method has been modified to calculate the optical spectra of porous silicon specifically by accounting for the effects of dispersion, absorption and emission within the material. Layer thickness and porosity gradients have also been included in the model. The dielectric function of the two component layers (i.e. silicon and air) is calculated using the Looyenga formula. This approach can be adapted to suit other porous semiconductors if required.

Examination of the experimental results have shown that the emitted light is strongly controlled by the optical modes of the structures. Furthermore, the data display an interplay of a wide variety of effects dependent upon the structural composition. Comparisons made between the experimental and calculated reflectivity and photoluminescence spectra of many different porous silicon microstructures show very good agreement.

Contents

Journal Publications

The following papers have been published in refereed journals arising from the work presented in this thesis.

1. E.K. Squire, P.A. Snow, P.St.J. Russell, "Light Emission from Porous Silicon Single and Multiple Cavities", Conference proceedings, *to be published in the Journal of Luminescence*, (1998).

2. E.K. Squire, P.A. Snow, P.St.J. Russell, "Optimising Light Emission from Layered Porous Silicon Structures", *Applied Optics*, **37**, 7107, (1998).

3. E.K. Squire, P.A. Snow, P.St.J. Russell, "Light Emission from Highly Reflective Porous Silicon Multilayered Structures", Conference Proceedings, *to be published in the Journal of Porous Materials*, (1998).

4. P.A. Snow, E.K. Squire, P.St.J. Russell, "Light Emission from Porous Silicon Single and Multiple Cavities", *Optics and Photonics News*, (1998).

5. P.A. Snow, E.K. Squire, P.St.J. Russell, "Vapour Sensing Using The Optical Properties of Porous Silicon Bragg Mirrors", *submitted to the Journal of Applied Physics*, (1998).

Conference Presentations

The following papers have been presented at national and international conferences arising from work presented in this thesis.

1. E.K. Squire, P.A. Snow, P.St.J. Russell, "Design of a Porous Silicon Resonant Cavity for Enhanced Light Emitting Diode Performance", *Symposium on Optical Composites*, Conference sponsored by the Rank Prize Funds, Grasmere, (1996).

2. E.K. Squire, P.St.J. Russell, P.A. Snow, "The Design of High Performance Porous Silicon Light Emitting Diodes Using a Photonic Band Gap Approach", *IEE Conference*, London, (1996).

3. E.K. Squire, P.A. Snow, P.St.J. Russell, "The Design of Efficient Porous Silicon Light Emitting Diodes Using a Photonic Band Gap Approach", *Semiconductor and Integrated Optics Conference*, Cardiff, (1997).

4. E.K. Squire, P.A. Snow, P.St.J. Russell, "Experimental Characterisation of Efficient Porous Silicon Light Emitting Structures", *National Quantum Electronics Conference*, Cardiff, (1997).

5. P.A. Snow, E.K. Squire, P.St.J. Russell, "Light Emission from Porous Silicon Single and Multiple Cavities", *EMRS meeting*, Strasbourg, (1998).

6. P.A. Snow, E.K. Squire, P.St.J. Russell, "Light Emission from Highly Reflective Porous Silicon Multilayered Structures", *Porous Semiconductors - Science and Technology Conference*, Majorca, (1998).

7. P.A. Snow, E.K. Squire, P.St.J. Russell, "Porous Silicon Mirrors: Structural

Colour from Silicon", *Optical Design in Nature*, Bath, (1998).

8. P.A. Snow, E.K. Squire, P.St.J. Russell, "Light Emission in Periodically Microstructured Porous Silicon", *CLEO/Europe-EQEC*, Glasgow, (1998).

Acknowledgements

I would like to convey my thanks to the following:

Paul Snow for his support and encouragement over the past three years.

Tim Birks, Peter Huggard and Philip St.J. Russell for their many helpful discussions.

Leigh Canham for both the provision of the porous silicon samples and for all his useful comments and suggestions.

Professor S. Kawakami of the Research Institute of Electrical Communication, Tohoku University, Japan, for the provision of a sample.

The Engineering and Physical Science Research Council for funding my research over the course of my PhD.

The Defence Evaluation and Research Agency for their support.

My family who have provided all the support and financial backing I've ever needed and who have always maintained their faith in me.

Finally, I'd like to thank everybody at the Golden Fleece for providing such a friendly pub to go home to through all eight years of my student life.

Chapter 1

Introduction

For many years silicon has been the dominant material used in the microelectronics industry. However, owing to its poor light emission characteristics, it has been rejected for use as an optoelectronic material in favour of semiconductors with greater luminescence efficiencies. Until the start of this decade, it had not been possible to obtain efficient room temperature luminescence from silicon. The demonstration by Canham in 1990 [1] that a porous form of silicon can emit brightly in the visible spectrum marked a turning point in silicon device research.

Porous silicon (p-Si) is not a new material. The first reported fabrication was made over forty years ago by Uhlir [2] during investigations into the electropolishing of silicon in hydrofluoric acid (HF). On examination of silicon wafers after etching, it was noted that the wafer surfaces had often developed a dark deposit. This was tentatively supposed to be a silicon oxide, and thus remained unexplored. Further interest in p-Si was limited until the 1980s when its potential for use in device fabrication was first realised. Interest then concentrated on utilising its very large surface area and associated fast oxidation rate as a means to electrically isolate regions of circuitry using the FIPOS (Full Oxidation by Porous Oxidised Silicon) process [3]. Canham's discovery triggered a worldwide research effort, with work primarily being aimed at establishing the luminescence mechanism of p-Si, and using this light emission with the aim of fully integrating p-Si optoelectronic devices with existing silicon technology.

In recent years, p-Si light emitting devices have used microstructuring, e.g. the

layering of alternating high and low index material to form a multilayer stack, as a means of controlling and enhancing spontaneous emission from the material. Generally, multilayer structures are used within many optical devices including high reflectivity mirrors, filters and vertical cavity surface emitting lasers (VCSELs). In the first two cases, the structure can be considered passive, i.e. it does not emit light. In the latter, light emission occurs from a central active cavity layer enclosed between two passive mirrors. In p-Si light emitting structures of similar design to VCSELs, emission is no longer confined to the central region. Instead, due to the emission characteristics of p-Si, luminescence can occur throughout the whole structure.

An important issue not yet fully discussed in the literature is the precise role played by the periodic structuring of p-Si, given (a) that the luminescence is physically distributed over many layers, and (b) that silicon is highly absorbing at short visible wavelengths. These effects must be given consideration if optimised designs for different applications are to be produced.

1.1 Summary of Thesis Contents

This report presents work carried out by the author over the past three years to gain a better understanding of the optical properties of p-Si layered structures. It was motivated by the need to develop a greater knowledge of how to control light emission and propagation in multilayered p-Si structures currently being examined for use in optoelectronic applications.

In order to address these issues, this work has been divided between computer modelling and experimental studies of different p-Si structures. Approaching the problem from these two different perspectives allows a more complete picture to be obtained and thus the best means of optimising device designs.

Computer modelling is used for two purposes. The first is to aid in the design of different p-Si microstructures by predicting the optical characteristics of each design. Once the samples have been fabricated, comparisons made between spectra obtained from experimental measurements and modelling calculations are used to examine the accuracy and validity of the assumptions made in the modelling pro-

cess. The second purpose of the modelling is to compare the relative efficiencies of a variety of more complex structures. Using this method, much valuable information can be learnt regarding the effects of different structures on the propagation of light within them, quickly and without the need for fabrication.

The first chapter of this thesis gives an introduction to the fabrication, structure and light emission characteristics of p-Si. It will be shown that although the fabrication process is relatively simple, changes to the etch parameters can have a large effect on the morphology of the produced porous layer. This, in turn, will alter the optical properties of the structure. Next, the origin of the p-Si luminescence bands, and their different attributes will be discussed. Finally, a more detailed examination of the visible band luminescence will be given. An explanation why this band is of the most technological importance to p-Si devices will be given.

Chapter two describes in general terms how the light emission characteristics of a material can be altered through periodic microstructuring. Both multilayer mirror and microcavity fabrication and theory will be discussed both generally and with reference to p-Si. Finally, a brief summary of recent experimental results regarding emission control in p-Si cavity structures will be given.

Chapter three shows the method used to model the optical spectra of p-Si single and multilayered structures. This includes the determination of the dielectric function of bulk silicon across the wavelength range of interest, and the subsequent determination of an effective dielectric function which represents the properties for a porous layer, i.e. one composed of silicon and voids. Next, the Fabry-Pérot equations and transfer matrix method used to calculate the reflectivity and transmission of an incident light wave through a single layer and multilayer structure respectively are described. Methods to make the computer model more realistic, i.e. able to account for the absorption and emission of light, are then discussed. Finally, a modelling comparison between the relative emission efficiencies of four different p-Si structures is discussed.

Chapter four discusses the results of experimental reflection and transmission measurements carried out on different p-Si multilayer structures and an amorphous silicon/silica multilayer structure respectively. Experimental and calculated spectra for each different sample are displayed and compared. Differences

between spectra obtained from p-Si samples fabricated using different etch parameters are discussed. Discrepancies between predicted and experimental spectra of the silicon/silica structure are shown to be due to the sample layer thickness and composition being different to that specified in the original design. The use of the model to determine more accurately the actual layer parameters is shown.

Chapter five displays and discusses the experimental and calculated photoluminescence results obtained from different p-Si single and multilayer structures. Comparisons are made between the calculated and experimental data for each structure, and the experimental spectra of samples relative to each other. These results are used to examine the effect that each different microstructure has on the emission and propagation of light from it. Suggestions for making the structures more efficient are given.

Finally, chapter six gives a summary of the work presented and examines what conclusions may be drawn from the results obtained.

1.2 Introduction to Chapter One

This chapter provides an overview of the p-Si fabrication process, followed by an examination of the structural and optical properties of the obtained porous layers. Firstly, light emission from crystalline silicon (c-Si) is discussed, and the poor luminescence efficiency compared to other semiconductor materials is explained. Next, the fabrication equipment and techniques for preparing p-Si are described. It will be shown that changes to the etch parameters, e.g. resistivity of the wafer, or current density, can produce vastly different structures, the morphology of which will then be described. Finally, proposed explanations of possible mechanisms for light emission from p-Si will be discussed. It will be seen that whilst one model currently stands out from the rest, there still remain experimental details which have not yet been fully explained.

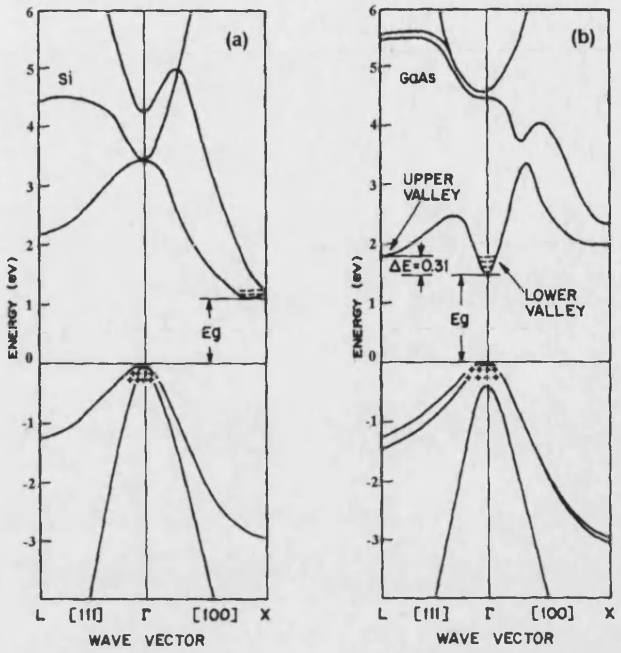

Figure 1.1: Band structure diagrams of (a) an indirect gap semiconductor, Si, and (b) a direct gap semiconductor, GaAs. [5]

1.3 Bulk Silicon Light Emission

Owing to its very poor luminescence characteristics, undoped bulk crystalline silicon (c-Si) has been rejected for use in active optical devices in favour of more efficient light emitting semiconductor materials, e.g. gallium arsenide (GaAs). The variation between the relative luminescence efficiencies of semiconductor materials arises due to differences between their electronic band structures.

In a semiconductor, luminescence occurs when an electron and hole undergo radiative recombination. The emitted photons will have negligible momentum, and if the recombining carriers are situated at the band edge, they will have an energy equal to the band gap energy. In a direct gap semiconductor, e.g. GaAs, the electron and hole are located in the same point in momentum space, i.e. the conduction band minimum and valence band maximum occur at the same point (see fig1.1b). These conditions result in a large radiative recombination rate and hence short radiative lifetime, as shown by Fermi's golden rule [4].

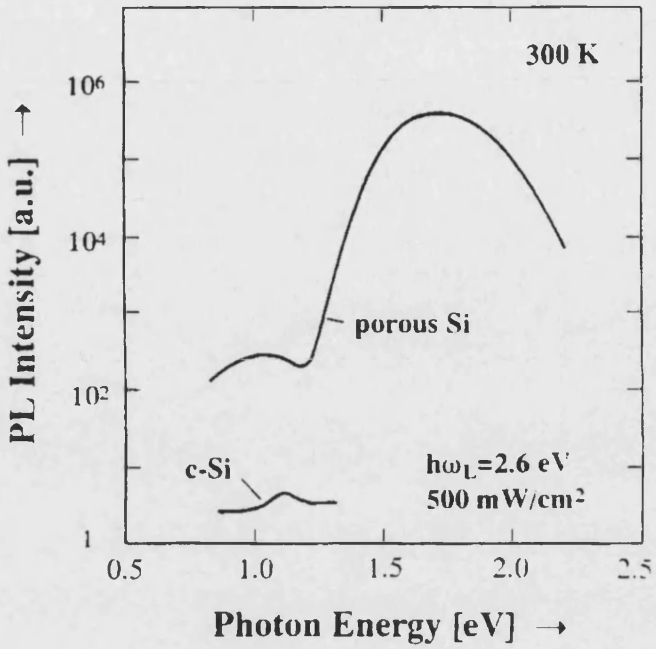

Figure 1.2: Comparison of room temperature photoluminescence spectra of c-Si and p-Si. Note the logarithmic scale. [7]

Silicon has a band gap of size ~ 1.12eV at 300K, and is an indirect gap material, i.e. carriers are located at the band minima at different points in momentum space (see fig 1.1a). In this instance, recombination can only occur with phonon assistance providing the necessary momentum conservation. The probability of this three body event occurring is less than that of direct recombination and hence the radiative recombination lifetime will be much longer. Because of this, typically before radiative recombination can occur the conduction band electron will recombine non-radiatively, for example, by Auger recombination.

The internal luminescence efficiency of a material, η, is defined as,

$$\eta = \frac{\tau_{nonrad}}{\tau_{nonrad} + \tau_{rad}}, \tag{1.1}$$

where τ_{nonrad} is the non-radiative recombination lifetime and τ_{rad} is the radiative recombination lifetime [6]. It can be seen from equation 1.1 that the light emission efficiency of direct gap semiconductors (>1%) is greater than that of indirect gap materials (e.g. $\eta_{silicon} \sim 10^{-5}\%$) [6] because the radiative recombination rate is

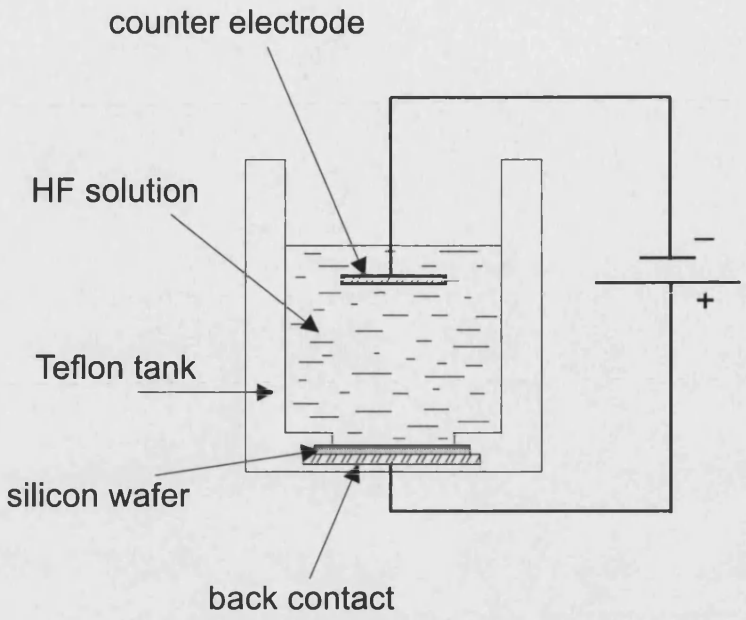

Figure 1.3: Schematic view of the electrochemical cell used to etch p-Si [8]

much higher than that of non-radiative recombination.

Figure 1.2 shows a comparison between the photoluminescence (PL) intensity of c-Si and p-Si layers. It can be seen that the PL from p-Si can be up to six orders of magnitude greater than that from c-Si, with the p-Si emission peak occurring at an energy ~0.5 eV higher than that of the c-Si spectra (E_g ~1.12 eV). As discussed above, the efficiency and energy of c-Si light emission is governed by the indirect nature and size of its band gap respectively. Section 1.6 examines why the emission characteristics of p-Si are so different.

1.4 Fabrication

A schematic view of the equipment required to fabricate p-Si is shown in figure 1.3. A p or n doped silicon wafer with a metallic back contact is placed in a HF resistant container made of Teflon. The wafer itself acts as one electrode, whilst a platinum electrode is placed in an aqueous HF solution. The HF etchant is mixed with a wetting agent, e.g. ethanol, which aids the penetration of the fluid into the pores thus increasing layer uniformity.

On application of a current through the system, pore growth will be initiated providing certain conditions are met [9]. The first condition requires the silicon to supply holes to the etch front which are then are consumed in the electrochemical reaction. To achieve this, the wafer must be correctly biased. The diode like behaviour of the wafer/HF contact is described by the terms forward (anodic) and reverse (cathodic) biasing. For example, when etching heavily doped p type material, the wafer must be forward biased so that holes are drawn to the surface. When etching n doped or lightly p doped material, illumination of the wafer is required to generate holes.

The second condition for dissolution is that the current density is below a critical value, J_{crit}. If $J > J_{crit}$, thus violating this condition, the dissolution reaction is limited by mass transfer to the HF, thus allowing holes to cluster on the surface. This will result in electropolishing. This process levels the surface of the silicon wafer by preferentially etching at the raised areas on the wafer face. If $J < J_{crit}$ the dissolution reaction is instead controlled by charge transfer in the wafer and hole depletion at the wafer surface. In this case the electric field distribution at the surface will result holes being channelled preferentially into regions of surface irregularity, e.g. defects. Pore growth will thus initiate in these areas and continue until hole depletion prevents further etching.

The exact mechanism responsible for the method of hole depletion at the etch front is not yet fully understood. Of the models proposed thus far, the view of Lehmann and Gösele has gained majority acceptance [10]. They propose that there are two separate means by which the supply of holes becomes depleted at the silicon/HF interface. The first, which results in the formation of larger pores, is governed by the width of the depletion region formed when holes are consumed by the etch. This in turn is dependent on the substrate doping. Overlapping of the depletion regions formed on the pore walls will inhibit hole transfer to these areas. The walls will thus become passivated from further attack whilst the etch continues at the pore tips.

The second mechanism for hole depletion places a lower limit on pore size and is governed by quantum effects. As discussed in section 1.6, the electronic band gap of p-Si is increased with respect to that of c-Si due to quantum confinement effects. Thus, in order to penetrate from the silicon wafer into the porous layer, the holes require an additional energy E_q (figure 1.4). If E_q is greater than the

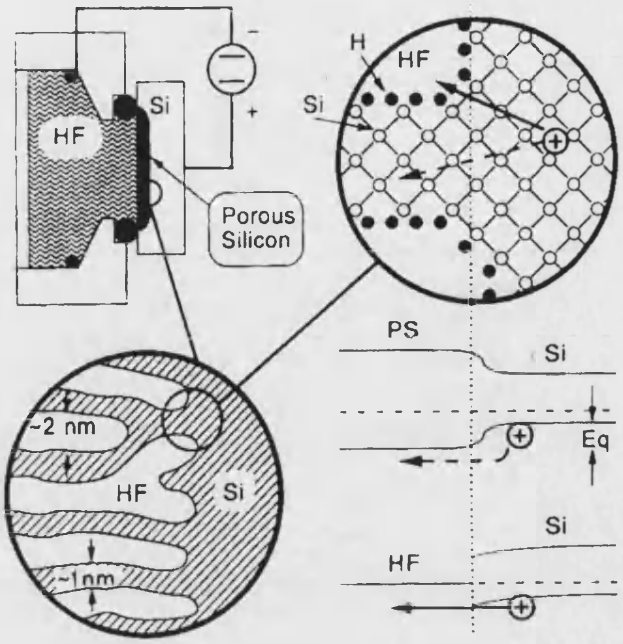

Figure 1.4: Schematic view of p-Si etching equipment (upper left), the specific processes involved in the etch at the pore tips (lower left and upper right), and the corresponding band diagram for the silicon/ electrolyte and silicon/p-Si transitions (lower right) [9]

energy of the holes, the p-Si interface region will become depleted and etching will cease. Both these hole depletion mechanisms are independent of each other but are able to co-exist, resulting in the formation of several different pore sizes dependent on substrate doping (section 1.4.1).

The best method of characterising a p-Si layer is by reference to its porosity. The porosity is defined as the percentage of voids within the material layer, i.e. a 70% porous material will consist of 70% void and 30% solid. It is important to note that the porosity depends on both pore size and density. Hence, the same overall porosity can arise from relatively few large pores or a greater number of densely packed small pores.

Figure 1.5 shows the dependence of the layer porosity on the applied current density for p-, p and p+ type p-Si layers [11]. It can clearly be seen that layers of greater porosity, i.e. a greater percentage of voids, will be obtained using higher current densities during the etch. This figure also shows that there is a

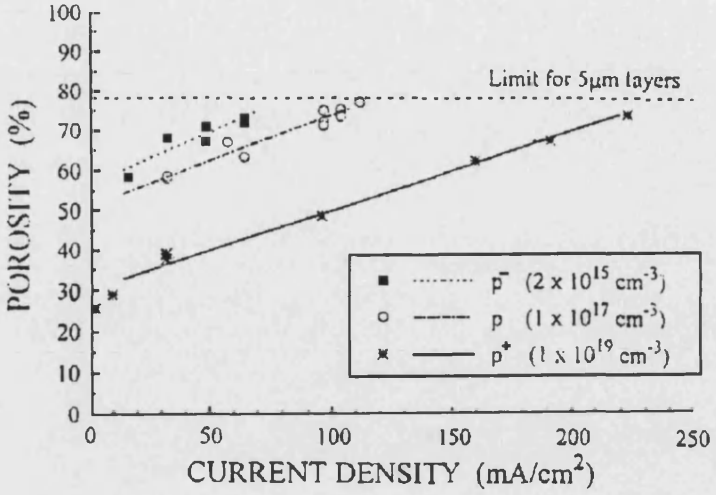

Figure 1.5: The porosity of p-, p and p+ type wafers of p-Si, as a function of applied current density [11].

wide variation in the porosity range obtainable with different resistivity wafers ranging from 60-75% for a p- substrate, to 30-75% for a p+ substrate. It is important to note that as the porosity grows the average refractive index of the layer will change as the two media are mixed. This point will be discussed further in section 3.3.2.

Both the above points are of great importance when designing p-Si multilayer structures, as switching of the current density as the etch progresses allows layers of different porosity, and hence refractive index, to be grown on top of each other. The fabrication and optical properties of structures will be discussed in chapters 2 and 3.

The value of current density is not the only etch parameter to determine the p-Si layer characteristics. Other factors include the HF concentration, the etch time and the substrate doping. The HF concentration has an important effect on the pore size, i.e. as the concentration decreases the porosity of the etched layer is found to increase [12]. The etch time controls the overall layer thickness, i.e. layers etched for a longer amount of time will be thicker. One consequence of long etch times, i.e. of the order of a few minutes, are the formation of porosity gradients within the sample, i.e. a non-uniformity of the porosity with depth. This can be a problem when etching larger structures and will be discussed further

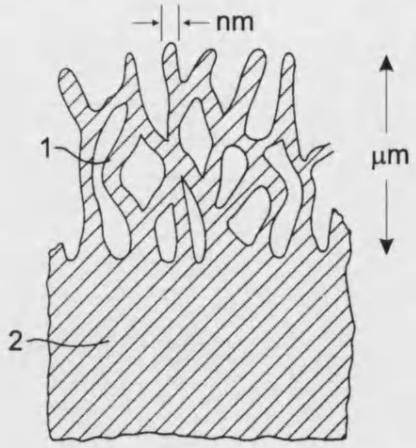

Figure 1.6: Schematic view of etched p-Si layer. The wires (1) have nm dimensions, whilst the layer thickness is of the order of a few μm. The layer is etched from a bulk silicon substrate (2) [9].

in section 2.4.

A further problem to be considered during fabrication is the degree of interface irregularity obtained from substrates of different doping levels. The roughness of the p-Si layer/substrate interface in p- and p+ doped material has been studied in detail by Lérondel [13]. His results showed the existence of two types of layer thickness oscillations, one on a millimetre scale (waviness), and the other on a micrometer scale (roughness). Whilst waviness was found to occur in both p- and p+ p-Si layers, the roughness contribution was only significant in p- layers. Both types of inhomogeneity show a linear increase in oscillation amplitude with dissolution time, and are believed due to current density fluctuations during fabrication. The occurrence of the roughness oscillations on a scale comparable with the wavelength of light means that it can cause significant scattering of light at the layer interfaces. It will be demonstrated in chapters 4 and 5 that scattering due to interface roughness in p- structures can have a significant effect on their reflectivity and PL spectra.

1.4.1 Effects of Substrate Doping on Pore Morphology

After etching, the material remaining in a p-Si layer forms a sponge-like network of silicon wires (figure 1.6). The exceptions to this structural formation are

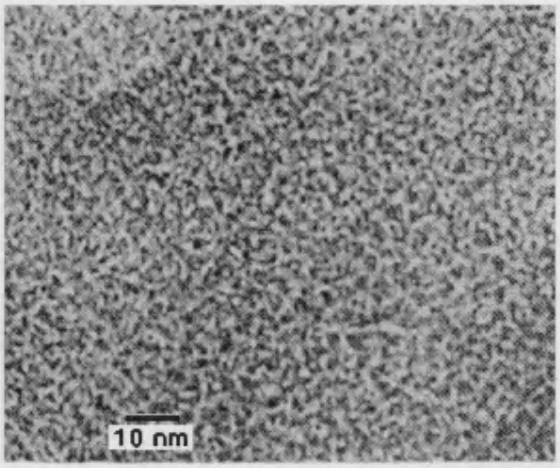

Figure 1.7: TEM image of a p-Si layer obtained by etching a p- type substrate [15].

the ordered arrays fabricated from n- substrates as discussed below. Table 1.1 shows how p-Si pore sizes are classified into three different classes, as set by the International Union of Pure and Applied Chemistry (IUPAC).

Pore type	Pore size
Microporous	< 2 nm
Mesoporous	2-50 nm
Macroporous	> 50 nm

Table 1.1: Pore size classification as given by IUPAC [14].

One of the most important factors affecting the final structural morphology is the type and resistivity of the initial c-Si wafer. P-Si layers etched from p+, n+ or n- substrate types show a distribution of pore sizes, e.g micropores and mesopores coexist in the same layer. However, wholly microporous structures can only be fabricated from p- substrates. Figure 1.7 shows a TEM picture of a p-Si layer etched from p- material. The image shows a cross section of pores of width ~3-5 nm forming a structure resembling coral. X-ray diffraction experiments have confirmed the remaining material to be composed of crystalline silicon.

Mesoporous structures are obtained by etching p+ and n+ substrates. Small angle scattering of X-rays and diffraction experiments show that the structure of p+ p-Si is strongly anisotropic [16] and crystalline [17]. TEM observations of p+ layers of porosities ranging from 31% to 79% by Beale *et al.* show long pores running perpendicular to the surface with widths of ~10 nm [18]. The pores themselves

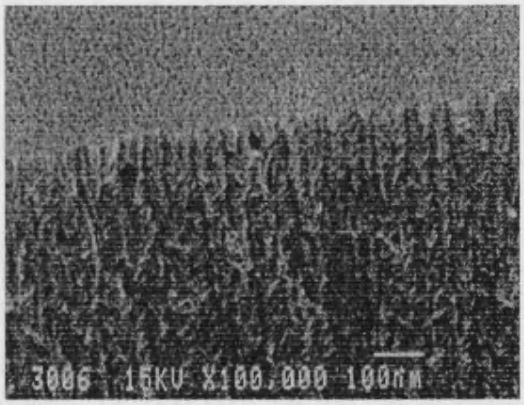

Figure 1.8: TEM image of a p-Si layer obtained by etching a p+ type substrate [18].

are heavily branched and exhibit a characteristic fir tree configuration. Figure 1.8 shows a typical TEM image of a p+ p-Si layer.

The etching of n- doped material leads to the formation of macropores. The pores may be randomly initiated or etching can be made to occur at set positions using pre-etched pits [19]. Using the latter technique highly ordered arrays of deep holes can be formed. Suggested applications for such structures include their use as photonic crystal waveguides [20]. Due to the large size of the pores, SEM can be used to examine these structures. Figure 1.9 shows an example of a macropore array formed from lithographically defined pits. The pores, up to 100 nm in diameter, can be seen to penetrate in a direction normal to the surface.

1.5 Mechanical Stability and Drying

After an etch has been completed it is necessary to ensure that the etching solution is removed from the pores. Normally, this is carried out by simply allowing the solution to evaporate in air at room temperature and pressure. This method is adequate for low to mid porosity (~55%) layers. The drying of high porosity (70%) layers by under these conditions can lead to cracking, peeling and even total disintegration of the layer due to a lack of mechanical stability. It is believed that the dimension of the pore walls may be more important than the overall porosity itself when determining the layer stability, and it has been shown that smaller skeletal sizes are more prone to break apart [21].

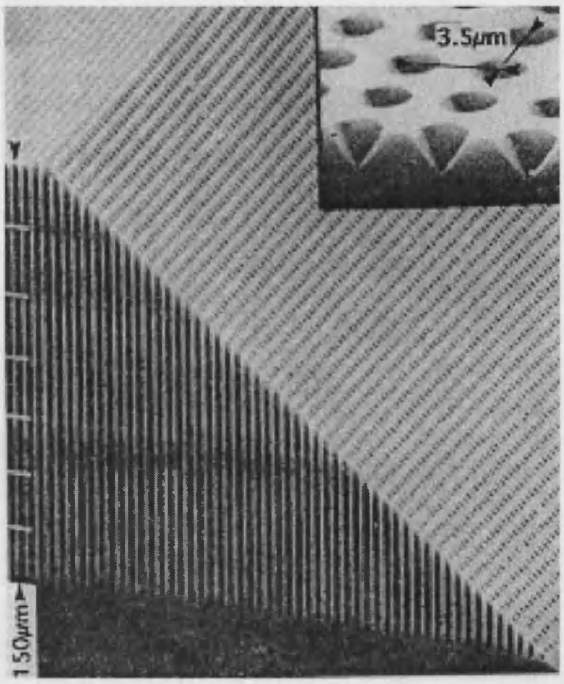

Figure 1.9: SEM image of a p-Si structure obtained from etching a n- type substrate which had pre-etched pits (shown in inset) [19].

This cracking of high porosity layers, caused by excessive capillary forces at the fluid/air interface within the pore, can be circumvented by supercritically drying the layer. This technique avoids the interface between the fluid and gas phase by removing the pore liquid above its critical point, thus removing capillary forces. Ultrahigh porosities, in excess of 95% have been achieved using this method [22].

1.5.1 Surface Passivation

The internal surface area of a p-Si film is exceptionally large, typically between 200-600 m^2cm^{-3} [23]. After etching, a surface rich in hydrogen bonds in the form $Si - H_x$ (x=1,2,3), is routinely observed using IR absorption spectroscopy [12][24]. However, the surface is also considerably more reactive than that of bulk silicon. If stored in ambient air, immediately after etching the chemical species present on this surface will change. The freshly etched layer will react with the air to oxidise the surface, and as a result Si-O-Si bonds can be observed in IR spectra. The aging process starts immediately after anodisation, its progression dependent upon the wafer environment. If left untreated, total oxidation of the

surface will be apparent after 1 year [14]. This effect is especially pronounced for high porosity layers due to their larger internal surface area [25].

It is important to note that through the careful control of p-Si surface passivation, it is possible to stabilise its luminescence. Stabilisation can be achieved through the high temperature oxidation of the p-Si sample in an atmosphere containing a small percentage of oxygen, to produce a very thin oxide layer [26]. After etching of the layer, the oxidation process is used to replace the fragile Si-H bonds present on the surface with more stable Si-O bonds. This oxidised material called, silicon-rich silicon oxide, can subsequently made into stable and efficient light emitting devices. Given the high surface area in p-Si, it is reasonable to expect that the surface will exert important effects on the optical behaviour. This will be discussed further in section 1.6.

1.6 Luminescence from Porous Silicon

1.6.1 Introduction

The demonstration in 1990 [1] that p-Si exhibits efficient luminescence in the visible spectrum at room temperature triggered much research aimed at establishing the emission mechanism. Such interest arose because, a) the development of p-Si light emitting devices for integration with existing silicon technology would extend the functionality of silicon from microelectronics into optoelectronics [14], b) p-Si can be fabricated quickly and at low cost, and c) there was a desire to establish the reason why p-Si luminescence is many orders of magnitude more efficient than that of c-Si.

As shown in section 1.3, bulk silicon displays very weak luminescence because the indirect nature of its band gap results in non-radiative recombination dominating over radiative recombination. In contrast, p-Si structures display luminescence across a broad wavelength range from the near infrared (IR) to the near ultraviolet (UV). This emission arises from four distinct luminescence bands of different origin. These bands, labelled as the UV, fast (F), slow (S), and IR bands are summarised in table 1.2. Of these bands, the S band has been the subject of the

Band Name	Peak Wavelength (nm)	Key properties
UV	$\sim$ 350	Weak porosity dependence Fast decay time (ns) Observed in oxidised material
F	$\sim$ 470	Same as UV
S	400-800	Strong porosity dependence Sensitive to surface passivation Slow decay time (μs)
IR	1100-1500	Observed in oxidised material Weak PL compared to visible spectra

Table 1.2: Summary of key features of photoluminescence bands

most research due to its technological significance. The main characteristic of this band is that changes to the p-Si layer porosity allow the emission wavelength of the material to be tuned across the visible spectrum from 400-800 nm [1]. The main features of the S band will be described in further detail in the following section. For completeness, a general overview of the properties of the remaining three bands will be given first.

The initial report of weak but fast ($\tau \sim$ ns) luminescence from the F band was made in 1992 by Harvey *et al.* [27]. The authors attributed the luminescence to direct transitions in c-Si nanocrystallites. Several more recent studies have shown that F band luminescence is only observed from oxidised samples. The samples investigated had been prepared by many different methods including artificial oxidation by chemical immersion in HNO_3 and by rapid thermal oxidation [6]. It has thus been concluded that the luminescence is likely to originate in the oxide itself, not from small crystallites [14]. Room temperature time resolved PL data showing the existence of this band are displayed in figure 1.10. The S and F bands were differentiated by choosing the period of the pumping laser pulse to be much smaller than the decay lifetime of the slow band, and much larger than the lifetime of the fast band.

UV luminescence from oxidised p-Si was first reported by Jiang *et al.* in 1993 [29]. This emission, peaking at $\sim$ 350 nm, observed with soft X-ray excitation, is also believed to originate from the oxide phase of the material. Emission from silicon crystallites was dismissed in this case as the band gap of the material was

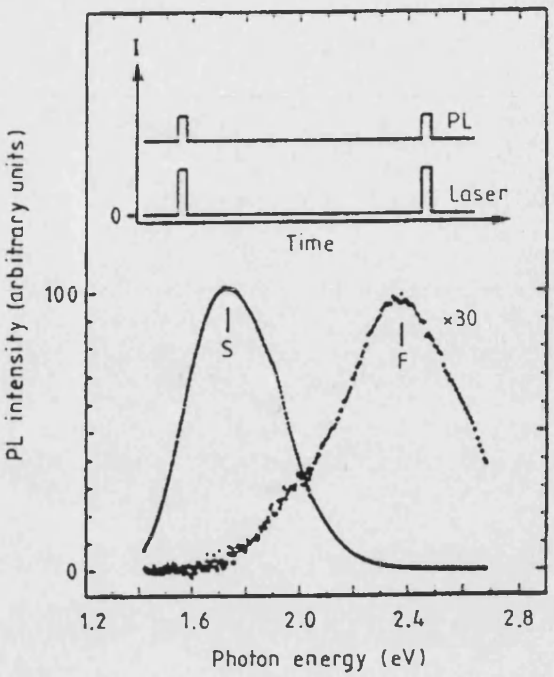

Figure 1.10: Results of time resolved PL experiments showing the existence of both a fast and slow spectral band. The inset shows a schematic of the laser pulse and PL signal, as described in the text [28]

not wide enough to produce photons of the observed energy (~4eV) [30].

Significant IR emission, first achieved by Fauchet *et al.* in 1993 [31] has received comparatively little attention. The emission was obtained from material annealed under ultra high vacuum and shows a tunability of emission wavelength between 1.1 to 1.5 μm, which is similar to that of the S band. The origin of this emission has been attributed to the recombination of carriers trapped in dangling bonds formed on the surface of the silicon nanocrystals [32].

1.6.2 The S Band

Efficient visible PL is attainable from homogeneous layers manufactured from substrates of all types, efficiencies normally decreasing in the order of n-, p-, n+, and p+ [14]. The main criteria for strong luminescence is that the material must be of high porosity [33]. PL can also be observed from material of lower porosity, although it is then seen to originate from small regions of the high porosity, i.e.

the PL source within a macroporous layer is found to be mesoporous material lining the pores [34].

Since the discovery of S band luminescence, numerous models have been proposed for the mechanism responsible for this emission. In his 1990 publication, Canham suggested that the quantum confinement of carriers in silicon wires was the origin of the observed luminescence [1]. Other mechanisms suggested in recent years include emission from surface hydrides [35], complex molecules (e.g. siloxene) [36] and hydrogenated amorphous silicon [37]. Discussions regarding the validity of these different models have been the the subject of several review papers [14][38]. However, of all the proposals, that of quantum confinement has continued to receive the strongest support both experimentally and theoretically, and thus remains the favoured model for light emission.

Quantum confinement (QC) occurs when the physical structure of a material is reduced, e.g. forming a fine wire or box. In the QC model for p-Si, luminescence is due to the radiative recombination of excitons localised within undulating crystalline silicon wires [28]. The exciton radius within the bulk material defines the size regime below which quantum size effects are likely to occur. In bulk silicon the free excitonic Bohr radius is $\sim$5 nm, thus in p-Si wires of dimensions less than this, QC effects are expected. The energy of the emitted photon will be lower than the band gap values by the exciton binding and localisation energies, i.e. after the diffusive drift of the exciton to a position of lowest energy in the connected wire network [14].

A consequence of QC effects, which have been extensively studied in III-V semiconductor materials, is an enlargement of the electronic band gap. This increase in the band gap is size dependent, i.e. as the wire width is decreased, the band gap increases. This effect naturally explains how the peak emission wavelength of p-Si can be tuned with changes in porosity, as displayed in figure 1.11. It can be seen that with increasing etch time, corresponding to a reduction in structure size [39], the peak wavelength blueshifts as the band gap widens. The width of the band is believed to be due to a distribution in the silicon nanocrystal sizes to which there corresponds an energy distribution of excitonic recombination energies [8].

A further effect of reducing the structural size is to increase the likelihood of

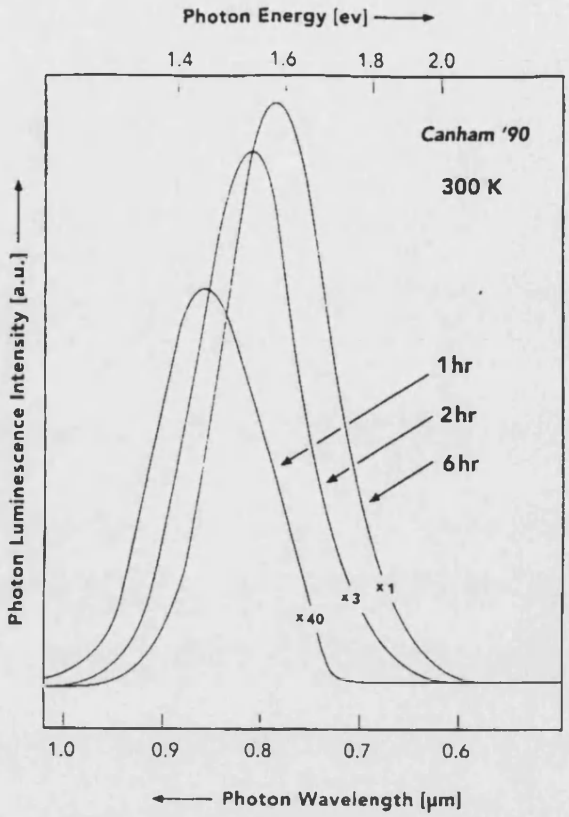

Figure 1.11: Room temperature PL from a p- doped p-Si layer. The spectra were taken after immersion in HF for the times indicated [1].

carrier recombination. Qualitatively, the confinement of carriers in real space causes their wavefunctions to overlap thus increasing the chance of strongly radiative transitions. In addition, scattering at boundaries can supply the needed momentum for a transition to occur in an indirect material.

As shown in equation 1.1 the internal quantum efficiency of light emission from a material can be increased by either increasing the radiative recombination rate or lowering the non-radiative recombination rate. The shape of the decay curve obtained from time-resolved PL measurements of p-Si provides valuable information regarding which regime applies to the system. If radiative recombination is dominant it would result in faster decay of excited carriers. Alternatively, if non-radiative processes are quenched, carrier lifetimes will increase, thereby slowing the decay time. P-Si time-resolved measurements are found to exhibit a slow decay of the order of microseconds. This confirms that the the increased light

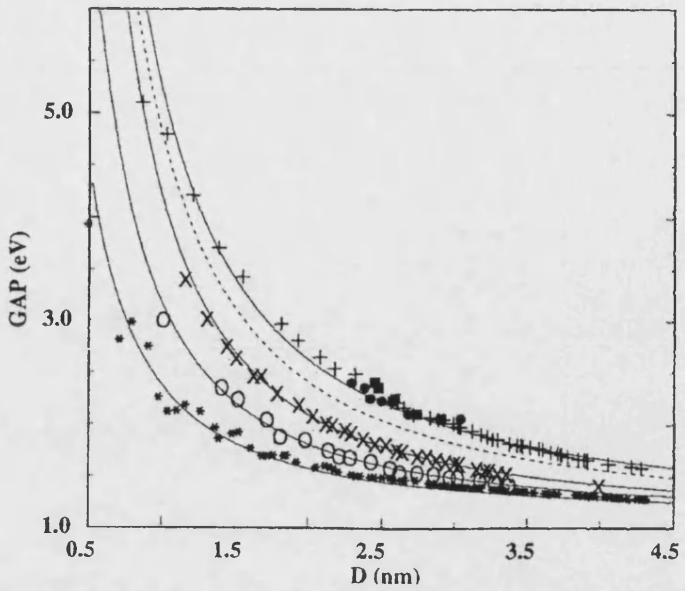

Figure 1.12: Calculated optical band gap energies for various silicon crystallites (+), or wires in the ((100): X; (110): *; (111): o; directions, with respect to their diameter *d*. The continuous lines are fits to this data [41].

emission efficiency observed from p-Si is due to the quenching of non-radiative pathways rather than increased radiative recombination [40].

In recent years, many experimental and theoretical results have been shown to support the QC model. X-ray diffraction and TEM measurements of high porosity luminescent layers composed of undulating wires have shown the structure to be completely crystalline [17]. Furthermore, TEM studies have allowed a direct and clear measurement of wire diameters <3 nm. These results show that the wire radii are less than that of the free exciton Bohr radius in bulk silicon, thus verifying that significant QC effects are likely to occur. Theoretical electronic structure calculations (figure 1.12) have verified that the increase in band gap energy due to a reduction in structural dimensions is consistent with that expected from silicon nanostructures of the same size as those observed in p-Si [41].

Of the experimental methods used to characterise p-Si, one of the most common is PL. A significant problem encountered in p-Si PL measurements is that the large linewidth, caused by inhomogeneous broadening, obscures the spectroscopic information it contains. By using a technique of resonantly excited PL these

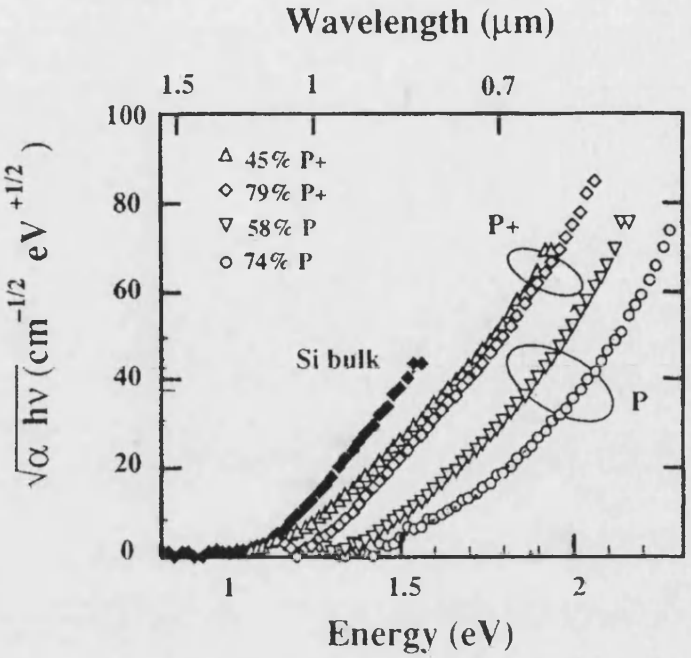

Figure 1.13: Square root of the absorption coefficient α times the photon energy $h\nu$, versus photon energy for c-Si, p and p+ p-Si [42].

problems may be overcome. In these experiments a laser tuned inside the broad PL spectrum is used to provide size selective excitation of the nanocrystals at low temperature. Under these conditions, the spectrum shows discrete steps at energies corresponding to phonons that are known to be involved in the absorption and emission of light in c-Si [28]. These results suggest that c-Si is both the absorbing and luminescing species.

Further experimental evidence for QC has been provided by the work of Sagnes *et al.* regarding absorption in p-Si [42]. This work compared the optical transmission of free standing p-Si films, fabricated from p and p+ p-Si with a range of porosities, with that of bulk silicon. Results showed that transmission below the direct gap is significantly increased in p and p+ p-Si relative to the bulk silicon. This shift in absorption edge to higher energy was attributed to QC effects enlarging the band gap of p-Si. Furthermore, the absorption spectra of both p and p+ layers undergo a porosity dependent shift, i.e. increased porosity shifts the absorption edge to higher energies as shown in figure 1.13. The upshifted absorption of p type layers relative to p+ layers is a consequence of quantum confinement due to the smaller structural dimensions of the former (table 1.1).

Even though QC accounts for the vast majority of experimental and theoretical results, there remain some observations that are difficult to reconcile with this model. Examples of these include results demonstrating a correlation between surface chemistry and PL peak wavelength. A common feature of all p-Si layers is the enormous surface area. This huge area is likely to be susceptible to the application of post etch treatments. Immediately after the sample has been etched, IR absorption spectra show the surface is hydrogen passivated. If this freshly prepared sample is then thermally annealed, desorbing the hydrogen to leave dangling bonds on the crystallite surface, a PL signal is no longer detectable. The dangling bonds have thus become non-radiative pathways. A further result which indicates surface involvement is that recently obtained by von Behren [43]. Although confirming a relation between sample PL and quantum confinement effects, his results also showed that if the samples were kept in an Argon atmosphere after anodisation, and were never exposed to air, the photon energy was much larger.

It has been acknowledged that these results can not yet be fully explained purely within the framework of the QC model, i.e. the peak position of the PL is not solely dictated by confinement. These issues need further study. What must be remembered when interpreting any given experiment is that the PL origin and peak emission are critically dependent on sample preparation, processing and handling.

1.7 Summary

The contents of this chapter have described the fabrication, morphology and luminescence of p-Si. The following chapter will show how this luminescence can be controlled and modified by periodically microstructuring the material. Examples will be given of the use of these multilayer structures in both passive and active applications.

Chapter 2

Spontaneous Emission Control In Periodic Microstructures

2.1 Introduction

The prospect of producing components based entirely on silicon for optoelectronic applications has created much interest in improving the efficiency of light emission from p-Si. A possible solution to this problem is the microstructuring of semiconductor materials which offers the potential to produce highly efficient and spectrally narrow light sources [44]. The prospect of gaining improved efficiency and control over p-Si emission through the use of this type of structural design has led to much investigation into this subject area [45][46].

The following chapters will investigate both theoretically and experimentally, the control of light emission and propagation within microstructured p-Si. The aim of this work is to provide useful information about how to improve the optical characteristics of future device designs.

This chapter will discuss the effects of microstructuring on light emission, both in general terms, and with regards to p-Si structures. Firstly, details of the emission process and the effect of microstructuring on its properties will be discussed. This will be followed by a description of the design, fabrication and optical characteristics of different structures, with regards to p-Si structures in particular. Finally

results of previous work on microstructuring in p-Si light emitting devices will be presented.

2.2 Spontaneous Emission

In 1917, Einstein proposed the existence of three types of electronic transition within an isolated atom subject to an interaction with an electromagnetic field. These transition processes are absorption, stimulated emission and spontaneous emission [47]. These processes also occur in semiconductors, although interactions between neighbouring atoms now result in energy levels that are no longer discrete but form bands.

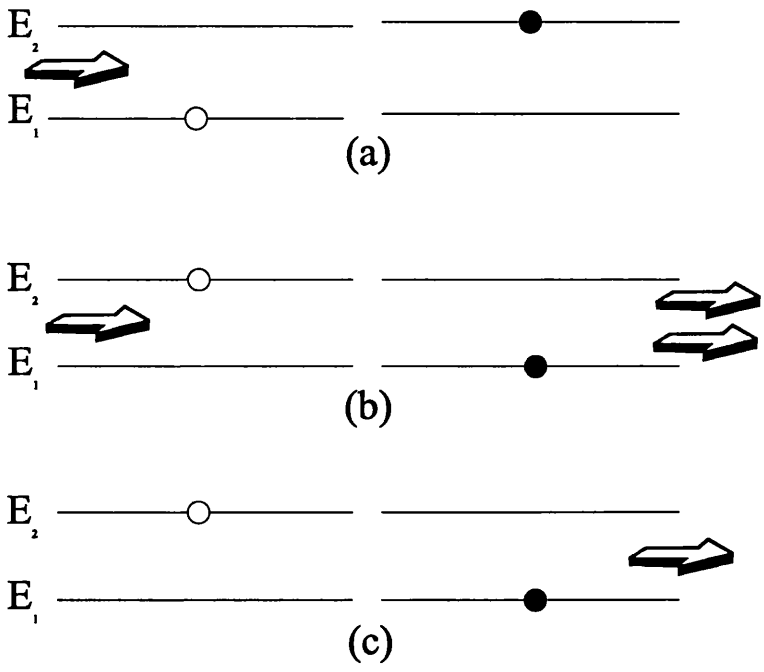

Figure 2.1: Schematic picture of (a) the absorption process, (b) the stimulated emission process, and (c) the spontaneous emission process.

In the absorption process (figure 2.1a), an incident photon of frequency ν causes a transition to occur from a lower (E_1) to a higher (E_2) energy state, the photon of energy $\Delta E = h\nu$ being absorbed, where $\Delta E = E_2 - E_1$. In the stimulated emission process, (figure 2.1b) an incident photon of frequency ν stimulates a transition from E_2 to E_1. This downward transition is accompanied by the emission of a photon with the same frequency as the incident one. The emitted

photon is coherent with, has the same polarisation, and propagates in the same direction as the stimulating photon. In the spontaneous emission process, a material initially in energy state E_2 spontaneously decays to E_1 by emitting a single photon (figure 2.1c). Semiconductors which decay by spontaneous emission radiate independently, and thus photons emitted by this process are incoherent and propagate in random directions.

The spontaneous emission properties of a semiconductor, e.g. decay rate, transition energy and radiation pattern, are not fixed characteristics, but a consequence of the coupling which occurs between the electronic dipole moment and the electromagnetic field surrounding it. The study of the quantum nature of electromagnetic fields and atom-field coupling is known as Quantum Electrodynamics, or QED.

QED shows that there will always be an electromagnetic field present in the atom's vicinity, this field being in its state of lowest energy, or zero-point state. Perturbations in this vacuum field, i.e. virtual photons, will induce spontaneous emission [4]. Due to its random and incoherent nature, spontaneous emission is a major source of energy loss and noise in semiconductor optical devices [48]. Developing the capacity to manipulate this emission will enable more efficient and controllable operation of optoelectronic emitters.

Since the discovery in 1990 of efficient room temperature PL from p-Si, many investigations have been undertaken to determine its potential for use in light emitting devices (LEDs) within optoelectronic applications based entirely on silicon. A key issue when designing p-Si LEDs is that of electroluminescence efficiency. This must be comparable to that of existing semiconductor LEDs fabricated from the naturally more efficient direct gap semiconductor materials (section 1.3).

The first p-Si LED was fabricated by depositing a contact layer on top of a freshly etched layer. This device had an external electroluminescence efficiency, i.e. light output from the device as a percentage of the total emitted from the material, of only 10^{-5}% [49]. Efficiencies from later devices utilising pn junction designs approached 0.2% [50]. Although approaching a practically useful value of 1% [51], these efficiencies could be improved upon further by careful consideration of device design [44].

One method of improving device performance is to design the structure such that the spontaneous emission characteristics of the material are modified. Modification of the emission spectra can be achieved through the manipulation of the photon density of states (DOS) to allow only certain propagation modes to exist in the structure. Control over the photon DOS can be obtained by microstructuring the material, e.g. layering it, to form multilayer mirrors and cavities. Use of this design influences both the radiation pattern and decay time of the emission. The microstructuring of p-Si to control these spontaneous emission characteristics is discussed below.

2.3 Porous Silicon Multilayer Mirrors

Highly reflective mirrors can be fabricated using a single metallic coating, ranging from protected aluminium (average reflectivity 87% in the visible spectrum), to bare gold (average reflectivity 99% in the visible spectrum) [52]. However, problems with the use of metallic mirrors include lack of durability, oxidation of unprotected metal, and absorption losses at the low wavelength (<500 nm) region of the visible spectrum. These problems can be reduced by the use of dielectric materials in mirror fabrication.

To achieve mirrors with equivalent or higher reflectivities than metallic mirrors using dielectric materials requires structuring them to form a multilayer stack. One of the most common uses for dielectric multilayer mirrors is within VCSELs, where highly reflective mirrors are required to confine light within the lasing cavity [53].

The multilayer mirror is a sequence of alternate layers of high and low refractive index dielectric material, often requiring two different types of semiconductor materials to achieve this. The optical thickness of each layer, d_{opt}, is given by,

$$d_{opt} = n\, d_{phys}, \tag{2.1}$$

where n and d_{phys} are the refractive index and physical thickness of the layer respectively (figure 2.2).

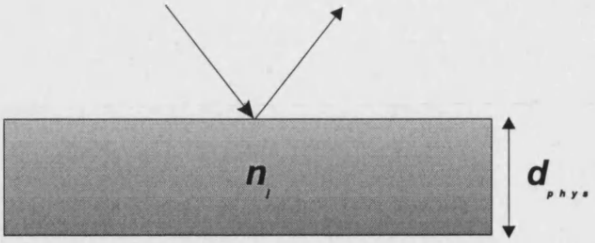

Figure 2.2: Schematic showing single layer parameters.

The simplest form of dielectric mirror design is the quarterwave stack. In this structure, the alternate layers each have an optical thickness of $\lambda_B/4$, where λ_B, the Bragg wavelength, is the wavelength where peak reflectivity is required. At normal incidence, λ_B is given by the equation,

$$m\lambda_B = 2(n_H d_H + n_L d_L), \quad (m = 0, 1, 2 \ldots), \tag{2.2}$$

where n_H, n_L, d_H and d_L are the refractive indices and the physical thicknesses of the high and low index layers respectively.

The wavelength at which the Bragg condition is satisfied will also change as a function of incident angle as given by the equation [54],

$$\frac{m\lambda_B}{2} = d_H \sqrt{n_H^2 - sin^2\theta} + d_L \sqrt{n_L^2 - sin^2\theta}, \tag{2.3}$$

where θ is the angle of incidence. Experimental results exhibiting this effect will be shown in section 4.2.2.

At the Bragg condition, reflections at low/high index interfaces phase shifted by an amount π are exactly cancelled by a π phase shift in the light reflected due to the path difference between alternate reflecting surfaces [55]. Therefore, all waves reflected from the stack interfaces will be exactly in phase and thus undergo constructive interference to form a strong reflected wave I_r (see figures 2.3 and 2.4c).

In fact, individual layers are not necessarily required to have an optical thickness

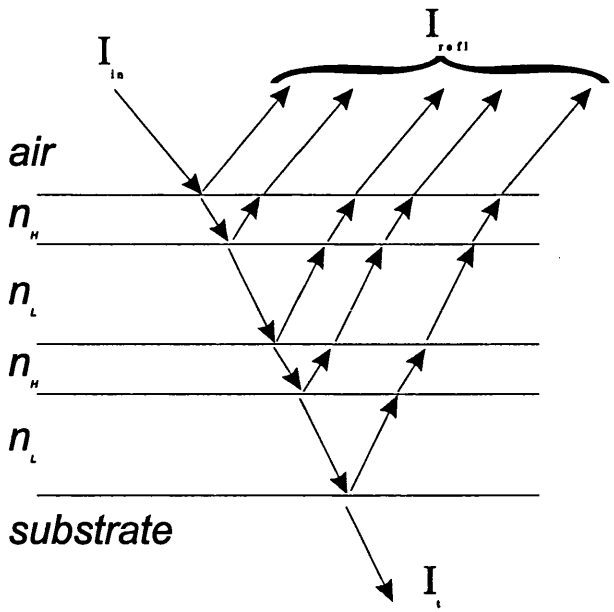

Figure 2.3: Schematic view of the reflection of waves from multilayer stack interfaces.

$\lambda_B/4$. Provided that the combined optical thickness of a high/low index pair is $\lambda_B/2$, the Bragg condition will be met (equation (2.2)). This fact is useful to consider when examining methods of minimising the absorption of emitted light in active p-Si multilayer structures. By decreasing the amount of high index/low porosity material in the structure there will be less material available to absorb light. This decrease of layer thickness is counterbalanced by increasing the amount of low index/high porosity material such that equation 2.2 is satisfied, i.e. layers of optical thicknesses $\lambda/8$ and $3\lambda/8$ will still have a combined optical thickness of $\lambda/2$.

Figure 2.4 illustrates the dependence on the calculated reflectivity at normal incidence of three systems at wavelengths between 1 μm and 2 μm. These structures are (a) a 3 μm layer with 50% porosity, (b) a quarterwave stack composed of 10 repeats with porosities 50% and 70% and thicknesses 0.18 μm and 0.22 μm respectively, and (c) a 20 repeat quarterwave stack with the same layer porosities and thicknesses as (b). The results are plotted as a function of wavelength for ease of comparison with experimental data presented in chapters 4 and 5. Furthermore, the variation of refractive index with both wavelength and porosity has been taken into account when modelling these structures (sections 3.3.1 and 3.3.2 respectively). Discussion of the entire modelling procedure will be given in further detail in the following chapter.

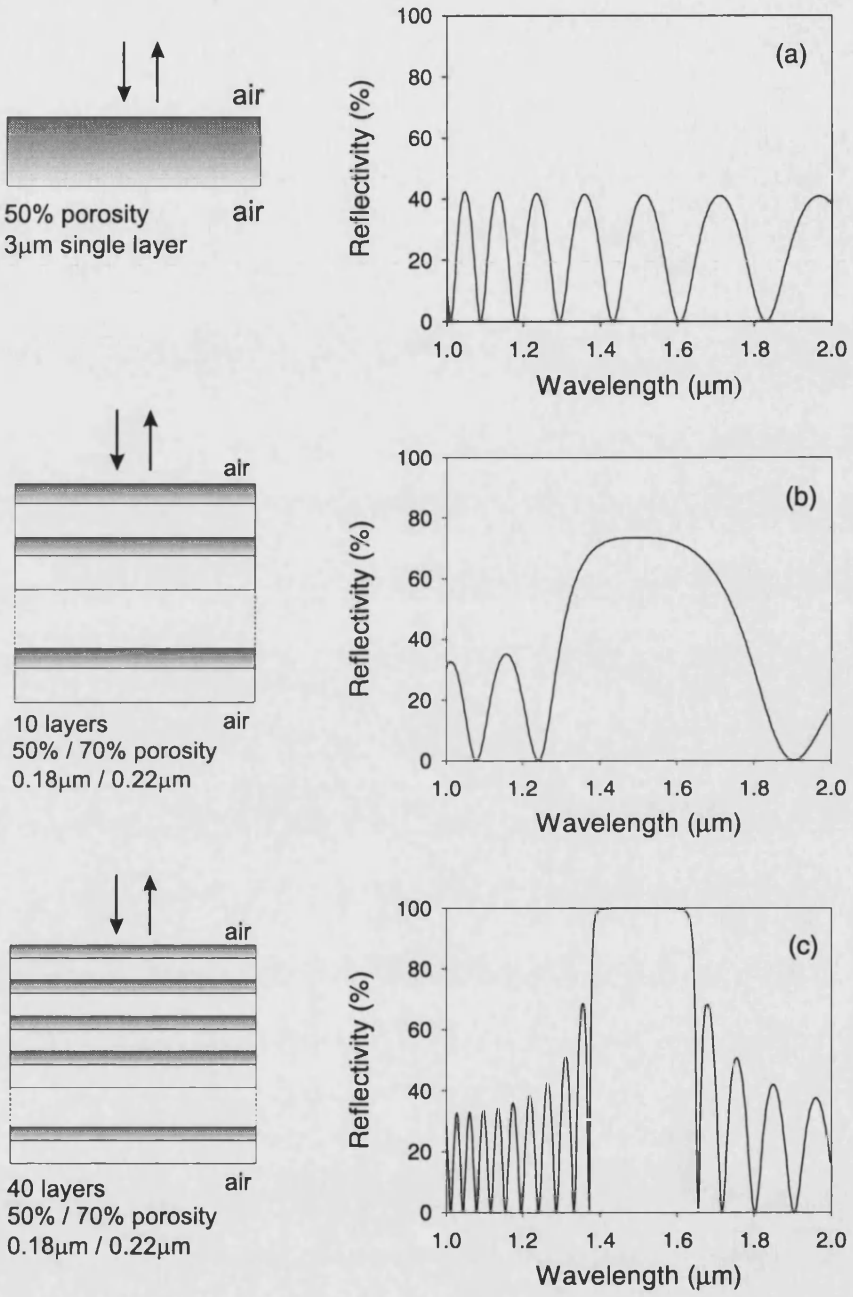

Figure 2.4: Calculated normal incidence reflectivities of three p-Si systems. a) A 3 μm layer with 50% porosity. b) 10 layer pairs with porosities 50% and 70% and thicknesses 0.18 μm and 0.22 μm respectively. c) 20 layer pairs with layer porosities and thicknesses as described in (b).

In the case of the single layer (figure 2.4a), the reflectivity spectrum shows Fabry-Pérot fringes. These are formed from successive reflections from the front and back interfaces undergoing constructive and destructive interference dependent on the relationship between light wavelength and layer thickness. As the number of layer pairs is increased (figure 2.4b), the strength of the reflected wave increases and a region of high reflectivity, called the stopband, begins to develop. The stopband is centred on λ_B, which in this case is chosen to be $1.5\,\mu$m. This feature becomes dominant when the number of layer pairs is increased further (figure 2.4c), and forms a broad region of high reflectance.

In the stopband region constructive interference from successive reflections at the stack interfaces produce a peak reflectivity close to 100%. Either side of the stopband, the reflectance reduces in an oscillatory fashion. These resonance modes are the Fabry-Pérot modes of the total 8 μm thick structure, similar to those seen in figure 2.4a. The bandwidth of the stopband $\Delta\lambda$ is controlled by Δn, the refractive index difference between layers. If $\Delta\lambda$ is defined as the FWHM of the reflectivity stopband then it is given by [56],

$$\frac{\Delta\lambda}{\lambda_B} = \frac{4}{\pi}\sin^{-1}\left(\frac{n_H - n_L}{n_H + n_L}\right). \tag{2.4}$$

The peak reflectivity of the stopband can be increased by enhancing the strength of the reflected wave. This can be achieved by adding more layers to the stack, thereby increasing the number of reflections, and enlarging Δn, thus enhancing the reflectivity of each individual layer interface [55].

2.4 Fabrication of Multilayer Structures

The fabrication of multilayer stacks exclusively from p-Si is a low cost and quick process. Both high and low refractive index layers may be obtained from the same material, as the index of each layer depends on varying the porosities (section 1.4). Therefore, a stack with alternating layers of low and high porosity material is also a structure with alternate layers of high and low refractive index.

P-Si multilayer stacks can be fabricated in two different ways. In the first method,

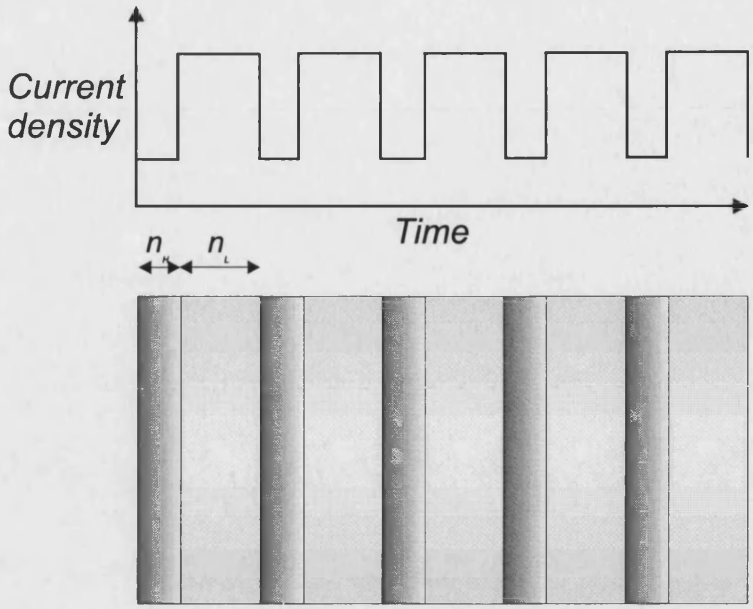

Figure 2.5: Schematic diagram to show the current switching process used to obtain multilayer stacks with alternating high and low refractive indices.

used to produce the devices studied in this work, etch parameters (i.e. the current density or illumination power) are periodically switched as the structure is etched from a homogeneous substrate to produce alternating layers of the required refractive indices n_H and n_L (figure 2.5) [58].

SEM and TEM images of a 20 layer p-Si structure, sample number C150[1], fabricated using this method is shown in figures 2.6 and 2.7. This structure, fabricated from a p+ substrate, is composed of alternating layers of porosities 54% and 71%, and thicknesses 0.19 μm and 0.34 μm respectively. The porosities of the layers were determined through the fitting of calculated curves to the experimental reflectivity data. The details of this fitting procedure will be discussed in chapter 4. For comparison, an SEM image of a multilayer structure, sample C139, fabricated from a p- substrate is shown in figure 2.8. As discussed in section 1.4, the layer interfaces of an etched p- doped substrate will exhibit a much greater degree of interface roughness than those in a p+ substrate. This increased roughness will result in greater scattering losses at the interface and thus reduced reflectivity. Examples of this will be shown in chapters 4 and 5.

The second method of fabrication involves etching a periodically doped substrate

[1] All sample names have been shortened for clarity. Samples are listed under their full names in Appendix B

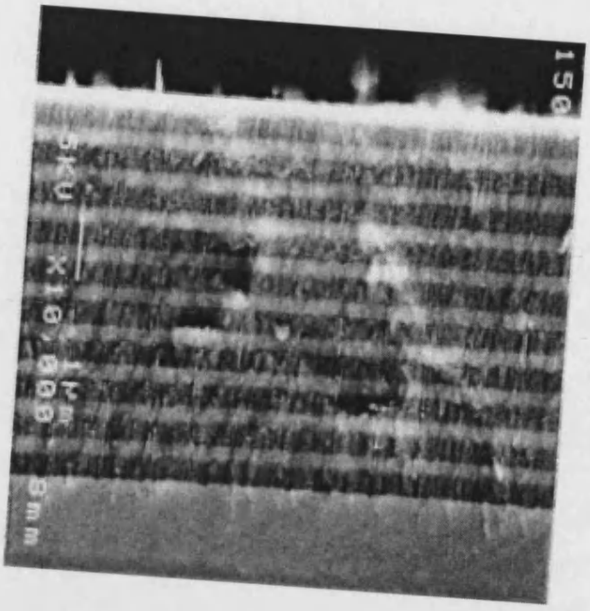

Figure 2.6: SEM image of sample C150, a 20 layer mirror formed from p+ doped material [57].

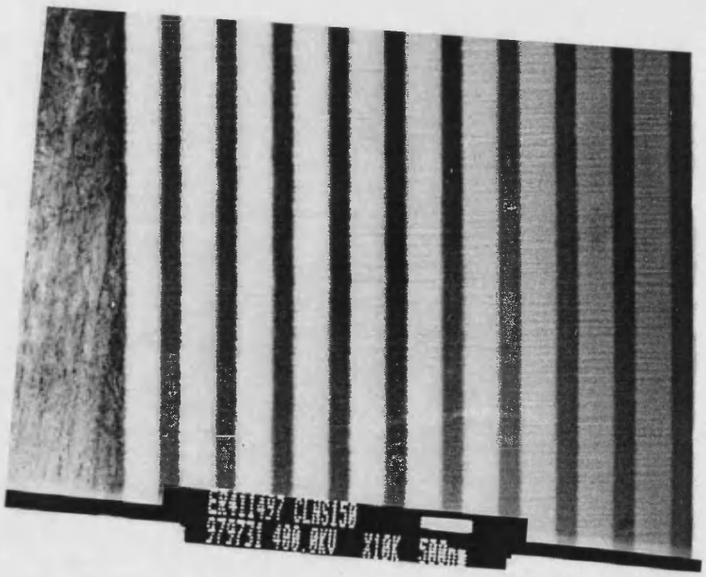

Figure 2.7: TEM image of sample C150, a 20 layer mirror formed from p+ material [57].

Figure 2.8: SEM image of sample C139, a 20 layer mirror formed from p- doped material. The wafer surface is on the left hand side of the image. [57].

whilst keeping the etch parameters constant [11]. The fabrication of multilayers by this means is less common than the first owing to the requirement of a epitaxially grown substrate.

A known problem with the etching process, particularly in larger multilayer structures, is the formation of gradients in the microstructure with depth e.g. porosity gradients. Examination of these gradients within p- and p+ p-Si samples has shown that two main effects are responsible for their formation. A different effect dominates depending on whether the structure is etched from a p- or p+ wafer.

Raman studies of p- single layers have revealed that an increase in crystallite size occurs when moving from top to bottom of the layer [59]. The thinning of the microstructure observed in the upper regions of the layer is a result of additional chemical etching due to increased storage time of the material in the electrolyte. This etch, called leaching, is not driven by current. Given their larger internal surface area p- samples are more susceptible to this effect, however it also occurs to a lesser effect in p+ samples.

In contrast, Raman studies have shown that within p+ structures the crystallite size changes from large crystallites on the surface to smaller ones at the p-Si/substrate interface. The cause of the increase in porosity from top to bottom has been attributed to a decrease in HF concentration with depth due to

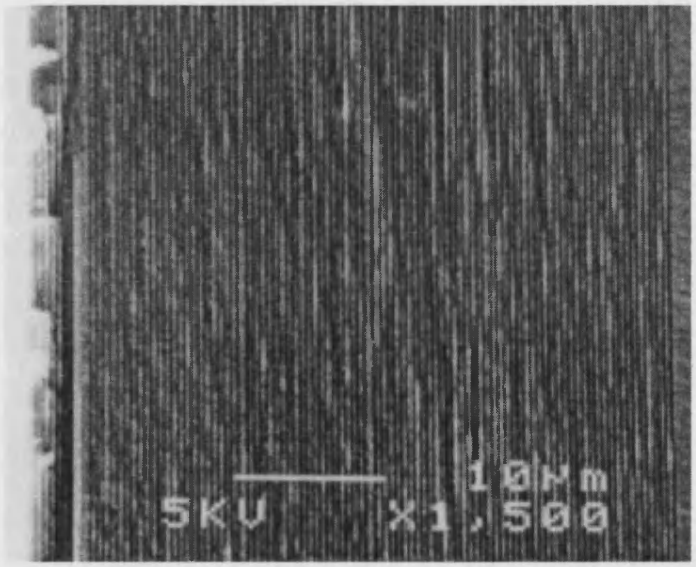

Figure 2.9: SEM image of sample C155, a 400 layer mirror fabricated from p+ material. Note the cracking of the uppermost layers, shown on the far left hand side of the image, due to leaching effects [57].

diffusional problems in the electrolyte [60] [59].

Depth variations in the porosity, and hence refractive index, exhibited by p-Si samples, will result in changes to the optical properties of the structure, e.g. within a dielectric mirror an increase or decrease in the optical thickness of the layers will result in the Bragg condition shifting to higher or lower wavelengths respectively. Furthermore, in both p- and p+ doping types, these changes to the microstructure will result in the sample becoming more mechanically fragile and thus likely to disintegrate [21].

An example of a reduction of mechanical stability in larger structures in shown in figure 2.9. The figure displays an SEM image of sample C155, a 400 layer multilayer structure fabricated from p+ material using the same etch parameters as those used to form the structure of figures 2.6 and 2.7. During etching of this sample, the upper layer porosities increased by leaching to such an extent that the sample began to degrade during the drying process.

To minimise the problem of porosity gradients within p+ multilayers Thönissen *et.al* have developed a method of changing the current density with depth as the etch progresses [60].

The etch rate r, and thus the thickness of the layer are related to the porosity, P, by the equation,

$$\frac{r_{etch}}{j} = \frac{A_r}{P\,\nu_{Si}\,e\,N_A\,\rho}, \tag{2.5}$$

where j is the current density, A_r the relative atomic mass of silicon, ν_{Si} the valence, N_A Avogadro's number and ρ the density of silicon [60]. Changes in the layer porosity caused by an HF concentration gradient will therefore result in a non uniform etch rate resulting in non-uniform layers.

Through the use of *in situ* reflectivity measurements at fixed wavelength and current density, Thönissen investigated how changes in the porosity, and hence optical thickness, of the layer altered the frequency of the reflectivity oscillations as a function of time. Repeating this experiment for different current densities allowed him to establish a graphical relationship between etch rate, layer thickness and current density. Using this relationship it was thus possible to determine the current density as a function of depth required to maintain a constant etch rate.

These fabrication techniques can be used to fabricate many different p-Si structures. P-Si multilayers have a wide variety of applications as passive devices. These include interference filters [61], vapour sensors [54], and bio-sensors [62]. Etching of two dimensional structures has also been performed to fabricate holographic gratings [63].

The following section discusses how this technique can be extended to form cavities for use in active light emitting devices.

2.5 Active devices using Microcavities

2.5.1 Microcavity structure

A standard microcavity is formed by the placement of an optically active material of thickness the order of an optical wavelength between two high reflectivity

mirrors. These mirrors may be either metallic coatings or dielectric multilayer stacks, and the central active layer may be composed of a single or multiple quantum wells [64] [65] , or simply a bulk layer of light emitting material [45].

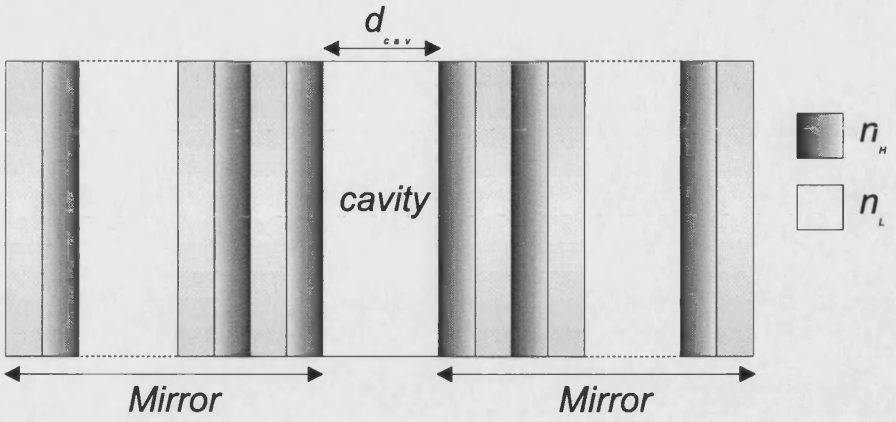

Figure 2.10: Schematic view of microcavity. This example is formed by enclosing a bulk active layer between two multilayer mirrors.

An example of the latter case, is shown schematically in figure 2.10. The central layer of thickness d_{cav} is sandwiched between two multilayer mirrors. In this case the refractive index of the active layer is the same as that of the low index layers of the two mirrors. This parameter, and those relating to the refractive index and number of mirror layers may be adjusted according to the optical characteristics desired from the device.

When emission occurs within the cavity, all photons, with the exception of those propagating approximately parallel to the cavity axis, will soon exit the structure due to the limited confinement provided by the mirrors. In contrast, light propagating in a longitudinal cavity mode will continue to build in strength as it stimulates more emission from the active material. This propagation mode takes on a standing wave configuration, i.e. it is resonant, when an integer number of half wavelengths span the cavity such that a wave node exists at each mirror.

The frequencies of these allowed modes ν_m, are thus given by,

$$\nu_m = \frac{m\,c}{2\,n_{cav}\,d_{cav}} \quad (m = 1, 2, ...), \tag{2.6}$$

where n_{cav} and d_{cav} are the refractive index and thickness of the cavity layer

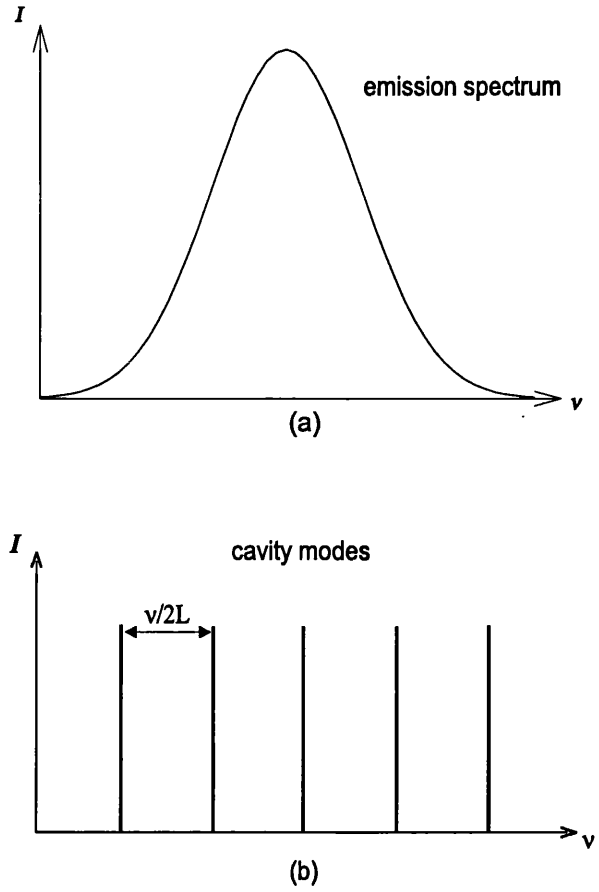

Figure 2.11: Schematic diagram demonstrating how the cavity selects only certain available frequencies from the broad emission spectrum [55]

respectively. It should be noted that when using dielectric mirrors to form the cavity, the confined photon mode will penetrate a finite distance into both mirrors. The penetration depth is dependent upon the refractive index contrasts which exist between the structure layers, i.e. the penetration distance will decrease as the index contrast increases.

Consecutive cavity modes are separated by a constant difference called the free spectral range (FSR), $\Delta\nu$, which may be written as,

$$\Delta\nu = \frac{c}{2\, n_{cav}\, d_{cav}}. \tag{2.7}$$

The only longitudinal modes sustained in the cavity are those with frequencies

given by equation 2.6. If it happens that the material emission spectrum is sufficiently broad enough to span several of these modes, only emission occurring at these frequencies will be allowed to propagate from the cavity (figure 2.11).

A quantity indicative of the quality of the cavity is the finesse, F. This value is the ratio of the separation of adjacent modes to their half widths. The finesse is written as,

$$F = \frac{\pi}{2}\left(\frac{4R}{(1-R^2)}\right)^{\frac{1}{2}}, \tag{2.8}$$

where R is the mirror reflectivity. From equation 2.8 it can be seen that higher reflectivity mirrors will result in sharper cavity modes. However, the reflectivity must not be so high that emitted light has difficulty exiting the cavity. The balance of these two effects must be carefully examined when considering methods of optimising device output.

The parameter used to describe the amount of emission which is coupled into these cavity modes is the coupling coefficient β, where,

$$\beta_c = \frac{\text{spontaneous emission into desired mode}}{\text{spontaneous emission into all cavity modes}} \tag{2.9}$$

When considering the coupling of spontaneous emission into available modes, it can be seen that one way of increasing β is to allow there to be only one cavity mode within the emission spectral bandwidth. For example, comparing the cavity thicknesses of a gas laser, d_{cav}=1m and a p-Si microcavity $d_{cav} = 0.75\mu$m, it can be seen from equation 2.7 that the microcavity modes can possess a free spectral range several orders of magnitude greater than that of the gas laser. Therefore, the chance of a microcavity being single moded, i.e. only one optical mode lies within the emission bandwidth, is much greater than that of a gas laser where emission may occur into several modes.

Yamamoto *et al* [48] have calculated the degree of enhancement and suppression of emission into cavity modes due to the modification of the vacuum field amplitude by the cavity (section 2.2). Interference between waves multiply reflected from

the cavity mirrors will enhance the field amplitude, thus inducing more emission. The calculations have shown the peak intensity of the emission from the resonant mode will be enhanced by a factor of $4/(1-R)$ over the free space value, whereas that of the non-resonant modes will be suppressed by a factor $(1-R)$. As the resonance mode propagates along the cavity axis, it is thus expected that a region of enhanced emission will exist in a cone concentrated about this region.

A further reason for using cavity structures is that the modifications they make to the photon density of states (DOS) not only decrease the emission bandwidth, but also alter the spontaneous emission rate. The emission rate Γ_{sp} of an electronic dipole in free space is given by Fermi's golden rule:

$$\Gamma_{sp} = \frac{2\pi}{\hbar}|\langle f|H_{int}|i\rangle|^2\rho(\omega), \tag{2.10}$$

where $H_{int} = \hat{\mu}\cdot E$ is the interaction Hamiltonian that couples the dipole moment operator of the transition $\hat{\mu}$ to the electric field E, $|i\rangle|$ and $\langle|f|$ are the initial and final states of the dipole-field system respectively and $\rho(\omega)$ is the photon DOS [66]. It has been theoretically shown that the limited level of confinement provided by a cavity comprised of multilayered dielectric material is sufficient to decrease the spontaneous emission lifetime $(1/\Gamma_{sp})$ by a factor of only a few percent [67]. However, experimental measurements of luminescence decay from single and multiple p-Si layers have indicated that a more significant change occurs [68]. This will be discussed further in the following section.

2.5.2 Cavity Losses

There are many losses inherent to the microcavity structure which will result in a poor coupling efficiency of the emission into the cavity mode. Instead of occurring into this mode, the emission can instead couple into competing lossy modes which also exist in the structure. These competing modes are leaky modes, guided modes and mirror resonance modes (figure 2.12).

Leaky modes exist because of the limited angle over which the multilayer mirrors reflect effectively. As shown by equation 2.3, the wavelength position of the Bragg

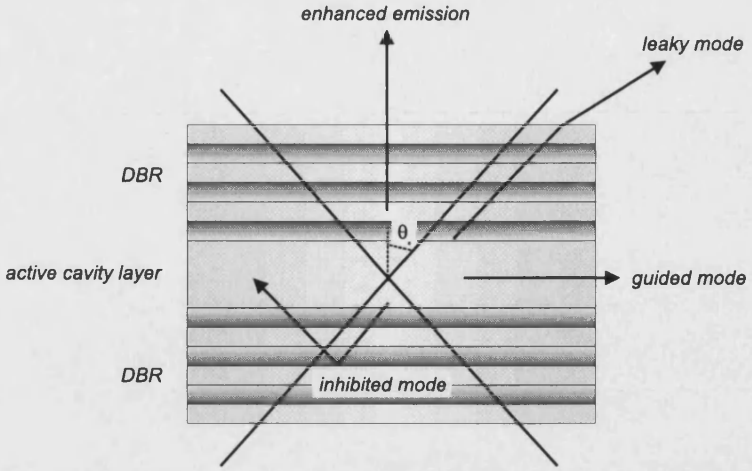

Figure 2.12: Schematic showing cavity loss mechanisms [8]

condition, and thus the stopband, will move as a function of angle. Thus, if the wavelength of the incident wave lies within the stopband at normal incidence, at a certain critical angle, this point will pass through the stopband edge and the reflectivity will fall accordingly. At angles of incidence above the critical angle, the multilayer mirrors will appear to be a homogeneous medium of refractive index n [56]. Guided modes occur in high index layers bounded on either side by material of lower index, and thus light can propagate the length of the active central layer by total internal reflection. Emission into mirror resonance modes will occur when the emission spectrum of the material is broader than the stopband of the microcavity structure. Light will thus couple into the modes either side of the stopband depending on their frequencies relative to the emission spectrum. Examples of emission into mirror resonances will be displayed and discussed in chapter 5.

Figure 2.13 shows the calculated reflectivity spectra of two example microcavity structures. In each case, a layer of optical thickness $\lambda_B/2$, where λ_B is chosen to be 1.5 μm, is placed between two mirrors, corresponding to the structures shown in figures 2.3b and 2.3c. The placement of this layer in the structure results in a dip in the reflectivity spectra in the centre of the stopband. This corresponds to the wavelength of a cavity resonance.

Adjusting the thickness of the layer will change the frequency of this resonance and thus result in the movement of the mode away from its central position. This characteristic may be used to select the the emission frequency of the structure.

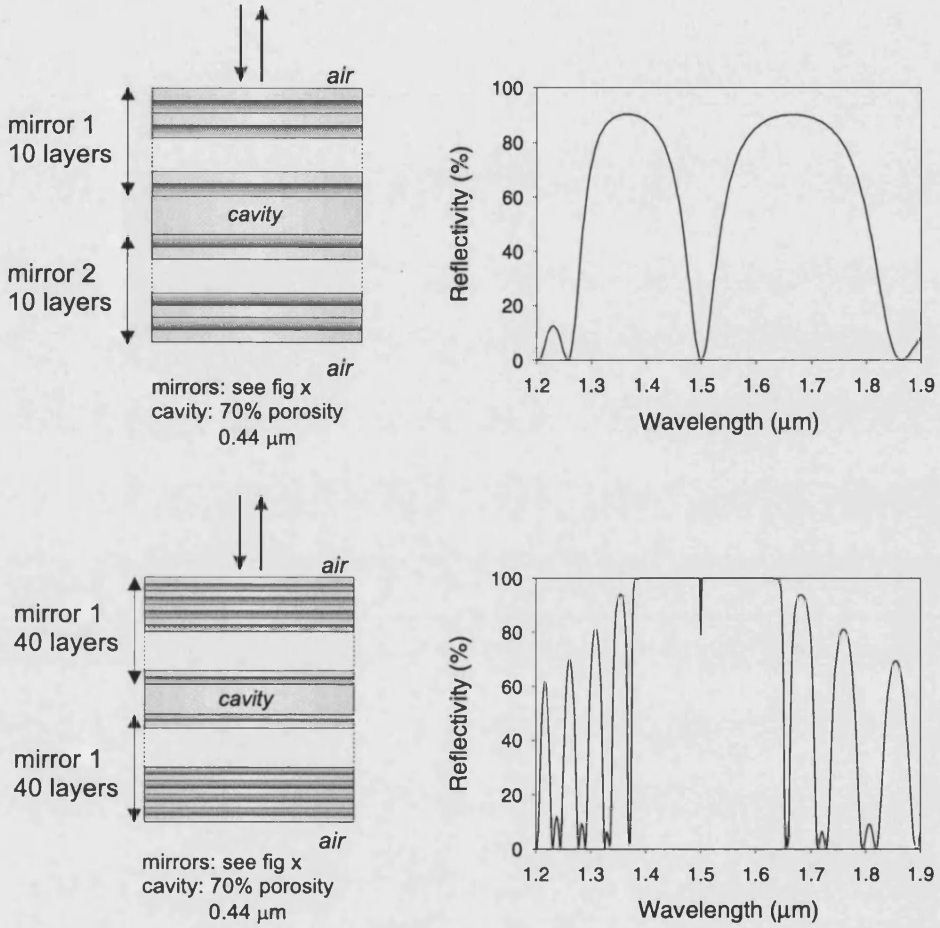

Figure 2.13: Calculated normal incidence reflectivities of two p-Si microcavity systems with mirrors of the same layer parameters as those used in figure 2.4. (a) Structure comprised of 70 % porosity, 0.44μm thick cavity layer between 10 layer mirrors. (b) Same as (a) but using 40 layer mirrors.

2.5.3 Porous Silicon Microcavities

Two different types of p-Si microcavity have been reported in the literature to date. The first type is composed entirely of p-Si [45], the structure being fabricated using the same current switching method as used to produce p-Si multilayer mirrors (section 2.4). The second type of structure was composed of a p-Si multilayer bottom mirror and a thin metallic top mirror [46].

The all p-Si device was demonstrated by Pavesi *et al.* in 1995 [45]. This was the first use of a microcavity to display spontaneous emission control in microstructured p-Si. Careful etching of the structure allowed the tuning of the cavity mode wavelength to coincide with the peak of the p-Si emission spectrum. In this case, independent measurements of a p-Si single layer fabricated using the same etch parameters as those used for the cavity showed the emission peak to occur at λ=760 nm. The microcavity itself consisted of a central layer of optical thickness λ and 75% porosity, enclosed between two p-Si multilayer mirrors each composed of six repeats of layers of optical thickness $\lambda/4$ and porosities 62% (n=1.5) and 45% (n=2.24) respectively. The sample was fabricated from a Boron doped p+ (0.01 Ω cm) wafer. Separate measurements showed the mirrors to have a reflectivity of approximately 97% resulting in a cavity finesse of approximately 50.

The room temperature PL spectra of the microcavity, a twelve repeat mirror and a single layer reference sample are shown in figure 2.14. The PL spectra were measured at an angle normal to the sample surface. The mirror is found to have some limited effect on the emission lineshape, the spectral features exhibited being a result of its stopband characteristics. It can be seen that the microcavity structure has two significant effects on the p-Si luminescence. Firstly, the bandwidth of the emission is narrowed from ~130 nm to ~15 nm, and secondly the PL peak intensity is an order of magnitude higher than that of the reference sample. As discussed previously, the first effect is a result of the cavity only allowing certain propagation modes to exist. Secondly, the increased coupling into the main cavity mode arises because this microstructure supports fewer competing lossy modes than a single layer. Furthermore, the increased confinement in the cavity means that the propagation mode will make more passes through the material and thus excite more emission. Furthermore, a significant narrowing of the radiation pattern was observed, the emission of the microcavity being restricted to a

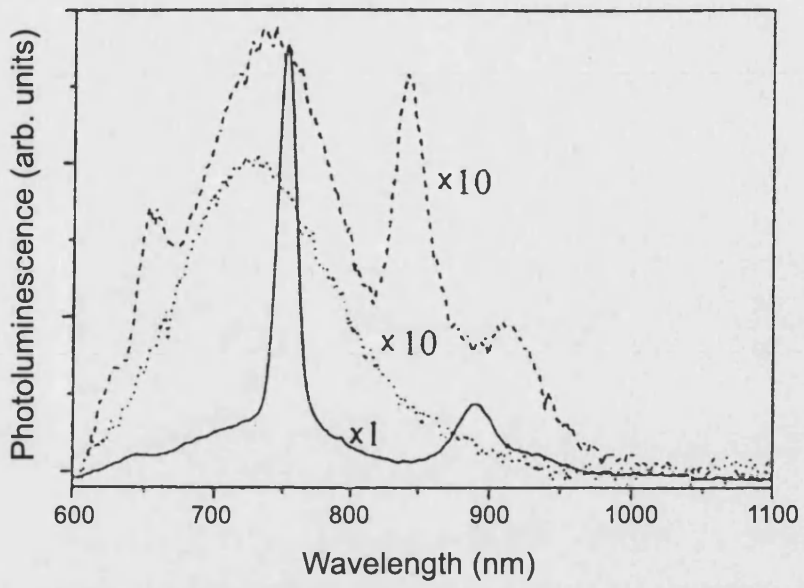

Figure 2.14: Comparison of room temperature PL spectra of a microcavity (solid line), twelve period mirror (dashed line) and single layer (dotted line) [45].

30 degree cone about the cavity axis, as discussed in section 2.5.1.

Contrary to the results of theoretical calculations [67], recent time resolved experiments carried out by Cazzanelli *et al.* [68] have shown a factor of 2/3 shortening of the emission decay time in a comparison made between a single reference layer and p-Si microcavity. Cazzanelli believes that the dielectric environment surrounding the emitting layer influences the emission decay time through the relationship between the photon DOS and the refractive index, n, of the medium, where $\rho(\omega) \propto n^3$ [68]. As discussed previously (section 2.5.1) the limited confinement provided by a microcavity will cause the photon mode to penetrate into the dielectric mirrors, the depth of this penetration being determined by the mirror and cavity refractive indices. Therefore, even though the cavity layer and single layer are of the same porosity, they will have different refractive indices because that of the cavity must also be averaged over the depth to which the optical mode extends into the mirrors. The modified index of the cavity caused by this effect will thus change the photon DOS and associated spontaneous emission rate.

The second type of cavity was demonstrated by Araki in 1996 [46]. The main structures, fabricated from a Boron doped p (0.4-0.6 Ω cm) wafer, consisted of

central layers of varying thickness, bounded on one side by a 20 layer multilayer stack and the other side by a thin (~25 nm) Ag coating. The reflectivity of the metal mirror was higher than 90% and that of the multilayer mirror ~90% in the wavelength region of interest. Experimental results show a narrowing of the emission bandwidth to approx 8 nm, but no enhancement of the emitted intensity was observed. This lack of enhancement was believed due to poor confinement in the cavity. This lack of confinement will result in (a) the transmission of the light from the cavity before it has made many passes through the material, and (b) emission into competing lossy cavity modes reducing the coupling coefficient β.

2.6 Summary

This chapter has discussed the method of microstructuring to control light emission from p-Si. It has been shown that the random and incoherent nature of free space spontaneous emission can be controlled by placing the emitting material in a microcavity structure. Microcavity effects on the emission include increasing the coupling efficiency by allowing only a single resonant mode to exist, increasing the decay rate, and narrowing the radiation pattern. In addition to this, work on experimental investigations into cavity effects on light emission using two different p-Si structures has been reported and their results discussed.

A potentially significant difference between p-Si multilayer structures and those fabricated from other semiconductors is that a p-Si structure will not simply be emissive in the central active layer, but throughout the entire microstructure. This is a difference not yet fully explored and explained in previous literature, and one which could necessitate changes in device design in order to utilise this additional emission.

The following chapters describe both theoretical and experimental work performed on p-Si microstructures. The aim of this work is to understand the mechanisms controlling the emission and propagation of light through different samples, and then use these results to produce optimised designs.

Chapter 3

Computer Modelling of the Optical Properties of Porous Silicon

3.1 Introduction

Modelling is a valuable aid to the design of p-Si devices. A good model allows the user to quickly predict the optical characteristics of a sample design, thus enabling the simple comparison of the spectra of many different structures. This process significantly reduces the amount of time required to optimise a particular device.

This chapter describes the theory concerning the modelling of p-Si optical spectra. Firstly, light propagation in microstructured materials is discussed in terms of photonic band gap theory. This theory provides a comprehensive view of structuring effects on the light emission process, some of which can be used to advantage in sample design. Following this, the determination of the material properties of silicon for both bulk and porous forms is discussed and the modelling methods are shown. The modelling of single layers of p-Si is carried out using a Fabry-Pérot model whilst that of multilayer mirrors and microcavities is performed using a transfer matrix method. The effects of material dispersion, porosity, absorption and emission can be included in both models. Finally, an

example of the process of sample design is shown. The light emission characteristics of four different p-Si structures are calculated using the transfer matrix model in order to determine their relative emission efficiencies. These results aid in the understanding of photonic band gap effects in periodic p-Si structures.

In chapters 4 and 5 it will be demonstrated that some of the the most valuable information that the modelling provides comes from its comparison with experimental results. These comparisons show both the level of validity and accuracy of the theoretical assumptions made during the modelling process regarding the material properties of p-Si. Any discrepancies between theory and experiment mean that refinements to the theory can be worked back into the model in a cycle of program development.

3.2 Introduction to Photonic Band Gap Theory

An alternative explanation of spontaneous emission control and light propagation in multilayer structures can be gained through the study of photonic band gap (PBG) theory. In analogy with electronic band structure, in an infinite periodic structure there will exist photon states for which propagation is allowed, and states for which it is forbidden, i.e. the photonic band gap. A periodic structure, e.g. a multilayer mirror or microcavity, can be considered as a one dimensional PBG structure which provides light confinement in the direction of the periodicity. In one dimension, the band gap, equivalent to the stopband of a mirror, represents a range of wavelengths $\Delta\lambda$ where both light emission will be inhibited within the structure, and all light incident on the stack will be reflected. Photonic band gap effects can be used to manipulate the emission and propagation of light in the direction of confinement. These effects are discussed below.

The effect of a photonic band gap on spontaneous emission from a direct gap semiconductor is illustrated in figure 3.1 [69]. This figure shows the two regimes of electronic and photonic dispersion. Due to atomic spacings being approximately 1000 times shorter than optical wavelengths the electron wavevector has been divided by 1000 to allow it to be displayed on the same plot as the photon wavevector. It can be seen that carrier recombination between conduction and valance band will be inhibited as the emitted photons have a frequency lying in

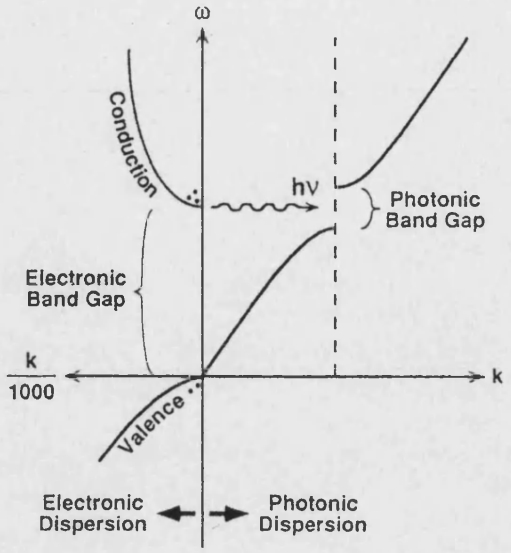

Figure 3.1: Schematic view of electronic and photonic band gaps. On the right, the band gap appears at the wavevector of the periodicity. On the left, an electronic dispersion diagram typical of a direct gap semiconductor is shown. Since the photonic band gap coincides with the electronic band edge carrier recombination is inhibited as the resulting photons are unable to propagate [69].

the photonic band gap. An electromagnetic wave with a frequency lying in this gap will thus be evanescent and unable to propagate from the structure.

The introduction of a defect layer, i.e. a microcavity, of width $m\lambda_B/2$ into the structure will introduce a defect mode into the centre of the band gap, its position corresponding to the resonance wavelength of the cavity (section 2.5.1). Emission not occurring into lossy modes (section 2.5.2) at this wavelength will be channelled into this mode which will be transmitted from the structure.

The periodicity of the multilayers has a further useful effect on light propagation in these structures. It is found that within periodic structures an electromagnetic field intensity will distribute itself into regions of high or low refractive index [70]. This distribution depends on the wavelength of the light and is illustrated in figure 3.2. It can be seen that on the short wavelength side of the stopband the light intensity is predominantly found in the low index regions, and on the long wavelength side, in the high index regions. At λ_B, at the centre of the stopband, the field stacks on the layer interfaces but quickly decays as it propagates into the structure, i.e. is evanescent. This field stacking effect can be used to advantage in p-Si. Using this effect it is possible to design a periodic structure so that at the

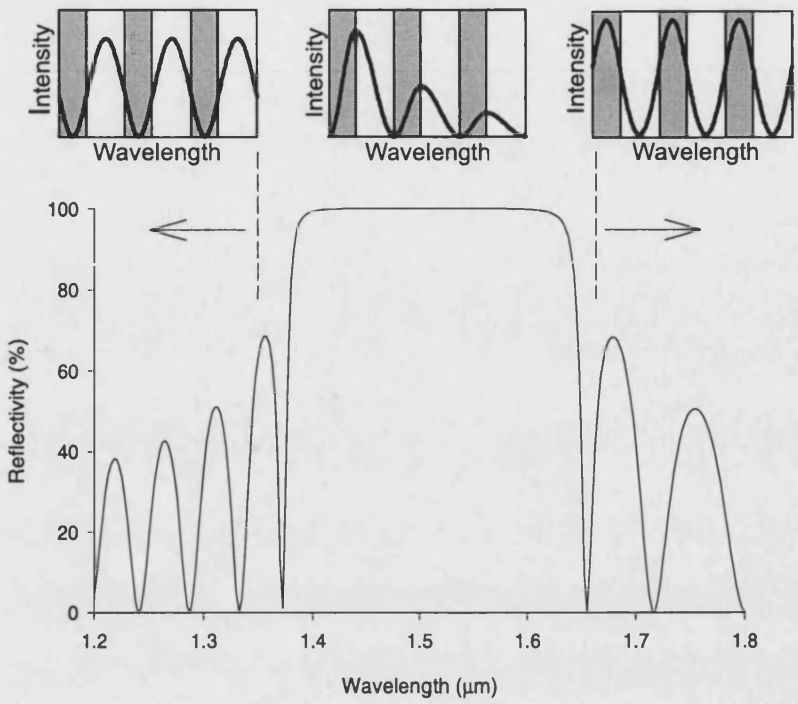

Figure 3.2: Calculated field intensity distribution in a multilayer mirror structure.

emission wavelength the majority of the light intensity is excluded from the low porosity highly absorbing layers and is instead concentrated in the high porosity layers where most of the emission will occur (section 3.3.6).

Photonic band gap theory will be used to both aid in sample design (section 3.7) and to help explain experimental results (chapters 4 and 5). The following section discusses the preliminary steps taken towards modelling p-Si microstructures.

3.3 Modelling of Porous Silicon Periodic Microstructures

To model the optical spectra of porous materials several steps have to be followed. The first is the calculation of the dielectric function of the bulk material over the wavelength range of interest. The second is to average this bulk phase with an empty pore phase to form an effective medium, whose properties determine the

macroscopic optical properties of the system. The third is to model the material's response to the propagation of an incident light wave through it. To do this, the Fabry-Pérot equations and transfer matrix method can be applied to model single layers and multilayers respectively.

In order to allow a closer comparison between experimental and theoretical data both methods have been further modified to account for the absorption and emission of light from the material. These modifications will be discussed in section 3.3.5.

3.3.1 Determination of the Dielectric Function

The dielectric function, ϵ, describes the macroscopic reaction of a material to the electric field of an incident electromagnetic wave. In a solid which contains no permanent dipoles, the dielectric response is controlled by the process of electronic polarisation. Under the influence of an electric field, dipole moments are induced in the material due to a redistribution of electronic charge. The total dipole moment per unit volume in a homogeneous material is known as the polarisation, $\mathbf{P}$, and can be written as,

$$\mathbf{P} = \epsilon_0(1 + \epsilon)\mathbf{E}, \tag{3.1}$$

where $\epsilon_0 = 8.85 \times 10^{-12} Fm^{-1}$ is the permittivity of free space and $\mathbf{E}$ is the electric field intensity.

Figure 3.3 shows how the value of the dielectric function varies with wavelength in the spectral region between IR and UV wavelengths for a non-polar semiconductor such as silicon. When examining the material response at these wavelengths, it can be seen that the dielectric function is complex. Looking at the real part of ϵ between infrared and visible wavelengths it undergoes an increase in its value with increasing frequency (normal dispersion).

Electronic transitions occurring at UV wavelengths are responsible for the strong structure seen in this spectral region. At these wavelengths the material is ab-

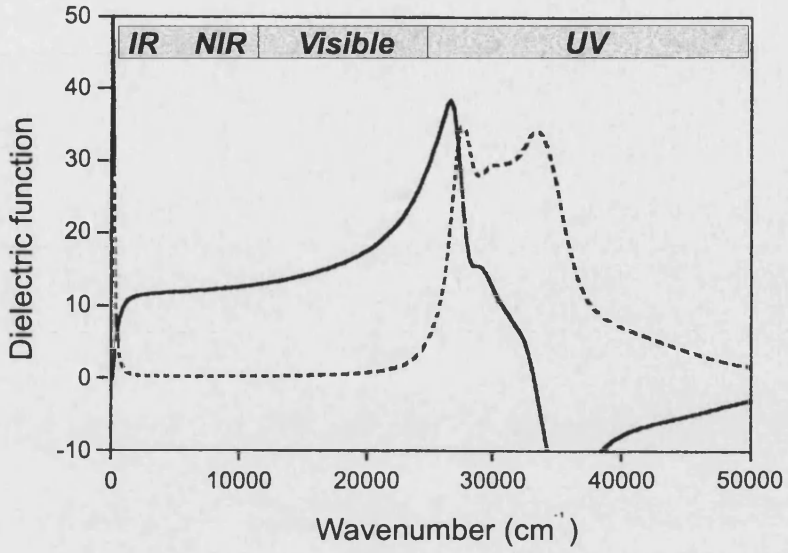

Figure 3.3: A typical plot of the real (solid line), and imaginary (dashed line) parts of the dielectric function, ϵ, for a non polar semiconductor such as silicon. ϵ is shown plotted between the wavenumbers of 10000-50000 cm^{-1} which is equivalent to wavelengths between 1-0.2 μm [40].

sorbing most of the oscillation energy and this is reflected in the sharp rise in the imaginary component of ϵ which represents the loss inherent to the process.

The real part of the dielectric function of silicon ϵ_{Si} is related to the refractive index, n_{Si} by the equation $\epsilon_{Si} = n_{Si}^2 - k_{ex}^2$, where k_{ex} represents the losses in the material. In this case k_{ex} is negligible compared to n_{Si}, thus the expression can be simplified to $n_{Si} = \sqrt{\epsilon_{Si}}$. Experimental measurements of refractive index values have been reported for the transparent region of silicon by a number of investigators. Using strict selection criteria Palik has tabulated the most precise of these results [71].

Although tables are a useful method of obtaining refractive index values at specific wavelengths, when there is a requirement to calculate the index over a range of wavelengths a dispersion equation can be used. For this work the refractive index was calculated using the Herzberger dispersion equation for silicon [72]. The real part of the refractive index may be written as,

$$n_{Si} = A + BL + CL^2 + D\lambda^2 + E\lambda^4, \tag{3.2}$$

where A, B, C, D E and F are constants, and $L = (\lambda^2 - F)^{-1}$ [73].

Substrate Doping and Free Carrier Absorption

It has been pointed out by Russo [74] that values of refractive index measured at wavelengths above the band gap will depend on the wafer resistivity, i.e. in highly doped bulk wafers it is necessary to account for the presence of free carriers. These free carriers are not localised to a specific atom and will respond to the influence of an externally applied field. This response will have an influence on the value of the dielectric constant.

Theiß has performed a study of the influence of substrate doping levels on the optical properties of p-Si [40]. He calculated the carrier density within both a bulk silicon wafer and a 77% porous layer by making adjustments to the dielectric constant in order to fit theoretical curves to experimentally measured reflectivity spectra. Examining the method of pore growth in p-Si layers (section 1.4), it is clear that a depletion of carriers in the porous layer to a level lower than that in the substrate is expected. In addition, the small size of the remaining silicon wires may effect the mean free path of the carriers leading to increased scattering and thus lower conductivity. Theiß's results showed that the macroscopic resistivity of the porous was a factor of 1.1×10^4 times higher than the bulk sample. This result shows that free carriers will have a much reduced effect on the value of the dielectric function of p-Si compares with that of bulk silicon.

The exact extent of this effect will change for differing layer porosities and doping levels. Therefore it was concluded that for the purposes of this work, the inclusion of the free carrier effect when calculating the value of the real dielectric constant would not result in greater accuracy in the computer model. This accuracy could only be gained through a detailed knowledge of the change in carrier concentration due to the etching process and scattering in the remaining silicon wires. Both of these effects remain for further detailed investigation as they require a wide range of samples and fabrication runs.

3.3.2 Effective Medium Approximations

In order to model correctly the optical properties of a porous material it is necessary to calculate the effect that the microstructuring has on the dielectric response of the material. Effective medium theory describes the relationship between the macroscopic properties of a porous system and those of the individual microscopic constituent materials. Using the electrostatic approximation, inhomogeneous materials with a characteristic length scale of inhomogeneities much smaller than the wavelength of light can be characterised by an effective dielectric function ϵ_{eff} [75]. For the case of p-Si, the theory replaces the two component system of silicon (dielectric function ϵ_{Si}) and air (dielectric function ϵ_a) by an effective medium with the dielectric function ϵ_{eff} (figure 3.4). A review of the theory describing the most commonly used formulae is undertaken in a review article by Theiß[76].

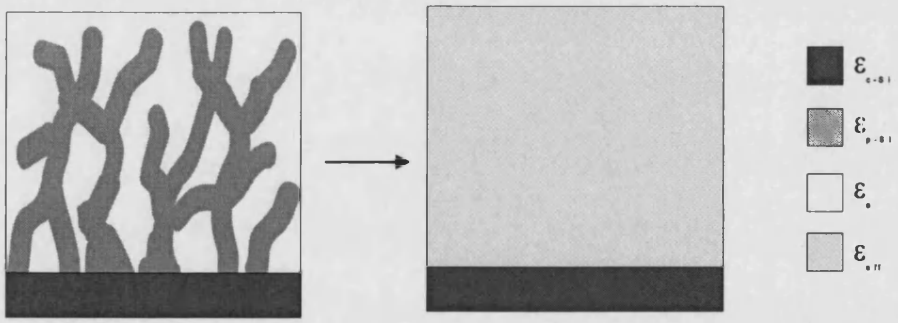

Figure 3.4: Schematic showing the averaging of two components to an effective medium

Simple mixing formulae, including those of Maxwell-Garnet [77], Bruggeman [78], and Looyenga [79], use one parameter to describe the microstructure, that being the material porosity, p. Although each formula only uses one variable, they differ in the nature of their derivation. Both the Maxwell Garnet and Bruggeman formulae calculate the dielectric function by discussing the internal field and polarisation of a single particle. This approach requires many approximations to be made and thus accuracy is lost in the final result. Looyenga uses a more general derivation which considers changes in the effective dielectric function owing to the mixing of fixed quantities of material containing many particles, each quantity being one of two different dielectric constants. The general nature of this formula has been shown to model the dielectric response of a porous material with greater accuracy than the other single parameter formulae [76] and is thus used in this work.

The Looyenga equation is written,

$$\epsilon_{eff}{}^{\frac{1}{3}} = (1-p)\epsilon_{Si}{}^{\frac{1}{3}} + p\epsilon_a{}^{\frac{1}{3}}, \tag{3.3}$$

where ϵ_a is the dielectric constant of air, and ϵ_{Si} the dielectric constant of silicon calculated using equation 3.2.

3.3.3 Modelling of Single Layers

The reflectance (R) and transmittance (T) of a wave at normal incidence from a single layer of p-Si are calculated using standard Fabry-Pérot equations for multiple beam interference.

These equations are:

$$R = r^2 \frac{e^{-2\delta_I} - 2\,cos\delta_R + e^{2\delta_I}}{e^{-2\delta_I} - 2r^2\,cos\delta_R + r^4 e^{2\delta_I}} \tag{3.4}$$

and

$$T = \frac{(1-r)^4}{e^{-2\delta_I} - 2r^2\,cos\delta_R + r^4 e^{2\delta_I}}. \tag{3.5}$$

r is the reflectivity amplitude coefficient, given by

$$r = \frac{n_j - n_a}{n_j + n_a}, \tag{3.6}$$

where n_j and n_a are the refractive indices of the layer and air respectively, and λ_0 is the wavelength of light in free space.

The phase δ comprises of a real and imaginary part, δ_R and δ_I respectively where,

$$\delta = \delta_R + i\delta_I. \tag{3.7}$$

The real part, δ_R, represents the phase change of the wave as it makes a single pass across the layer and is written as,

$$\delta_R = \frac{4\pi n_j d}{\lambda_0}. \tag{3.8}$$

δ_I represents the loss and/or gain in the layer and is discussed further in section 3.3.5.

3.3.4 Modelling of Multiple Layers: The Transfer Matrix Method

Modelling of electromagnetic field propagation in the periodic microstructures is carried out using a transfer matrix method [80]. Given an initial incident amplitude, this method calculates the total field amplitude resulting from the interference of all forward and backward travelling components of the wave that are reflected from the layer interfaces as it passes through the structure. Thus, the relative amplitudes of the total reflected and transmitted waves can be calculated. A full derivation of these matrices is shown in Appendix C.

The basic multilayer structure to be modelled consists of alternating layers of refractive index n_j and width d_j where $j = 1, 2$. The stack pitch, Λ, is the sum of d_1 and d_2 (figure 3.5). Cartesian axes are orientated with y normal to the layer interfaces and z parallel to the layers. There is no field variation in the x direction.

The electric field of a linearly polarised wave in layer j can be written in the form:

$$E_j = E_{j0}\, exp\left[-j\left(\beta z \pm p_j y\right) + j\omega t\right], \tag{3.9}$$

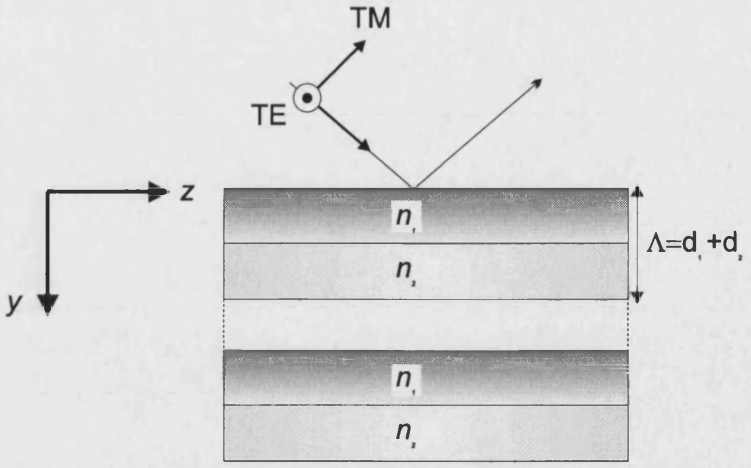

Figure 3.5: Schematic view of multilayer stack structure. The two different polarisation states are also shown. The TE mode is one whose E-field is parallel to the interfaces, and the TM mode is one whose E field lies in the (y,z) plane.

where

$$p = \sqrt{k^2 n_j^2 - \beta^2}, \tag{3.10}$$

is the wavevector component of the field normal to the layer interface, k, the vacuum wavevector, n_j, the refractive index of the layer, and β, the wavevector component in the z direction (section 3.5). Equation 3.10 reflects the fact that the wavevector must have a magnitude equal to kn_j. The direction of the electric field oscillation defines the polarisation of the wave. A transverse electric (TE) wave is one whose E-field is parallel to the interfaces with $H_x = E_y = E_z = 0$, and a transverse magnetic (TM) wave is one whose E-field lies in the (y, z) plane, with $E_x = H_y = H_z = 0$, where H represents the magnetic field of the wave (figure 3.5).

In each case the field can be written in terms of its x component, which is denoted by f. In the jth layer of the Nth period, f_j^N can be written as [80],

$$f_j^N(y) = a_j^N \, cos(p_j(y - y_j^N)) + b_j^N \, \frac{sin(p_j(y - y_j^N))}{\xi_j p_j \Lambda}, \tag{3.11}$$

where a_j^N and b_j^N are complex amplitudes to be determined and y_j^N is the value of y at the centre of the jth layer of the Nth period. f is the general solution to the Helmholtz equation,

$$\frac{d^2 f_j}{dy^2} + p^2 f_j = 0, \tag{3.12}$$

with boundary conditions at the interfaces requiring that,

$$f_1 = f_2, \quad \xi_1 \frac{df_1}{dy} = \xi_2 \frac{df_2}{dy}. \tag{3.13}$$

The parameter ξ is a polarisation parameter defined as,

$$\xi = 1 \ \ (TE) \ \ or \ \ \xi = \frac{1}{{n_j}^2} \ \ (TM), \tag{3.14}$$

the inclusion of which allows both TE and TM cases to be treated by the same analysis.

A two component vector consisting of the two constants a_j^N and b_j^N, completely specifies the field in the layer. Thus, the vector in one layer can be expressed in terms of the vector in the adjacent layer in the previous period by operation with a 2×2 matrix:

$$\begin{pmatrix} a_j^{N+1} \\ b_j^{N+1} \end{pmatrix} = M \begin{pmatrix} a_j^N \\ b_j^N \end{pmatrix}. \tag{3.15}$$

The amplitude coefficients of the incident, reflected and transmitted waves, A_i, A_r, and A_t can thus be related through a total matrix M_{tot} which is a multiple of each individual layer matrix , i.e.

$$\begin{pmatrix} A_i \\ A_r \end{pmatrix} = M_{tot} \begin{pmatrix} A_t \\ 0 \end{pmatrix} = \begin{pmatrix} M_1 \\ M_2 \end{pmatrix} A_t. \tag{3.16}$$

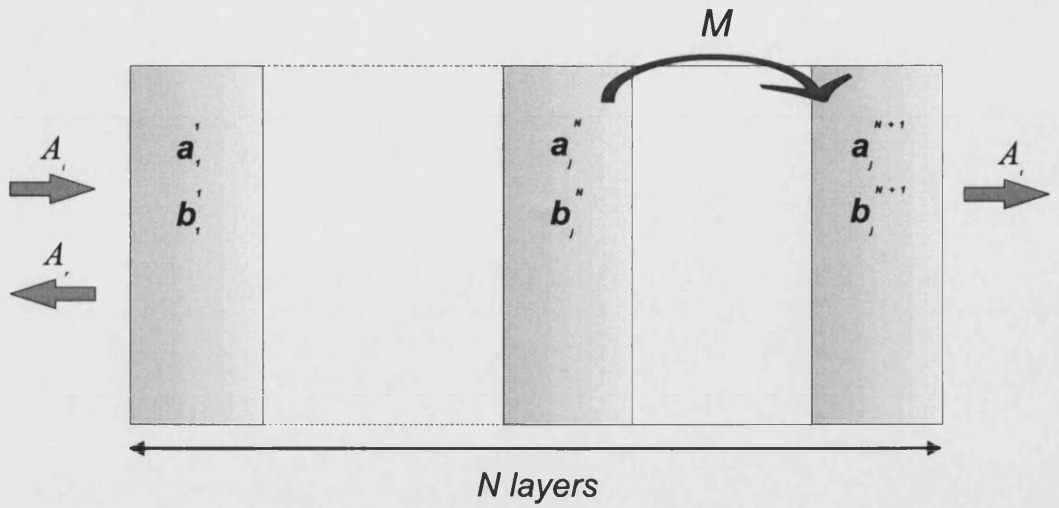

Figure 3.6: Schematic showing the use of transfer matrices to relate the field amplitude between stack layers.

Setting A_t=1 allows the calculation of A_i and A_r which can then be normalised to set A_i=1, i.e.

$$A_i = \frac{M_1}{M_1} \quad A_r = \frac{M_2}{M_1} \quad A_t = \frac{1}{M_1}. \tag{3.17}$$

The obtained amplitude coefficients are then used to calculate the total reflected and transmitted power from the structure. The time averaged value of the power per unit area crossing an interface is the irradiance, I, which can be written,

$$I = \frac{c\epsilon_0}{2} E_0^2, \tag{3.18}$$

where E_0 is the amplitude coefficient of the reflected or transmitted wave [55]. The reflectance (R) and transmittance (T) of the wave are defined as,

$$R = \frac{I_r}{I_{in}}, \quad T = \frac{I_t}{I_{in}}. \tag{3.19}$$

3.3.5 Accounting for Absorption and Emission

Although the Fabry-Pérot method and translation matrices provide a suitable means for calculating the reflected and transmitted wave amplitudes, further detail can be added to these methods in order to make the final model more realistic and thus better able to fit the experimental data. These effects include absorption in passive structures, and both absorption and emission in light emitting structures.

Emission and absorption are added to the Fabry-Pérot model via an additional phase term δ_I. δ_I is written,

$$\delta_I = (\alpha - n_g)d, \tag{3.20}$$

where α is the absorption coefficient and n_g is the emission term chosen to represent gain in the material. α is written,

$$\alpha = \frac{4\pi k_{ex}}{\lambda}, \tag{3.21}$$

where k_{ex} is the extinction coefficient of the material. Values for k_{ex} obtained from reference tables for bulk silicon [71] can be approximated by the expression,

$$k_{ex} = 0.815 \times \exp(\frac{-(\lambda - 0.3827)^{0.6398}}{0.1027}) \times f_s, \tag{3.22}$$

where f_s is the fraction of silicon in the layer and λ is expressed in units of microns. It is assumed that the absorption scales linearly with porosity.

The effect of gain is modelled by assuming a Gaussian distribution for the emission.

$$g(\lambda) = g_0 \frac{1}{\sqrt{2\pi\sigma}} exp\left[\frac{1}{2}\left\{\frac{(\lambda - \lambda_0)}{\sigma^2}\right\}\right] = g_0 G(\lambda). \tag{3.23}$$

where the centre wavelength, λ_0, and standard deviation, σ, are obtained from experimental results from a layer of the same porosity as used for the low index regions of the structures examined in the following section [45]. g_0 is an adjustable parameter used to vary the amount of gain in the layers.

Gain and absorption are added to the transfer matrix model by replacing the real refractive index value n_j in equation 3.10 with a complex refractive index n_{jc}

$$n_{jc} = n_j + i(k_{ex} - n_g), \tag{3.24}$$

where n_j is now the real part of the refractive index of layer j. k_{ex}, and n_g are the terms representing absorption and emission respectively.

Within the multilayer structures, a gain term is added only to the refractive index of the low index layers as it is assumed that the emission will be predominately from these regions. This approximation applies, both because these layers emit light more efficiently and because less of the emitted light is reabsorbed owing to the lower volume fraction of silicon. The total refractive index for each low (n_L) and high (n_H) porosity layer can then be calculated using the equations,

$$n_L = \sqrt{\epsilon_L} + i[k_{ex}(\lambda) - \lambda g(\lambda)/4\pi], \tag{3.25}$$

and

$$n_H = \sqrt{\epsilon_H} + i[k_{ex}(\lambda)], \tag{3.26}$$

where ϵ_L and ϵ_H are the effective dielectric constants of the low and high porosity layers respectively.

The transfer matrix approach can now be applied to calculate the reflection, transmission or emission properties of any arbitrary sequence of p-Si layers.

3.3.6 Modelling of Light Emission

One important difference between p-Si and conventional semiconductor multilayer structures is that in p-Si devices the luminescence is distributed throughout the entire structure rather than in well defined localise emitting regions (e.g. within a central cavity). It is shown below, using theoretical modelling, that a well designed p-Si mirror will emit light almost as well as a conventional microcavity.

An investigation was carried out to determine the emission characteristics of three different p-Si structures (figure 3.7). These structures were (1) a single 75% p-Si layer (low refractive index); (2) multilayer stacks composed of alternating layers of high/low refractive index (64% and 75% porosity respectively) terminated at both ends with a low index layer; and (3) a microcavity system consisting of two multilayer stacks of the same porosity as in case (2) but enclosing an active layer of 75% porosity. The stacks in this case are also terminated with low index layers. All structures contain an equal amount of high porosity light emitting material, of total thickness L.

A comparison is made between these structures by finding the gain required to amplify an input by tenfold, i.e. if a single photon enters the structure and triggers spontaneous emission, how much gain is needed for the structure to produce nine extra photons? Thus the sum of the reflectivity and transmission equals 10. In order to make a fair comparison between the structures the optical path length of the single emitting layer, L, is kept equivalent to the path length of all the low index (emitting) layers in the multilayer stack and microcavity. Gain is then added to the structure by gradually increasing the gain term n_g in the complex refractive index as described in section 3.3.5.

Single High Porosity Layer

The first example examines gain in a single 75% porosity layer. Figure 3.8a shows the Fabry-Pérot resonances of the layer when there is no gain present in the structure. The figures are shown plotted in units of frequency deviation, i.e. deviation of frequency from the central emission frequency, so that effects to the

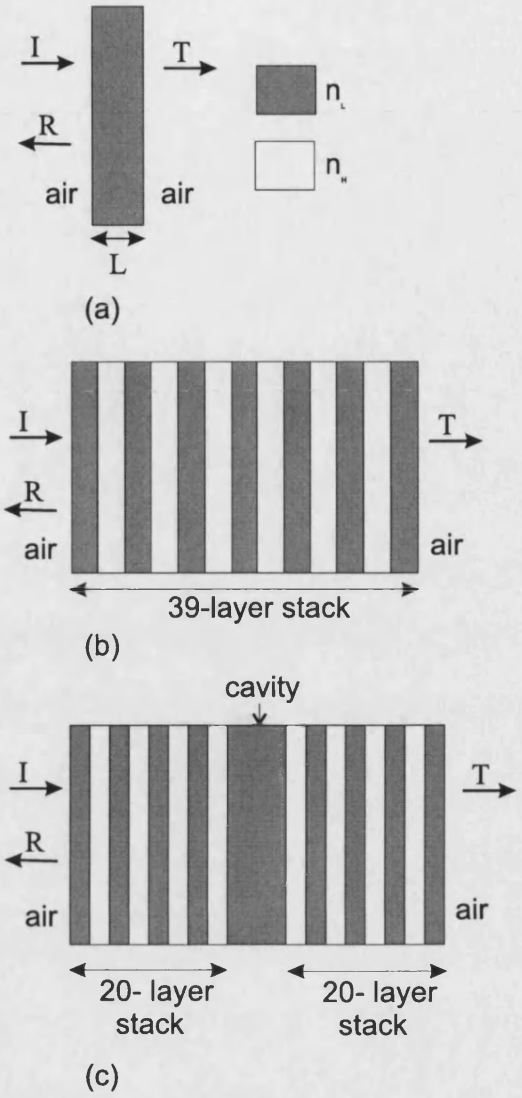

Figure 3.7: A schematic view of the structures used in the comparison of relative emission efficiencies.

FWHM can be observed more clearly. The choice of central emission frequency, 400 THz (760 nm), is described in section 3.3.5. From figure 3.8 it can be seen that at the dips in the reflectivity resonances, no light is reflected back from the stack, i.e. any light not absorbed in the stack is transmitted. The low finesse of the resonances is due to the relatively small Fresnel reflectivity (~3%) at the air/p-Si interfaces. As gain is added to the layer, a single resonance gradually dominates, and the reflectivity and transmissivity grow accordingly (figure 3.8b). Smaller subsidiary resonances are also apparent on the wings of the main peak as emission is also occurring into other modes. The quantity gL shown in figure 3.8b is the 'gain length' needed to amplify the input by the required amount.

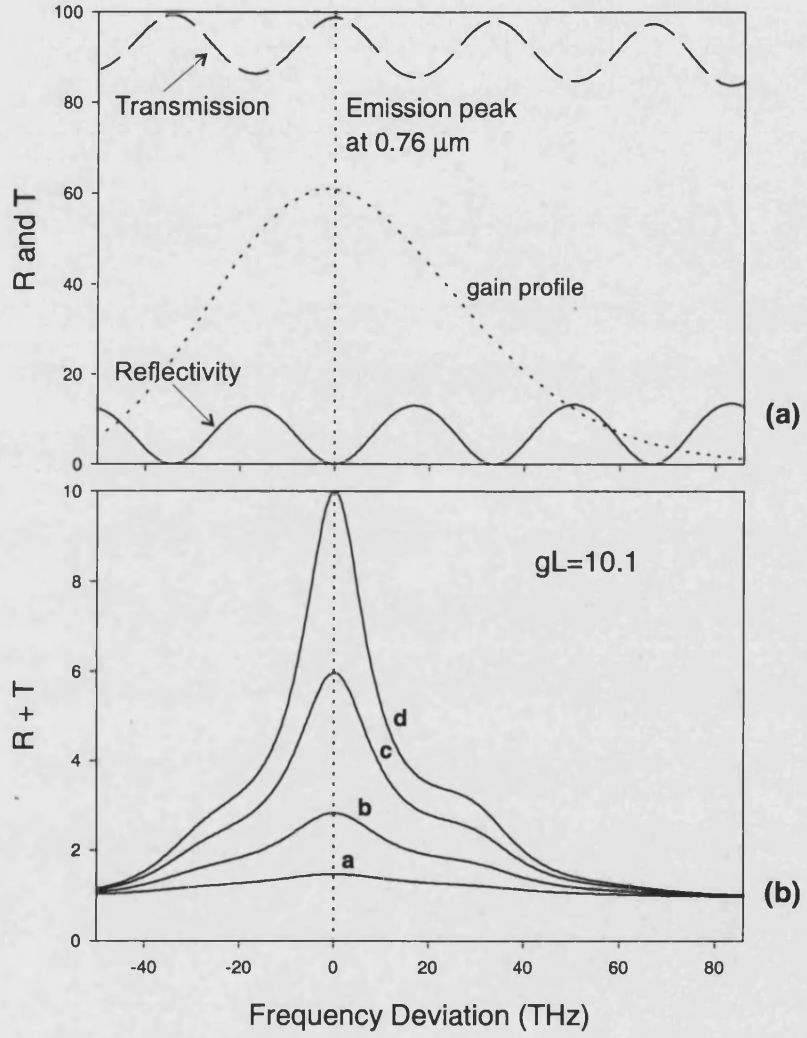

Figure 3.8: Reflectivity (R) and transmissivity (T) of a single 75 % porosity layer of 2.86 μm width with no gain. The Gaussian gain profile is also shown, with the single layer emission peak indicated by a dotted line. (b) Sum of reflectivity and transmissivity of the same layer but with added gain. Curves a,b,c, and d correspond to gains of 1.2, 2.3, 2.9, and 3.5 μm^{-1}.

The lower the value of gL, the less material is required to achieve this aim and the more efficient the structure.

Uniformly Periodic Multilayer Stacks

Here two cases are examined. In the first, the multilayer stack is designed so that the first Fabry-Pérot transmission resonance on the high frequency edge of the stop band coincides with the peak of the emission spectrum (400 THz). In the second, it is designed so that the first Fabry-Pérot transmission resonance on the low frequency edge of the stop band coincides with the emission peak. These two cases were chosen in order to compare the efficiency of light emission from the structure when the light intensity is concentrated in the low index and high index layers respectively, as described in section 3.2.

The relevant Fabry-Pérot mode in each case is positioned over the peak of the p-Si emission spectrum by altering the layer thicknesses within the stack to adjust the position of the Bragg condition as described in section 2.3. Figure 3.9a shows the reflectivity and transmission spectra in the first case. As described in the text, the peak of the emission spectrum (760 nm) is made to coincide with the top of the Fabry-Pérot mode on the high frequency edge of the band gap. Under this condition the fields in the stack are concentrated in the low index emitting layers (section 3.2). The figure shows that the finesse of the Fabry-Pérot mode is sharpened (figure 3.9b), indicating a greater degree of confinement and thus an increase in photon lifetime. The gain required to achieve a photon flux 10 times the input flux is approximately 30 times smaller in this case than in the single high porosity layer as it is now being concentrated into a much narrower bandwidth (table 3.1).

The stack is now redesigned to fit the second multilayer case (figure 3.10a). The total number of layers was kept constant, the width of the low porosity (zero gain) layers being reduced in order to shift the Bragg condition to the other side of the gain peak. Once again, the finesse of the dominant mode is considerably enhanced over that of the single layer. The gain required to achieve a photon flux 10 times the initial flux here is approximately 10 times larger than in the single layer (figure 3.10b). This result is not unexpected since on the low frequency side of the band gap the fields are concentrated in the low porosity, highly absorbing

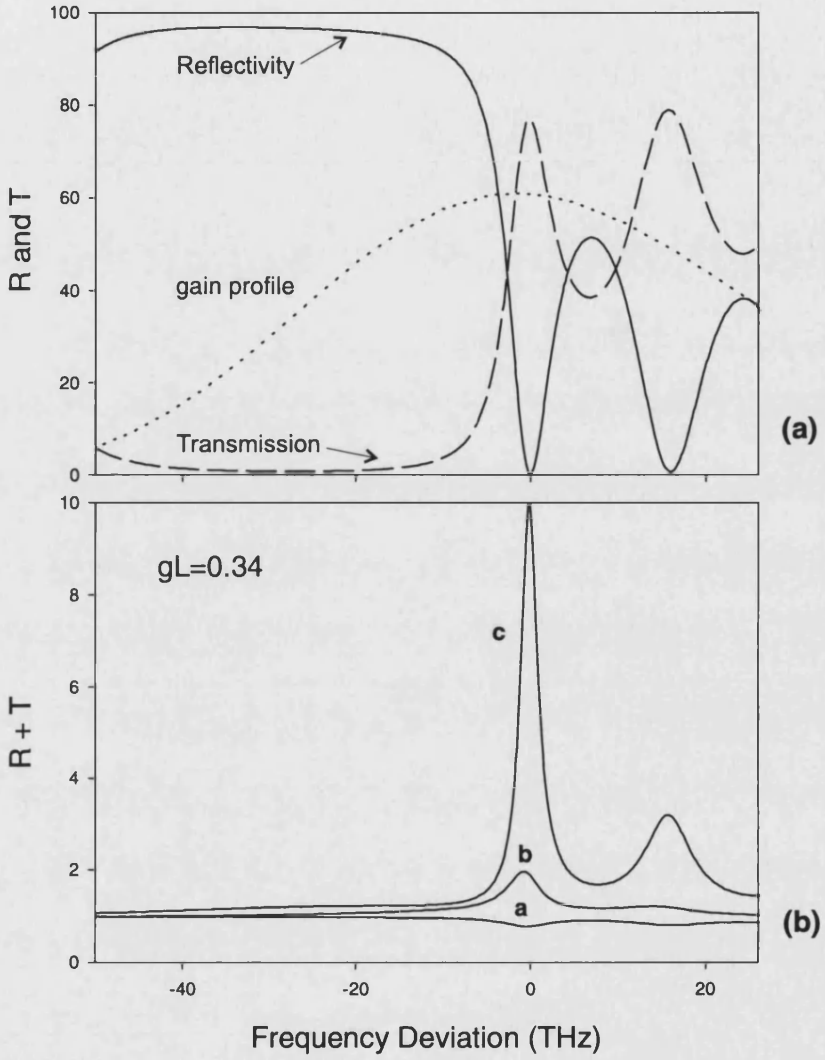

Figure 3.9: Reflectivity (R) and Transmissivity (T) of a 39-multilayer stack designed so that the first Fabry-Pérot resonance on the high frequency side of the stopband sits on the gain peak. The gain peak remains in the same position as that shown in figure 3.8. The layer widths are 0.14 μm (low index) and 0.12μm (high index). (b) Sum of reflectivity and transmissivity with added gain. Curves a,b, and c correspond to gains of 0, 0.06, 0.12 μm^{-1}.

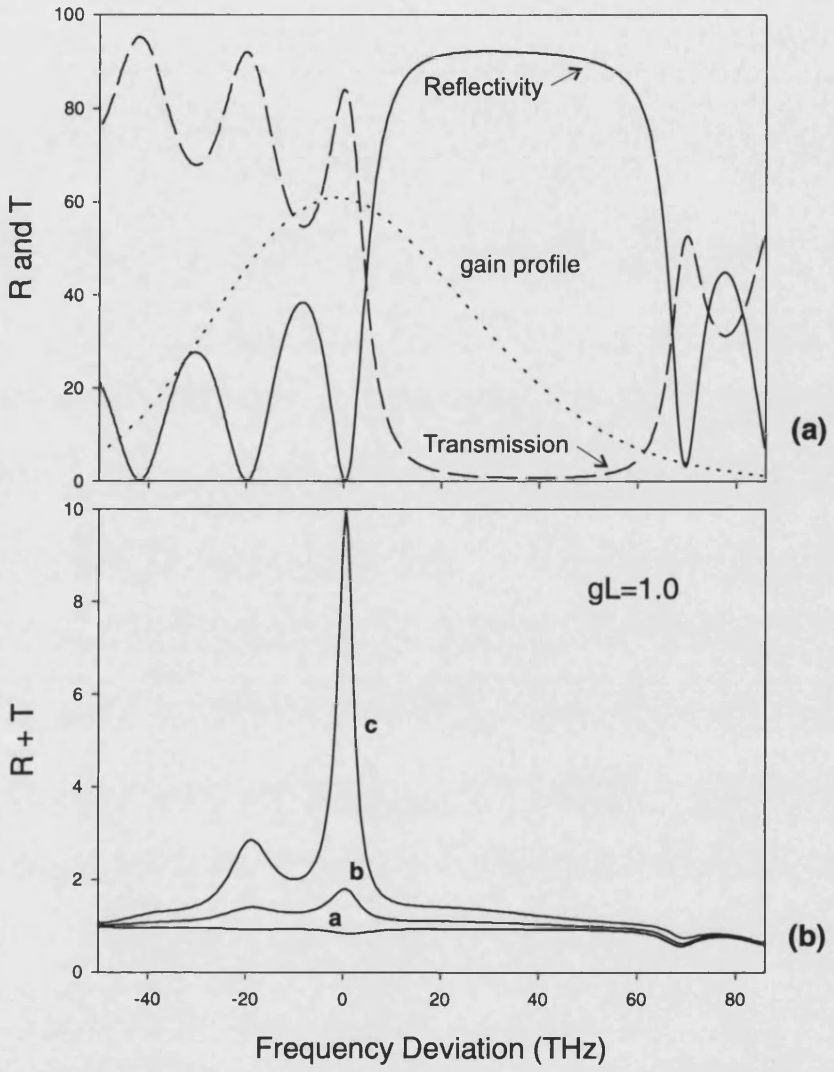

Figure 3.10: Reflectivity (R) and transmissivity (T) of a 39-multilayer stack designed so that the first Fabry-Pérot resonance on the low frequency side of the stopband sits on the gain peak. The layer widths are 0.14 μm (low index) and 0.08 μm (high index). (b) Sum of the reflectivity and transmissivity with added gain. Curves a,b, and c correspond to gains of 0, 0.16, and 0.35 μm^{-1}.

layers.

Multilayer stack with defect layer

Finally, the same procedure was applied to a microcavity formed by placing a $\lambda/2$ thick layer of emitting material between two multilayer stacks. In this case, λ is chosen to coincide with the position of the gain peak. A resonance forms in the centre of the stop band, and this is designed to sit on the emission peak (figure 3.11a). The results in figure 3.11b display further narrowing of the emission mode. The gain required in this case was approximately 34 times smaller than for the single layer, and is very close to the value for the first multilayer stack. This shows that the latter two structures emit light with comparable efficiencies. It is also apparent that the use of a multilayer structure considerably narrows the emission linewidth, the microcavity linewidth ($\Delta\nu_{FWHM}/\nu = 0.004$) being approximately 13 times smaller than that of the single layer ($\Delta\nu_{FWHM}/\nu = 0.05$).

The results are summarised in table 3.1. It can be seen that the emission from suitably designed multilayer stacks and microcavities is considerably enhanced in both strength and finesse over that of a comparable single high porosity layer. The gain in the high porosity layers, needed for a net gain of 10 times in the overall structure, is 34 times higher in the single layer than in an appropriately designed stack or microcavity. In addition, substantial narrowing of the emission mode, is apparent in the multilayer stacks and microcavity. A comparison between the relative widths of the resonance modes of the different structures provides valuable information regarding the degree of photon confinement within each of them. The width of the emission modes of each structure, $\delta\nu$, are related to the photon lifetime τ_p through the equation [81],

$$\delta\nu = \frac{1}{2\,\pi\,\tau_p}. \tag{3.27}$$

τ_p is related to the overall losses from the structure, α_r, where,

$$\tau_p = \frac{1}{c\,\alpha_r}, \tag{3.28}$$

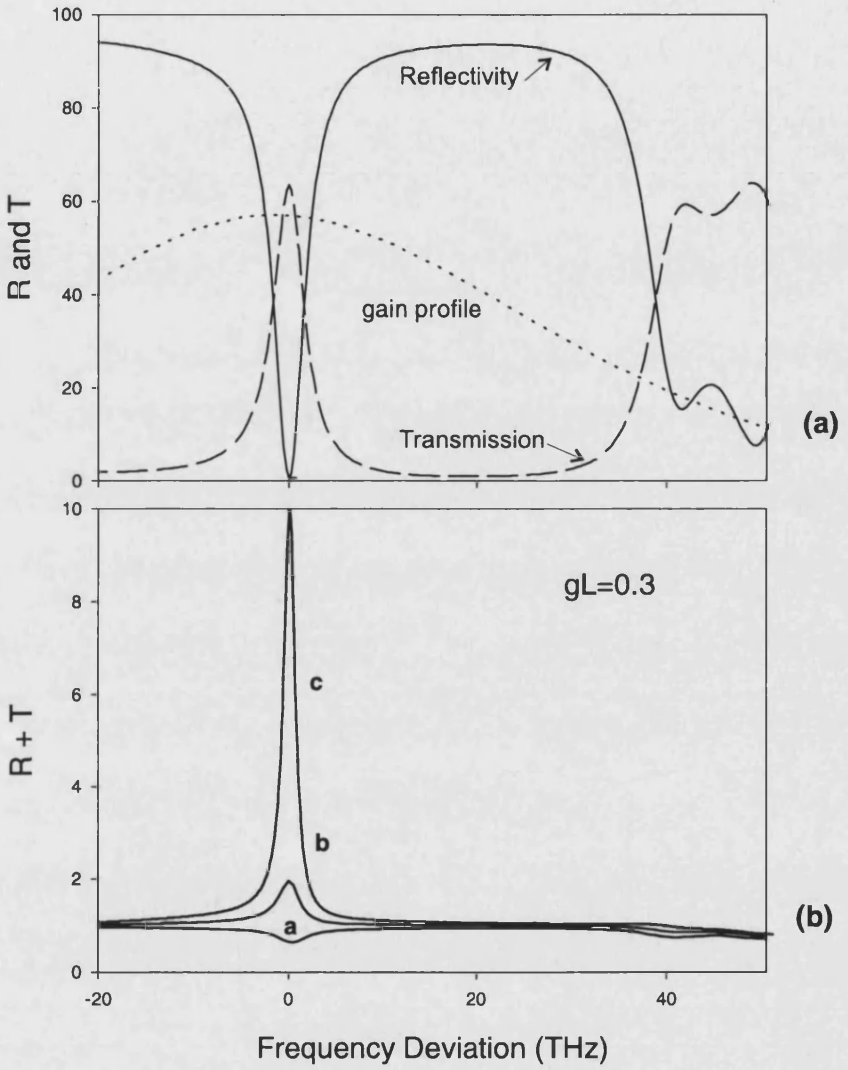

Figure 3.11: Reflectivity (R) and transmissivity (T) of a microcavity consisting of a $\lambda/2$ thick layer of emitting material between two 20-layer multilayer stacks; note the cavity mode in the middle of the stopband. The layer widths are 0.26 μm (defect layer), 0.13 μm (low index) and 0.11 μm (high index). (b) Sum of the reflectivity and transmissivity with added gain. Curves a,b, and c correspond to gains of 0, 0.05, and 0.10 μm^{-1}.

Structure type	Resonance Linewidth ($\Delta\nu_{FWHM}/\nu$)	Gain for 10× amplification (relative to microcavity)
microcavity	0.004	1
multilayer stack 1	0.008	1.15
multilayer stack 2	0.011	3.34
single layer	0.05	34

Table 3.1: Results displaying the relative emission efficiencies and resonance linewidths of the four structures under comparison.

It can thus be seen that a greater loss within a particular structure will result in broader resonance modes. Furthermore, shorter photon lifetimes will result in the propagation mode making less passes through the material and thus being able to excite less emission.

These results show that the correct design of a p- Si mirror or microcavity system can result in large gains in the efficiency of light emission at specific wavelengths.

3.4 Summary

This chapter has described the computational modelling of p-Si multilayer structures. The modelling was performed to aid in the design of p-Si samples by establishing a more thorough understanding of light propagation in periodic microstructures.

The control of light emission and propagation has been examined in four different periodic microstructures, with the aim of using the results to help optimise current multilayered structure designs. To achieve this, a Fabry-Pérot and translation matrix method was modified to model light emission and propagation through a structured p-Si absorbing material. Results have shown that the efficiency of emission from a multilayer mirror can be comparable with that of a microcavity. These results display the possibility that an efficient light emitting structure can be formed from a much simpler design, i.e. a mirror, if optimised correctly.

Experimental investigations regarding the optical characteristics of p-Si structures will be examined in the following chapter.

Chapter 4

Experimental Measurements: Reflectivity and Transmission

4.1 Introduction

Experimental characterisation of different microstructures using reflection and transmission measurements was carried out to enable a comparison between the observed optical spectra of the samples and those predicted by modelling. By comparing the experimental data and computer calculations, the accuracy and reliability of the model could be determined, i.e. a close match between the two sets of data would confirm that correct assumptions have been made about the process of light propagation within the samples under investigation.

In this chapter, the reflection and transmission spectra of samples fabricated from three different materials are examined. The initial transmission experiment was carried out on a multilayered structure which was designed to test the computer model. The sample was planned to be a stack composed of alternating silicon and silica layers. However, the sample grown was found to be composed of layers of uneven thicknesses grown from hydrogenated amorphous silicon and silica. Experimental measurements of the transmissivity of this sample are presented and the method used to estimate the actual layer thicknesses and refractive indices will be discussed.

Secondly, results of reflectivity measurements on p-Si multilayer and microcavity structures are presented and examined. Difficulties in taking accurate measurements are discussed and a comparison between experimental data and modelling calculations is given.

4.2 Transmission Measurements on an Amorphous Silicon/Silica Multilayer Stack

Transmission measurements of a multilayer structure fabricated from amorphous silicon and silica layers were chosen as a suitable means of both testing the computer model and gaining experience in experimental characterisation methods. Two different measurements were carried out; transmission as a function of wavelength and angle.

Initially, the transfer matrix model was used to design a multilayer stack such that angular measurements of its stopband could be obtained at a fixed wavelength of 850 nm (section 2.3). This wavelength was chosen due to the availability of a suitable laser light source. The calculations performed modelled a structure composed of alternating high and low refractive index layers composed of silicon and silica respectively. The dispersion formula used to calculate the refractive indices of silicon is shown in section 3.3.1. The formula used for silica in the wavelength region $\sim 0.2 - 2.5\mu$m is given below (where λ is the free space wavelength in microns).

$$n_{SiO_2}{}^2 - 1 = \frac{0.6961663\lambda^2}{\lambda^2 - (0.0684043)^2} + \frac{0.4079426\lambda^2}{\lambda^2 - (0.1162414)^2} + \frac{0.8974794\lambda^2}{\lambda^2 - (9.896161)^2} \text{ [82].} \tag{4.1}$$

The original aim was to design the structure such that the position of the stopband could be tuned by adjusting the angle of the incident light. As shown in equation 2.3, an increase in the angle of incidence will cause the Bragg condition to move toward shorter wavelengths. The effect of this movement is shown in figure 4.1 where it is observed that the angular measurement allows both the stopband and its neighbouring resonances to be viewed.

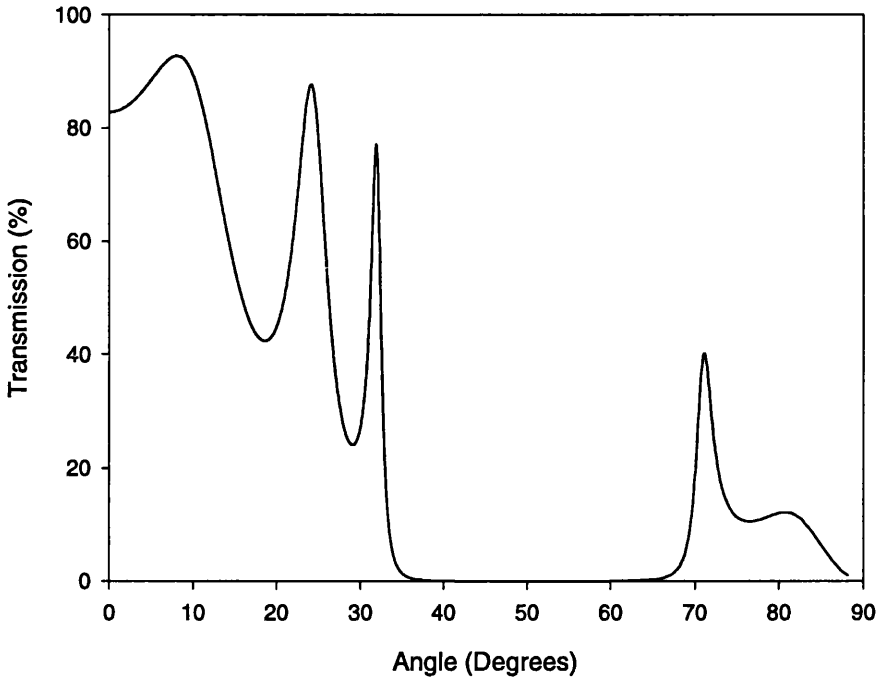

Figure 4.1: Calculated transmissivity as a function of angle, for TM polarised light, of the silicon/silica multilayer structure provided by members of the Institute of Electrical Communication at Tohoku University.

In order to access both of the stopband edges in an angular measurement it is necessary that the stopband should be narrow. Modelling showed that a sample possessing layers of optical thickness $\lambda/4$ resulted in the stopband width being too great for this to occur, i.e. only one edge could be viewed. To reduce the stopband width, the relative layer optical thicknesses were adjusted whilst maintaining the Bragg condition to increase the amount of silica at the expense of silicon (section 2.3). It was found that layer thicknesses of $\lambda/22$ and $10\lambda/22$ produced a stopband of suitable width whilst maintaining the periodicity of the structure. In addition, this sample structure had the advantage of reducing the amount of absorption within the silicon layers which can be significant at short wavelengths. The sample would therefore allow a greater amount of light to be transmitted and thus make measurements easier.

The original proposed design is given below and the predicted reflectivity and transmissivity spectra for this sample are shown in figure 4.2.

Number of repeats: 20 alternate silicon/silica

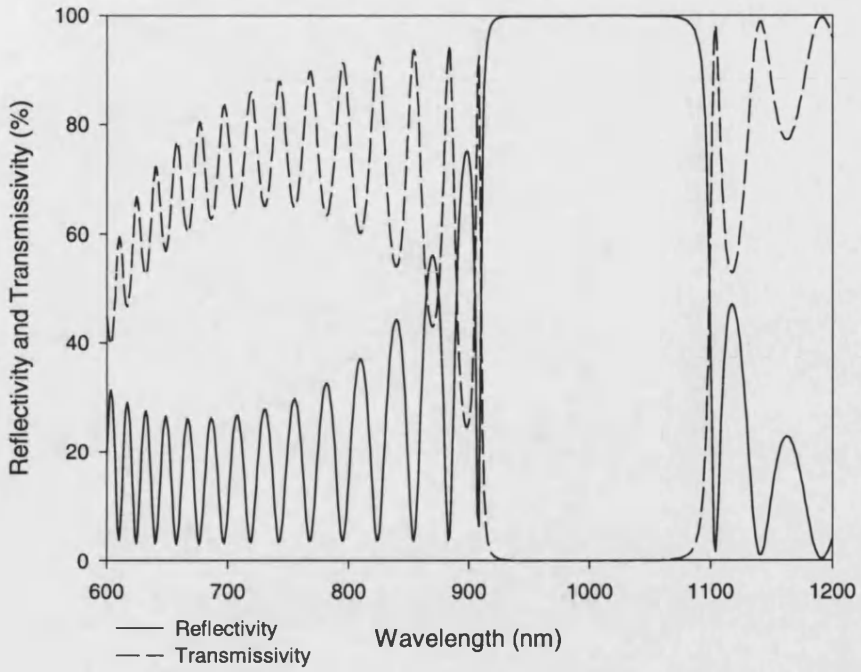

Figure 4.2: Predicted optical spectra for silicon/silica multilayer stack as described in text.

Layer one physical thickness: 12 nm
Layer two physical thickness: 304 nm
Silica substrate

The sample under investigation was provided by members of the Institute of Electrical Communications at Tohoku University, Japan. When received, it was found that the sample was of a different specification to that requested. The deposition conditions for this sample are noted in Appendix D. The new sample was composed of eighty layers of hydrogenated amorphous silicon, and silica of unknown oxygen content. Although the number of layers in the received sample was double that requested this could be allowed for in the analysis. However, the difference in fabrication materials meant that the refractive indices used when designing the sample were different from those in the fabricated structure. As expected from equation 2.2 these differences will be shown to have a significant effect on the optical properties of the stack.

4.2.1 Experimental Method

The experimental arrangement used to measure transmissivity versus wavelength, shown schematically in figure 4.3, is as follows. Firstly, light from a tungsten bulb was imaged onto a pinhole which (a) allowed light from only a small area of the filament to be collimated, thus reducing variations in the bulb spectra due to temperature differences across the filament, and (b) allowed control over the solid angle of the beam, thus making it easier to collimate. All light transmitted by the sample was subsequently collected by a large diameter multimode optical fibre and detected by an optical spectrum analyser.

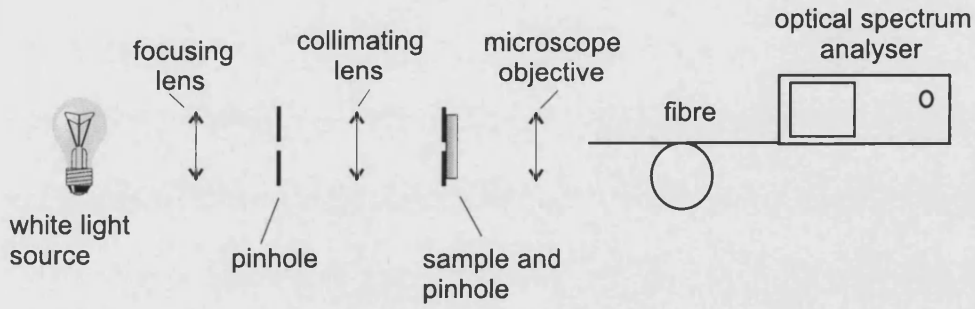

Figure 4.3: Experimental arrangement to measure transmission as a function of wavelength.

Two measurements were necessary to determine the transmissivity of the sample as a function of wavelength. The first was a measurement of the detected power through the pinhole in the absence of the sample, and the second was a measurement of the detected power through the pinhole with the sample present. After performing a background subtraction from both, the transmissivity of the sample was calculated by dividing the second measurement by the first.

Placing the second pinhole directly in front of the sample was found to be necessary as results from initial experiments showed variations in the layer thicknesses across the sample. Results displaying the effects of this inhomogeneity will be discussed in further detail below. Furthermore, if a large area of the sample was illuminated, experimental broadening could be seen in the transmission resonances. This occurs because the large area measurement was effectively measuring an transmissivity average over a range of stacks with differing layer parameters.

Two types of transmission experiment were used to characterise the sample. 1)

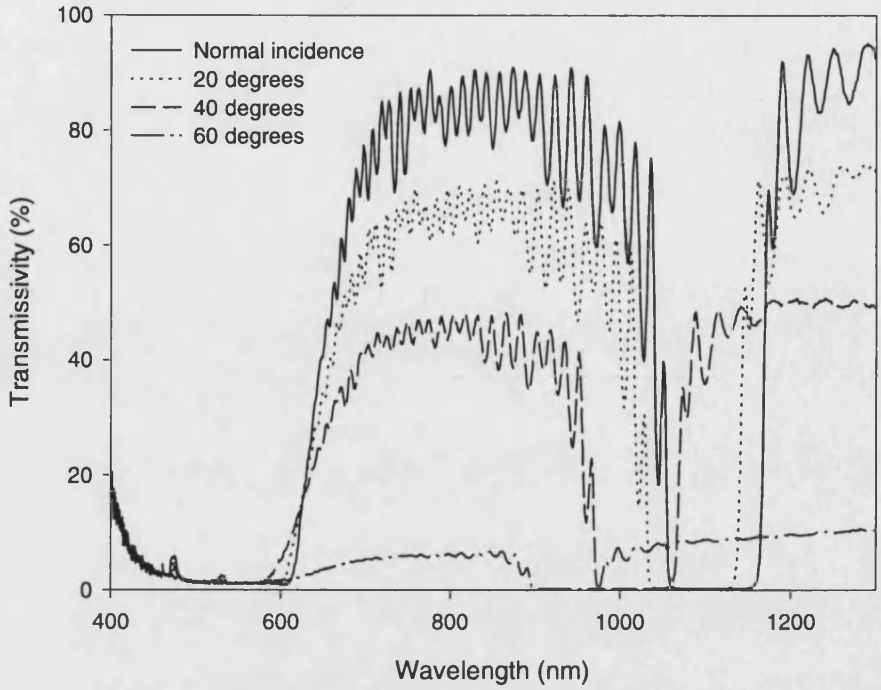

Figure 4.4: Transmission of the sample as a function of wavelength at the indicated angles of incidence for TM polarised light.

normal incidence transmissivity at wavelengths between 500-1700 nm, and 2) transmissivity at 850 nm over an angular range of 0 to 75 degrees. The results of these measurements are discussed below.

4.2.2 Transmissivity Versus Wavelength

The results of the experiment to measure the sample transmission as a function of wavelength can be seen in figure 4.4 for a number of different angles of incidence. At normal incidence, the first order band gap is seen to be centred at a wavelength of ~1100 nm, and a second gap appears below ~600 nm. As the angle of incidence is increased from 0 to 60 degrees the first order band gap is seen to shift to lower wavelengths as the Bragg condition changes according to equation 2.3.

At all angles of incidence the transmissivity falls off sharply below ~650 nm owing to increased absorption in the amorphous silicon layer. Below 600 nm two small features appear in the spectrum. The first feature at ~530 nm is the edge

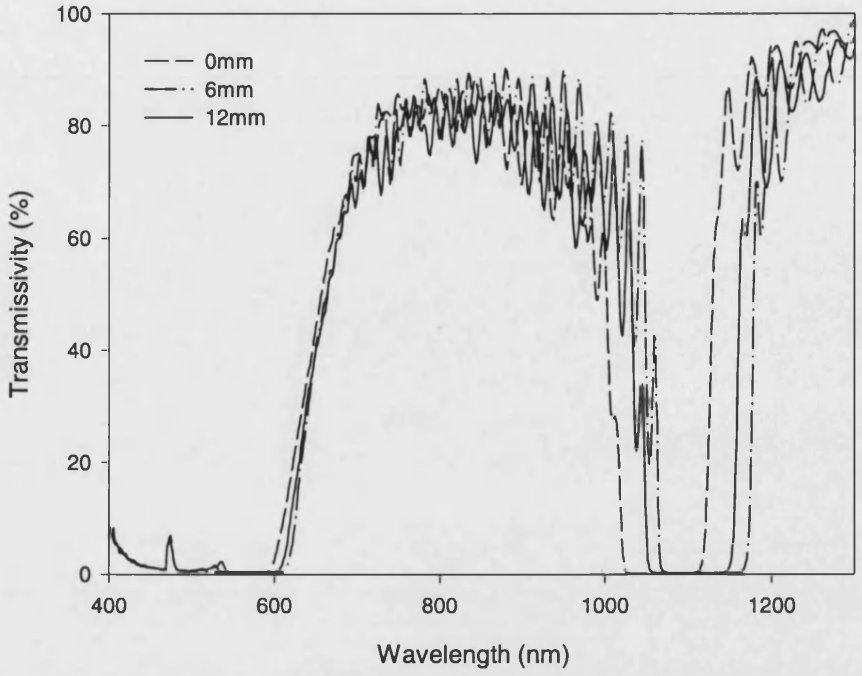

Figure 4.5: Variation of sample transmissivity as a function of wavelength at points 6 mm and 12 mm from a starting point (0mm) across the sample surface.

of the second order stopband, the height of which has been severely limited by absorption. The second slightly larger feature shows no movement with increasing angle and is thus believed to be an experimental artifact.

When these results are compared to predictions for the original design at normal incidence shown in figure 4.2, it can be seen that the Bragg condition is now at a longer wavelength (see equation 2.2). This result indicates that the layers are of a longer optical path length than originally intended.

Figure 4.5 shows further data which supports the above result. These measurements show the transmissivity of the sample measured at distances of 6 mm and 12 mm in a horizontal line across its surface from a starting point (0 mm), and show a change of up to $\sim$5% in the stopband position. These results not only confirm that the sample is comprised of layers of greater optical thickness than originally thought, but that the layer thicknesses vary across the sample.

Given the wide degree of variation between the results the computer model was used as an aid to determine the actual layer widths from the experimental data.

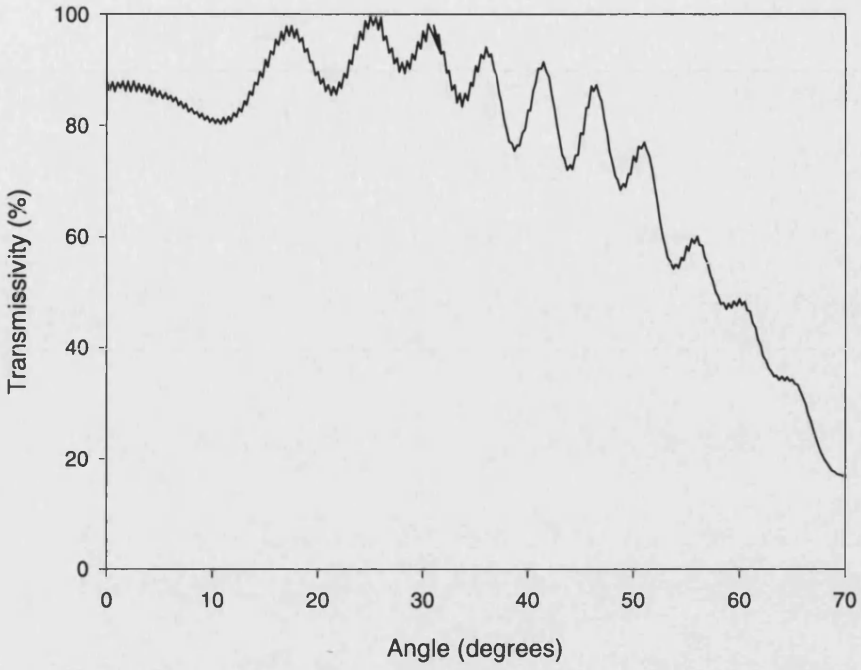

Figure 4.6: Transmissivity of sample as a function of angle at a fixed wavelength of 850 nm.

This process will be discussed in section 4.2.4.

4.2.3 Transmissivity Against Angle

For this experiment the white light source was replaced by a broad area AlGaAs laser of wavelength 850 nm (FWHM ~10 nm) and the first lens and pinhole removed. A polariser was placed after the collimation lens to allow only TM polarised light to illuminate the sample. The alignment of the IR beam was achieved with the aid of a Helium-Neon laser beam. The sample was placed as described in the previous experiment and the transmissivity was measured for angles between 0 and 75 degrees. The transmitted power was frequently checked at a reference angle of 0 degrees to try and eliminate any drift in laser power over time.

The results of this experiment, performed using TM polarised light, are shown in figure 4.6. Several resonances can be observed but there is no evidence for

a stopband as shown in figure 4.1. The absence of evidence for a band gap is because it has been shifted to longer wavelengths (figure 4.4) and thus can not be observed by angular measurements at 850 nm.

4.2.4 Modelling Results

Figure 4.7 shows the result of a comparison between the transmissivity of the original structure designed using the transfer matrix model, to the obtained experimental results. It is clear that the two sets of data are not in good agreement. This mismatch is a result of two effects. Firstly the fabricated sample was composed of materials different to those expected and thus the material refractive indices were different from the initial assumptions, and secondly the layers showed evidence of being both wider than intended, and possessing a thickness variation across the sample.

Given that the sample was of different composition to that intended, computer modelling of the structure was used to estimate its actual characteristics. Values of refractive index for the amorphous silicon and silica layers at a wavelength of 1.55 μm which were supplied with the sample (Appendix D), were used as a starting point.

In order to make the fit, new information had to be obtained regarding the actual layer thicknesses and refractive indices. Firstly, a fit was obtained to Fabry-Pérot fringes observed in the region of transmission between 1350-1700 nm by adjusting the optical path length of the structure. At these wavelengths, the electromagnetic field no longer samples individual layers in the stack and the fringes are due to reflections off the end interfaces of the structure. This fit was carried out using the Fabry-Pérot model described in section 3.3.3.

The optical path length of the stack is expressed as $n_{eff}L$, where n_{eff} is an average effective long wavelength refractive index, and L is the total thickness of the structure. An initial value of n_{eff} was calculated from the refractive index data supplied with the sample using the equation,

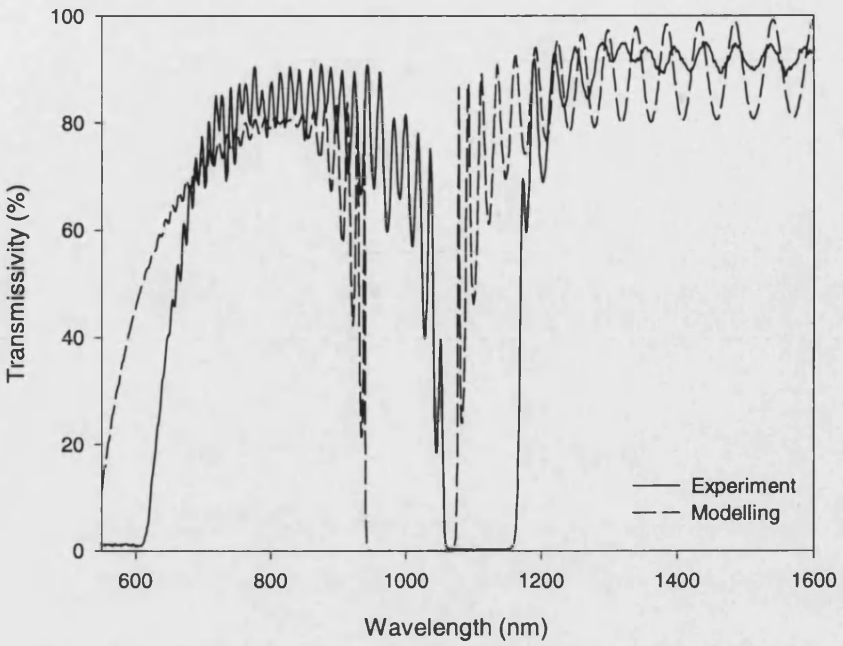

Figure 4.7: Comparison of initial modelling calculations of sample transmissivity as a function of wavelength, versus experimental measurements.

$$n_{eff} = \frac{(n_1 d_1 + n_2 d_2)}{d_1 + d_2}. \tag{4.2}$$

where n_1, n_2, d_1 and d_2 are the refractive indices and layer thicknesses of the amorphous silicon and silica layers respectively [48].

The wavelength spacing and visibility of the fringes are governed by the optical path length of the stack and the refractive index difference between the end layers and surrounding medium respectively. The path length was varied by adjusting L and n_{eff} until a good fit was obtained. Once the optical thickness had been determined the total thickness of the two layers in each repeat $(d_1 + d_2)$ can be calculated. For the position at which the measurement was taken, $(d_1 + d_2)$ was calculated to be 600 ± 5 nm.

In the initial comparison (figure 4.7) it can be observed that the width of the calculated stop band is too large. This width is governed by the refractive index difference between the two different layers, and thus this index contrast was

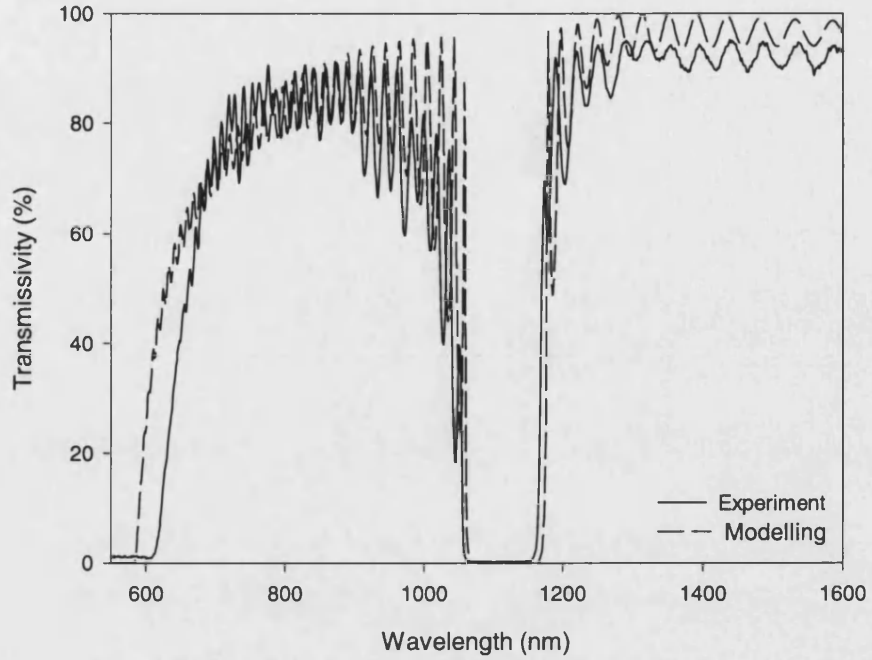

Figure 4.8: Comparison between experimental normal incidence transmissivity and modelled transmissivity calculated using refined layer parameters.

decreased until the stop band widths agreed.

Furthermore, the position of the stop band is controlled by both the layer widths and refractive indices. Based on the calculated values of d_1 and d_2 obtained using the method above, further minor adjustments were made to these parameters until the experimental and modelling stop bands overlapped.

Figure 4.8 shows a comparison of the experimental data and the modelling calculations performed using the refined values of n_1, n_2, d_1 and d_2. It can be seen that the agreement is much improved. The new calculation is observed to be in good agreement at wavelengths above $\sim$ 800 nm. Below this value the calculated curve dropped off much faster than the experimental curve. This drop off is caused by absorption effects dominating at shorter wavelengths. These effects are weaker in the modelling results between 600-850 nm than those seen in the experimental data, thus implying that the modelled absorption is too low. This is reasonable as the exact material properties are unknown.

It should be noted that the good quality of fit between the two sets of data was

Number of repeats	40 alternate amorphous silicon/silica
Layer one physical thickness	14 nm
Layer two physical thickness	345 nm
Layer one refractive index	2.9
Layer two refractive index	1.49
Silica substrate	

Table 4.1: Values used to calculate the model transmissivity shown in figure 4.8.

to be expected given that there existed four free parameters. Furthermore, good agreement could be obtained with more than one set of parameter values. However, the variation in values between the different parameter sets was negligible and thus the results are considered reliable.

The values used to calculate the model transmissivity shown in figure 4.8 are summarised in table 4.1.

In summary, due to the supply of a sample fabricated from different materials to those originally expected, transfer matrix model calculations using adjusted values were used to fit curves to the measured transmission spectra. Furthermore, both the modelling and experimental data showed that the layers were both thicker than originally intended and that they also varied in thickness across the length and width of the sample. In making a comparison between the layer thickness values supplied with the sample (design A) and those calculated from modelling the optical spectra (design B), two points can be raised. It can be seen that whilst the ratio of layer thicknesses within each structural design is consistent (<3% difference), there is a large increase in layer thicknesses between design A and design B ($\sim$14%). This implies that the actual growth rate during fabrication was greater than that perceived.

4.3 Reflectivity Measurements on p-Si samples

4.3.1 Description of Samples

In total, twenty six p-Si samples were grown and examined. These samples, designed using the transfer matrix model, comprise of three single layers, sixteen multilayer mirrors and seven microcavities. The majority of the samples were etched from either p- or p+ substrates depending on the availability of material. A complete listing of sample details can be found in Appendix B.

Although originally it was planned to produce samples with specific optical characteristics, strict time limitations and equipment malfunctions meant that it was not possible to develop the etching process to a sufficient level of reliability in order to obtain the desired structures. In many cases it was found that the measured optical spectra were very different to those originally intended. Although this did not pose a difficult problem when modelling the experimental data, it meant that it was not possible to perform any comparisons similar to those described in section 3.3.6 which relied upon the samples being comprised of equal amounts of low index material.

To fit the computer model data to that obtained experimentally, layer thickness measurements were first obtained from SEM images of the structures and then were entered into the program. The two layer porosities were then adjusted manually until the two sets of data were found to be in good agreement.

4.3.2 Experimental Method

Reflectivity spectra were taken by two different methods of measurement. The first method used a Perkin-Elmer spectrophotometer to provide an accurate measurement of absolute reflectivity against wavelength at an angle of 6 degrees. One feature common to the spectra of larger samples obtained in this manner is the observed smearing of the Fabry-Pérot fringes. At short wavelengths this is predominantly an effect of absorption in the material, but at longer wavelengths the smearing is due to instrumental effects. The resolution and scan speed of

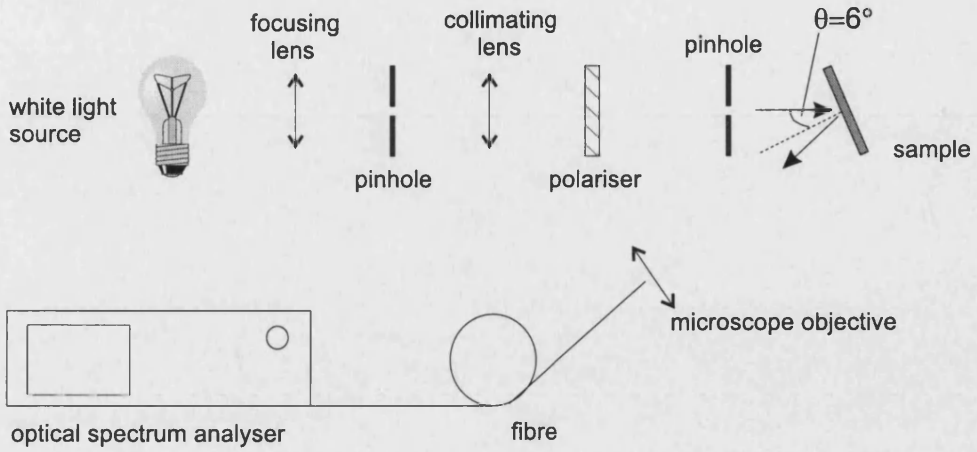

Figure 4.9: Experimental arrangement for reflected power measurement.

the Perkin-Elmer were 2 nm and 60 nm/min respectively. However, the time response of the equipment was 5 s, thus giving an effective resolution of 5 nm and causing features with a FWHM below this value to be smeared. This effect is discussed further below.

The second method of reflectivity measurement used an optical spectrum analyser to obtain a measurement of reflected power against wavelength. Using this method it was not possible to obtain a reliable measure of absolute reflectivity due to difficulties in finding a reference sample which gave reproducible results. However, the spectra obtained gave an accurate measurement of the wavelength position of spectral features, and thus could be used in comparisons with the results of computer modelling. In comparison with the Perkin-Elmer spectra these results, obtained over a time period of several months after etching, show a slight blueshift due to aging effects. This aging is discussed further in the summary.

The experimental arrangement to obtain reflectivity spectra by the second method is shown in figure 4.9. The arrangement is similar to that described in section 4.2.1, except that in this case the collected light has been reflected off the sample which has been placed at an angle of 6 degrees. This angle was chosen so that it was consistent with that used in the Perkin-Elmer measurements.

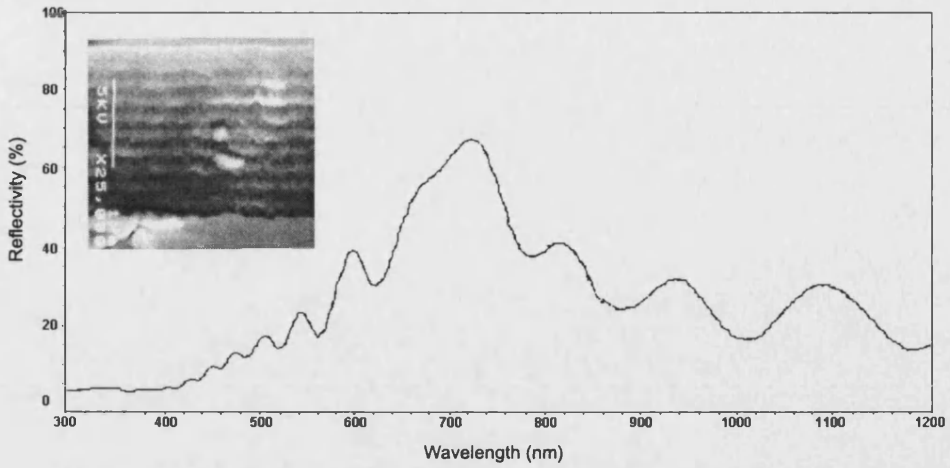

Figure 4.10: Reflectivity spectrum of p- sample C139. The inset shows an SEM image of the structure [57].

4.3.3 Results

Comparison of Reflectivity of p- and p+ Doped Structures.

Figure 4.10 shows a reflectivity spectrum of p- sample C139 taken with the Perkin-Elmer spectrophotometer. The inset shows an SEM image of the structure, also shown in greater detail in figure 2.8. The structure is composed of 10 repeats of alternating high and low refractive index material of thicknesses $0.07 \pm 0.02\,\mu$m and $0.11 \pm 0.04\,\mu$m respectively. The number of repeats was chosen to be 10, as initial modelling results showed a saturation of the peak reflectivity value beyond this number. Thus, the addition of more layers to the structure would not result in any significant increase in its performance as a mirror.

The spectrum, taken over a wide wavelength range between 300-1200 nm, shows a peak reflectivity of 66% at ~710 nm, with smaller resonance modes either side. The resonances are seen to disappear at shorter wavelengths (λ <500 nm) due to the increased predominance of absorption and interface roughness within p-Si layers at shorter wavelengths.

It can clearly be seen that the shape of the reflectivity peak does not closely resemble the familiar stopband shape as shown in figure 2.4. It is also expected that the reflectivity should be significantly higher for such a 20 layer stack. These

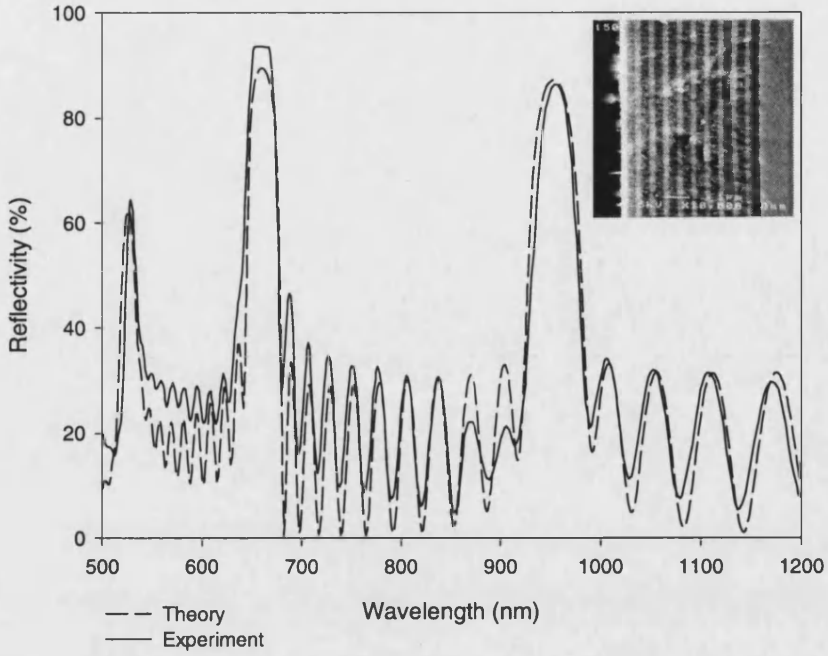

Figure 4.11: Experimental and calculated reflectivity spectra for p+ sample C150. The inset shows an SEM image of the structure [57].

disagreements are believed to be due to a significant degree of light scattering occurring at rough layer interfaces. This is a common feature of etched p- layers, as discussed in section 1.4.

Figure 4.11 shows a reflectivity spectrum of p+ sample C150 taken with the Perkin-Elmer. An SEM of the structure is shown in the inset, a larger version also being shown in figure 2.6. This sample was fabricated using the same etch currents and number of repeats as those used for C139, but slightly longer etch times were used for each layer. In comparison with figure 4.10, it can clearly be seen that the doping level of the material used to etch the sample has a significant effect on the quality of the microstructure obtained, and therefore the sample's optical characteristics.

C150 is composed of 10 high/low refractive index repeats of thicknesses 0.21 $\pm$ 0.02 μm and 0.34 $\pm$0.02 μm respectively. The two different spectra shown in figure 4.11 correspond to experimental data and the computer modelling calculations. Examining the experimental spectrum it can be seen that there are three dominant peaks centred at wavelengths of approximately 950 nm, 650 nm and 525 nm,

with reflectivities of approximately 88%, 95% and 65% respectively. It must be noted that the flat top of the 650 nm peak is an instrumental artifact, and is not the true shape of the spectra. The three peaks correspond to the 2nd, 3rd, and 4th order Bragg conditions respectively (equation 2.2). The 4th order feature is misshapen due to absorption effects becoming dominant at shorter wavelengths. Between the two bands are (N-1) resonances where N is the number of repeats in the multilayer stack.

In comparison with the reflectivity spectrum of C139 in figure 4.10, it can be seen that both the stop bands and mirror resonances are of much greater visibility. This is due to a lower degree of scattering due to interface roughness present in samples etched from p+ substrates, as discussed in section 1.4 and seen in a comparison between figures 2.6 and 2.8. Reflections from the interfaces will thus result in a significantly stronger overall reflected wave.

It can be seen that the comparison between computer modelling calculations and the experimental data is in excellent agreement. The calculated spectra was obtained using layer thickness and porosity parameters of 0.19 μm, 0.34 μm, 50%, and 71%, for the high and low refractive index layers respectively. The layer thicknesses used in the model are in good agreement with those obtained from SEM measurements, whilst the layer porosities used are within the permitted limits obtainable when etching p+ doped material (figure 1.5).

When calculating the sample spectra, changes to the layer refractive indices and spectral feature position due to errors in the layer porosities were examined. It was found that an error in the assumed porosity of each layer by $\pm 1\%$ would result in an error in the refractive index by $\pm \sim 1\%$, and hence a shift of the spectrum to shorter or longer wavelengths would occur. For example, the spectrum of multilayer mirror sample C150 exhibits a 12 nm shift to shorter wavelengths for a porosity increase of only 1%.

Increasing Layer Number in a p+ Multilayer Mirror

Figure 4.12 shows two spectra of the p+ sample C153. This structure was fabricated using the same substrate doping and etch parameters as C150, the only difference being that it is composed of 40 high/low refractive index repeats in-

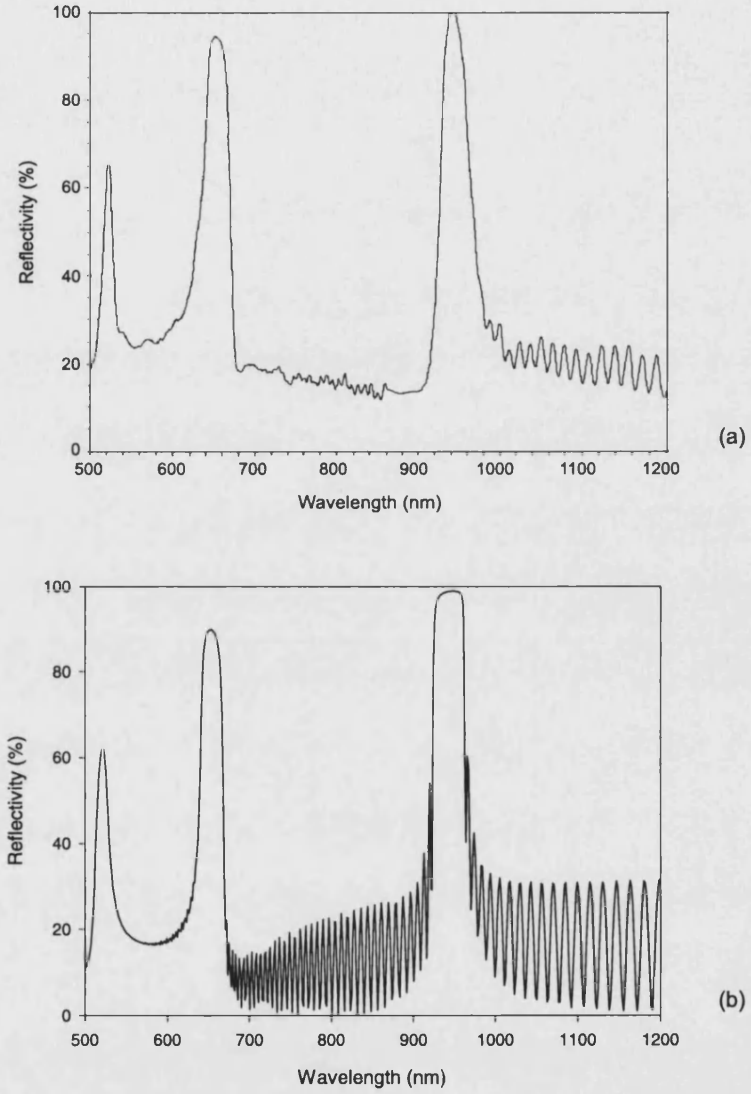

Figure 4.12: (a) Experimental reflectivity spectrum of p+ sample C153 (b) Results of computer modelling calculations for this sample.

stead of 10. Spectrum (a) shows the experimentally measured sample reflectivity taken using the Perkin-Elmer, and spectrum (b) shows the computer modelling result for the same structure.

Comparing the experimental reflectivity spectrum of this sample, (figure 4.12(a)), to that of C150, (figure 4.11), it is apparent that as the number of repeats is increased, the peak reflectivity of the second order mode increases to a value close to 100% whereas that of the 3rd order mode remains close to the 10 repeat value. A further significant feature of figure (a) is the reduction of fringe visibility when moving from long to short wavelengths. As discussed in section 4.3.2, this feature is due to instrumental effects. In comparison with sample C150 (fringe FWHM ~25 nm), the larger total thickness of this structure results in the fringe FWHM (~3 nm) falling below that clearly resolvable by the spectrophotometer (5 nm), and thus they are smeared.

The computer simulation of the experimental data was performed using the same fitting parameters as those used for C150, except that the number of repeats was increased to 40. It can be seen that the two sets of data are again in good agreement regarding peak position and relative heights. The main difference between the two spectra is the much greater fringe visibility exhibited by the calculated spectrum at long wavelengths. This occurs because instrumental smearing effects have not been taken into account when modelling.

Figure 4.13 shows an SEM image of stack C154. This structure, etched from a p+ substrate, comprises of 80 high/low refractive index layers of thicknesses $0.11 \pm 0.01\,\mu$m and $0.18 \pm 0.01\,\mu$m respectively. The structure was etched using the same parameters as C153 except that the etch times for each layer were halved. This was carried out in order to halve the thickness of the layers, allowing the first order Bragg condition to be satisfied at shorter wavelengths, and thus shifting the first order stopband to the measured wavelength region.

Figure 4.14 shows the experimental reflectivity spectrum and the computer modelling fit for this sample taken with a spectrophotometer. The experimental spectrum shows the first order stopband, of reflectivity almost 100%, centred at a wavelength of ~1000 nm. The second order band edge is seen at ~550 nm. Once again, the intermediate resonances are of much lower visibility than those of C150. To obtain a fit, layer thicknesses and porosities of 0.11μm, 0.18μm, 54%

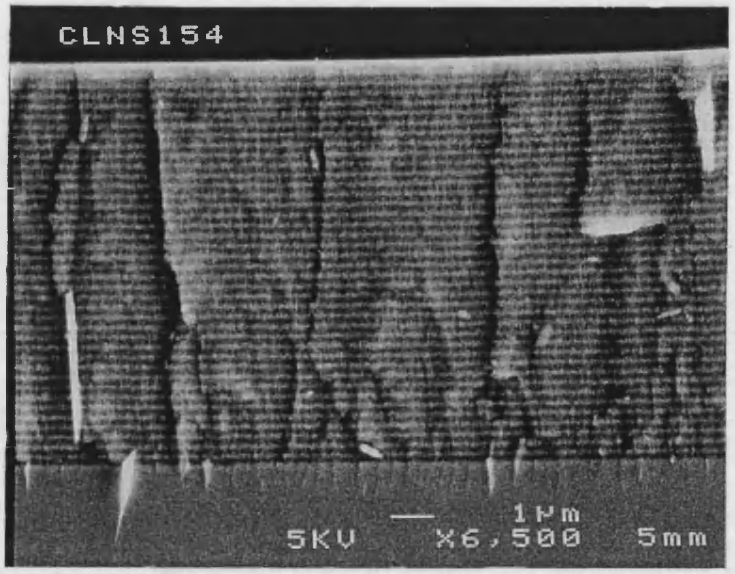

Figure 4.13: SEM image of p+ sample C154 [57].

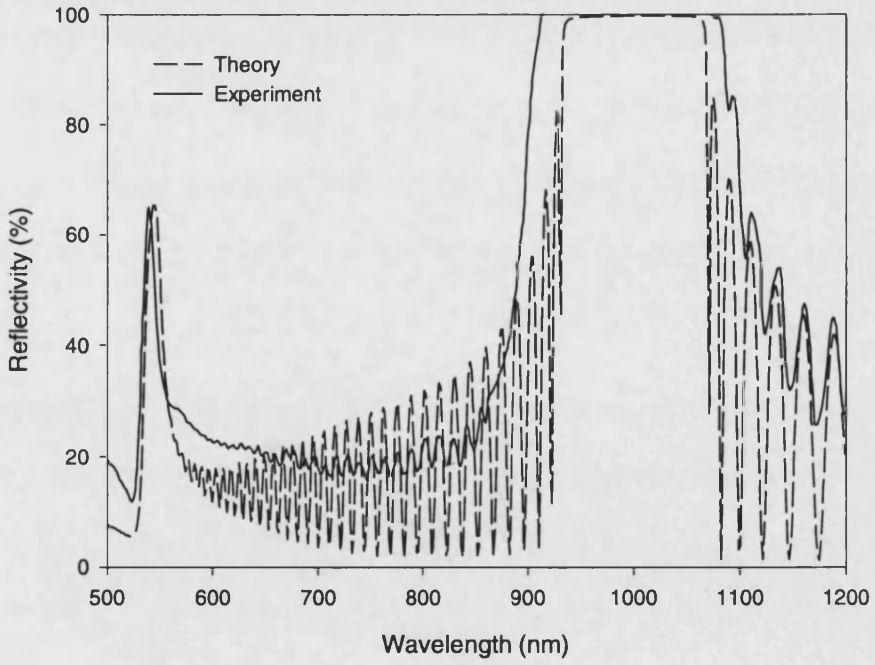

Figure 4.14: Experimental and calculated reflectivity spectra for p+ sample C154.

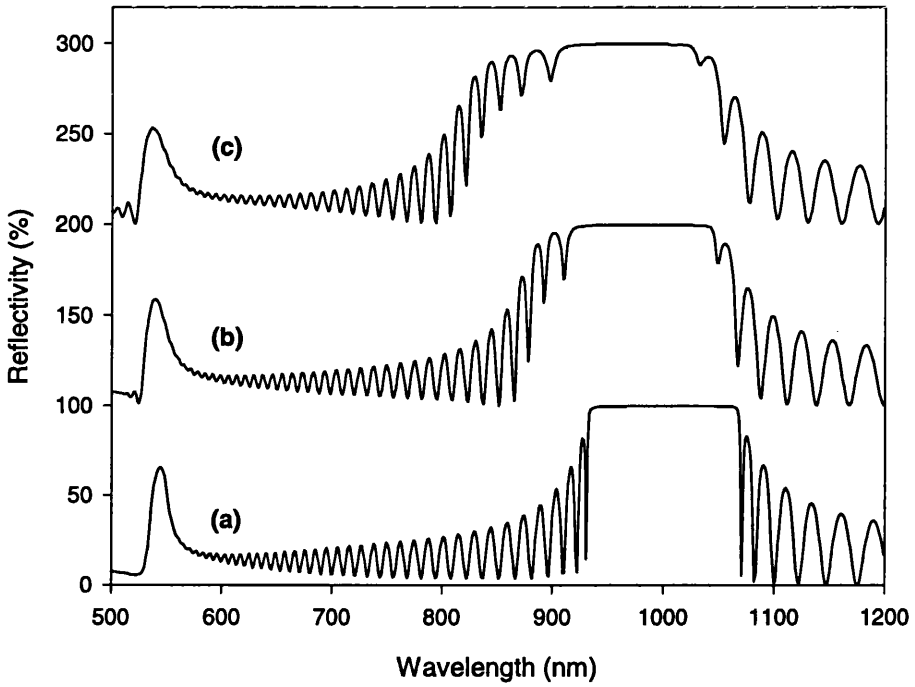

Figure 4.15: Calculated effects on the reflectivity spectra of sample C154 for increasing porosity gradients. Plots (b) and (c) have been vertically displaced by 100% and 200% respectively for clearer viewing. (a) Calculated spectra with no gradient present. (b) Calculated spectra with a 5% increase in porosity between the top and bottom layers of the stack. (c) Calculated spectra with 10% increase in porosity between top and bottom layers.

To examine the effects of porosity gradients in p-Si p+ samples, a version of the model was adapted to calculate the effects of a gradual increase in layer porosity with depth. For simplicity, the same total increase in porosity was used for both high and low index layers. However, as discussed previously, (section 2.4) the gradients found to exist within p+ samples are believed due to changes in HF concentration with depth during etching. This concentration reduction is related to the flux of HF molecules, i.e. higher current densities result in larger gradients [59]. This implies that the switching of current densities required to fabricate a multilayer stack will result in a far more complicated gradient structure than that modelled.

Figure 4.15 shows the effect on the optical spectrum of the sample due to increasing the porosity difference between the top and bottom layers by amounts of 4% and 8% (figure 4.15 (b) and (c)). It is observed that the main effect of the gradient has been to change the shape of the stopband. As the gradient is increased, the band is seen to widen and develop side modes. This occurs because the spectra is now composed of contributions from several different layer combinations each with their own Bragg condition. The stopband expands in width to the left because of the increase in structure porosity with depth results in the Bragg condition being satisfied at shorter wavelengths. Figure 4.14 shows that with no gradient present, the stopband width of the calculated spectra is too narrow. The change in stopband shape and width of the calculated spectra with a gradient present is more in agreement with that observed in experimental spectra.

Microcavities

Figure 4.16 shows an SEM image of the single microcavity sample C53. This sample, fabricated from a p+ substrate, is an asymmetric cavity structure composed of a high index defect layer sandwiched between an upper 16 layer mirror and a lower 5 layer mirror. The high index, low index, and defect layers are of thicknesses $0.08 \pm 0.02\,\mu$m, $0.14 \pm 0.01\,\mu$m and $0.19 \pm 0.01\,\mu$m, respectively.

Figure 4.17 shows the experimental reflectivity spectrum and the computer modelling fit taken at an angle of 10 degrees. In this case, the experimental spectrum was obtained using an optical spectrum analyser, and thus is a measure of reflected power only, not absolute reflectivity. For this reason, the spectrum is shown plotted in arbitrary units. It can clearly be seen that there is a dip in both the the experimental and calculated reflectivity spectra at $\sim$ 840 nm corresponding to the cavity resonance. The resonance position has been displaced to longer wavelengths due to the cavity being thicker than that required to meet the Bragg condition when $m = 1$ (see equation 2.2).

To calculate a fit to the experimental spectrum, layer thicknesses and porosities of $0.078\,\mu$m, $0.142\,\mu$m, $0.191\,\mu$m, 45%, 73% and 45% for the high index, low index and defect layers respectively were required. Once again, the layer thicknesses are in good agreement with those measured from the SEM image, and the layer

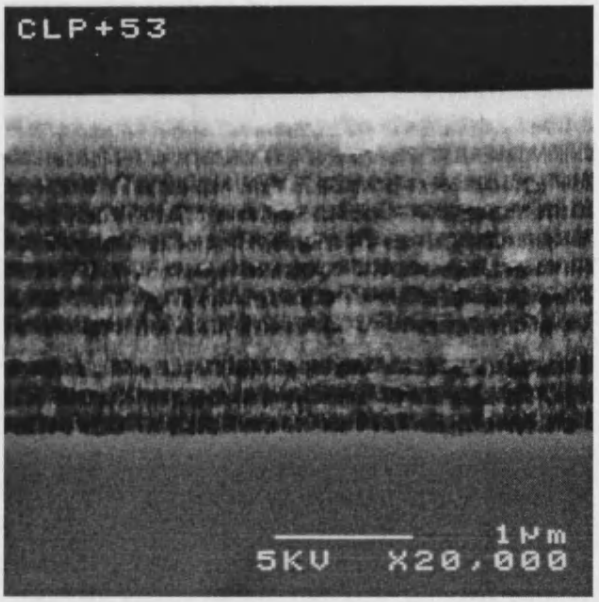

Figure 4.16: SEM image of single cavity p+ sample C53 [57].

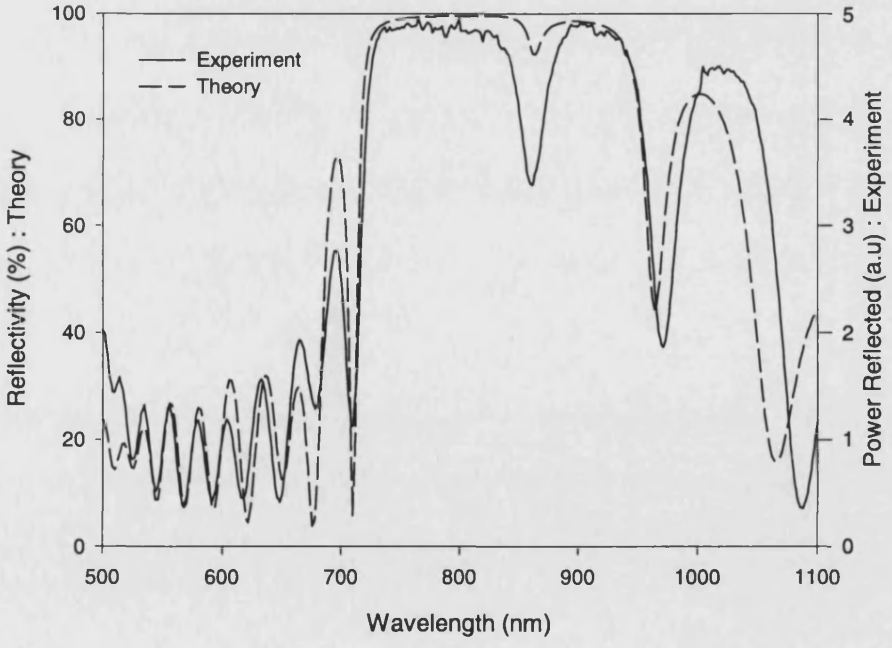

Figure 4.17: Experimental and calculated reflectivity spectra of p+ sample C53. Experimental data are shown plotted in arbitrary units.

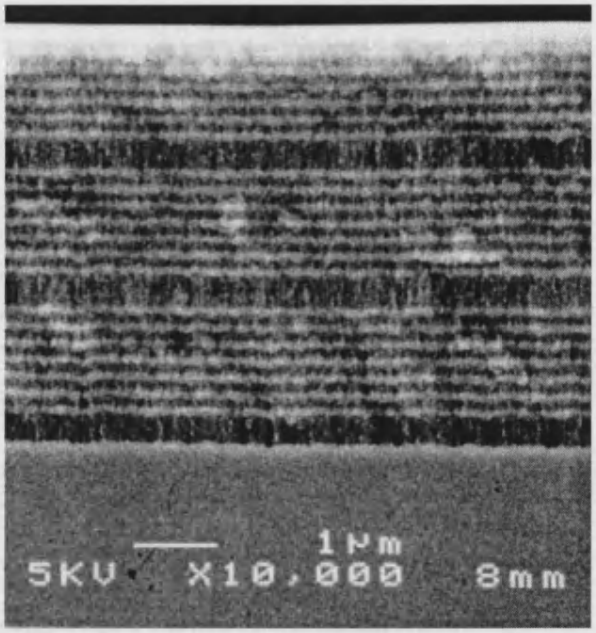

Figure 4.18: SEM image of p+ sample C61 [57].

porosities close to those obtained from previous fits.

Figure 4.18 shows an SEM image of sample C61, again etched from a p+ substrate. The sample is an example of a double cavity, i.e. there exist two defect layers sandwiched between multilayer mirrors. In addition to this, a third defect layer lies between the third mirror and the c-Si substrate. The layer thicknesses of this sample were measured to be $0.08 \pm 0.02\,\mu$m, $0.12 \pm 0.02\,\mu$m, $0.39 \pm 0.02\,\mu$m and $0.35 \pm 0.02\,\mu$m for the high and low index mirror layers, and the top two and bottom defect layers respectively.

Figure 4.19 shows the experimental and modelling reflectivity spectra at an angle of 10 degrees. Again, in this case, the reflectivity spectrum was taken using a spectrum analyser, so is only a measure of reflected power, not absolute reflectivity. Examining the experimental spectrum, the stop band is centred on a wavelength of ~800 nm. It is positioned at a lower wavelength than previous structures due to smaller layer thicknesses changing the position of the Bragg condition. The resonance dip placed at ~740 nm is observed to have a shoulder on its long wavelength edge. The modelling spectrum, which shows another good fit, exhibits a split at this point in the resonance. This splitting is a consequence of the weak coupling of light between the two cavities, and is analogous to that of coupled penduli. Two modes exist within this coupled system which are lin-

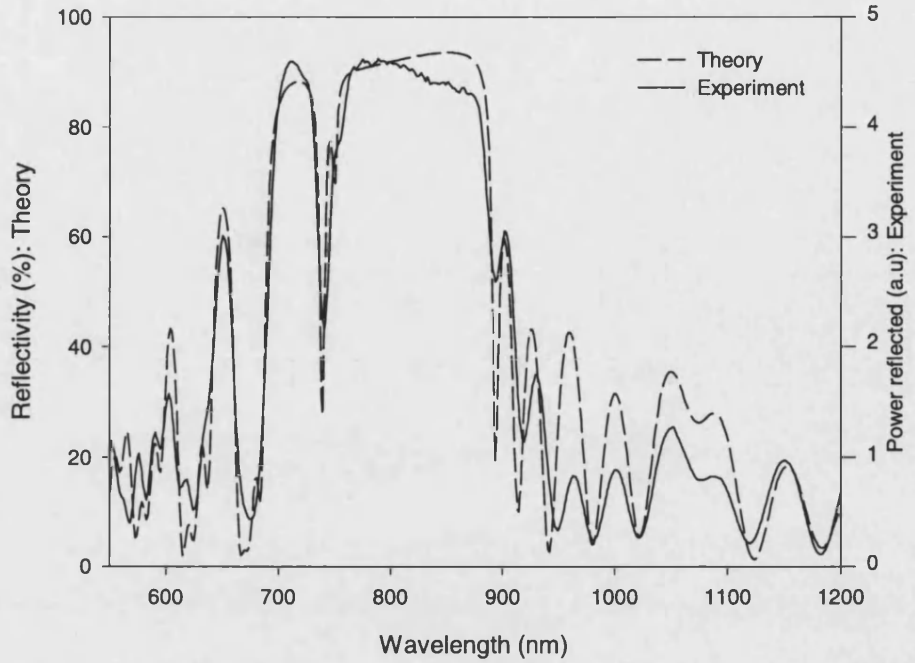

Figure 4.19: Experimental and calculated reflectivity spectra of p+ sample C61. Experimental data are shown plotted in arbitrary units.

ear combinations of the modes of the individual cavities. Therefore, the coupled mode frequencies will be modified with respect to those of a single cavity. As the coupling between the cavities strengthens the mode splitting increases, thus the small degree of splitting observed in the modelled data (figure 4.19) shows that only a very weak coupling effect is occurring. This splitting can not be seen clearly in the experimental data due to insufficient resolution. A detailed study of the optical properties of different p-Si coupled cavity systems has recently been reported by Pavesi [83].

The modelling parameters used to fit to this data are 0.08 μm, 0.11 μm, 0.39 μm, 0.35 μm, 40%, 67%, 68% and 68%, for the high index, low index, top two defect and bottom defect layers respectively. Again the layer thicknesses are in good agreement, but this time the porosities have had to be made slightly less than those used in previous fits.

4.3.4 Summary

This chapter has discussed transmission and reflectivity measurements performed on several different types of sample. These measurements were made in order to be able to determine their optical characteristics, and compare actual optical characteristics with those predicted by computer modelling.

The first sample, a multilayer mirror composed of alternating layers of amorphous silicon and silica, was found to have been fabricated to different specifications than those intended. Furthermore, experimental transmission spectra obtained from different points on the sample gave a clear indication of the existence of thickness variations in the sample layers. In this case the computer model was used to calculate fits to the experimental data and thus provide an estimate of the actual layer parameters.

The second set of samples was composed of p-Si multilayer mirrors and microcavities. Reflectivity measurements were required to characterise these samples as substrate absorption prevented transmission experiments. After obtaining the layer thicknesses of the structures from SEM images, manual adjustment of the porosity values resulted in good agreement between computer model calculations and experimental data. It has thus been shown that the modelling theory is both accurate and reliable for a wide variety of different samples fabricated from p+ material.

When examining the attributes of the experimental spectra obtained from both p- and p+ samples, it was clear that the two types of doped materials resulted in very different spectra. It was found that the p+ spectra were far more characteristic of standard multilayer structures in terms of their shapes and thus their spectra fitted well with that predicted by the model. Furthermore, the modelling of porosity gradient effects in large multilayer stacks has shown good agreement with experimental results. In contrast the spectra of the p- samples showed marked differences to that expected, e.g. weak stopbands. It is probable that these differences are mainly due to the effects of interface roughness.

It should be noted that over a period of several months whilst the experimental data were being obtained, the optical properties of the samples were found to change due to the effects of sample storage in ambient air, as discussed in section

1.5.1. The change due to oxidation of the samples lead to an observable shift in the optical spectra towards shorter wavelengths, e.g. after a period of four months after etching the reflectivity spectrum of 20 layer multilayer sample C150 was observed to have shifted by ~5 nm. Although this shift had a negligible effect on the modelling of the spectrum taken immediately after etching, if future measurements of the samples were to occur, this factor should be taken into account if using the calculated spectrum for comparison.

The next chapter discusses the use of photoluminescence measurements as a further means of characterising the p-Si samples. These measurements, and the computer modelling fits to them help determine the mechanism of light emission and propagation in p-Si microstructures.

Chapter 5

Experimental Measurements: Photoluminescence

5.1 Introduction

The previous chapter discussed the use of reflectivity measurements to determine the optical properties of different p-Si microstructures. In addition to these experiments, photoluminescence measurements were also used to characterise both p-Si multilayer mirrors and microcavities. The relative sizes and positions of the PL spectral features gave valuable information regarding the effect of different microstructures on the emission and propagation of light in each case.

Although some previous experimental PL measurements have been performed on p-Si multilayer structures, computer modelling of PL spectra has not been used as an aid to understanding the results. In this chapter, further details of the modelling of p-Si PL spectra will be discussed, and experimental spectra obtained from p-Si structures are compared with those predicted by calculations. The experimental results, obtained from a variety of structures, including a single layer, a mirror and a microcavity, clearly show the different effects that each design has on the propagation of emitted light. These effects and the conclusions drawn from comparisons between experimental and theoretical data are discussed.

Unfortunately, no comparison experiments regarding relative emission efficiencies

between different structures could be performed for two main reasons. Firstly, the samples were not fabricated on site and thus different amounts of time elapsed between fabrication and measurement. During this time the samples were stored in ambient air and underwent oxidation, thereby changing their optical properties by unpredictable amounts. Secondly, due to problems with fabrication equipment reliability, the samples are not composed of equal amounts of emitting material. This inequality in the relative amount of material in each structure meant that differences between the emission efficiency of different samples could not be considered as being due to structural effects alone.

5.2 Experimental Technique

The equipment used to obtain the PL measurements is shown schematically in figure 5.1. An argon ion laser, tuned to emit at a wavelength of 488 nm was used as a pump source to excite carriers in the material. The vertically (TE) polarised laser light was first passed through a beamsplitter so that a small portion of the beam could be monitored by a power meter to detect any fluctuations in the laser power during the course of the experiment. The second portion of the beam was then passed through a pinhole to ensure that only a small area of the sample was illuminated. This was performed in order to reduce any loss of fringe visibility due to possible lateral sample inhomogeneity.

Light emitted from the sample was collimated and passed through a polariser before being focused onto the 200 μm entrance slit of the spectrometer. This slit width gave the spectrometer a resolution of 2.8 nm. Due to the high sensitivity of the detector, the light passed through a short wavelength cut off filter (λ_{cut}=530 nm) to ensure that no laser light entered the equipment. The accumulation of the optical spectra by the detector was controlled using computer software. The obtained results were wavelength calibrated using measurements previously taken with the spectrometer and a neon discharge lamp, the wavelength accuracy of the spectrometer being $\sim$2 nm. In addition to this, the effects of system response on the results were removed through normalisation of the data with black body spectra obtained from a tungsten bulb.

Also shown in figure 5.1 is the optical arrangement used for reflectivity measure-

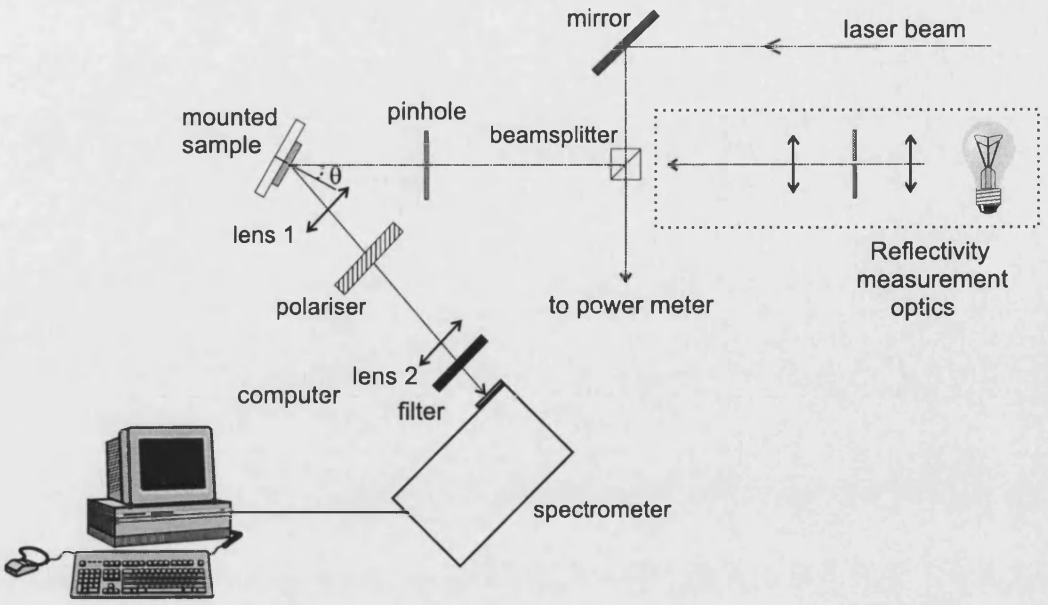

Figure 5.1: Schematic view of equipment used to obtain PL and reflected power measurements.

ments, a description of which is given in section 4.9. The integation of these optics into the PL experimental arrangement allowed both PL and reflected power measurements to be obtained without the need to move the sample or equipment. This ensured that the same area of the sample was illuminated during each experiment and thus minimised any possible errors in the results due to sample surface inhomogeneity.

5.3 Theoretical Modelling of PL Spectra

As discussed in section 3.3.5, the effects of light emission in the structure can be added to the computer model through the addition of a gain term to the complex refractive index. This term, which acts as an effective negative absorption, has a mean and standard deviation which can be adjusted to obtain a good fit to PL spectra. As with the modelling of gain in section 3.3.6, gain was added to the low index layers only. Possible improvements to this theory will be discussed in the summary at the end of this chapter.

Before a comparison between modelling calculations and experimental PL spectra could occur, one further modification to the model had to be performed.

Instead of simply plotting the total output spectrum (i.e. the sum of the reflected and transmitted waves) as shown in section 3.3.6, in this case the total output spectrum with no gain term was subtracted from the output spectrum with gain present. The difference between these two spectra gave the actual emitted spectrum.

that the shape of the obtained emission curves did not change until a certain threshold value of gain was reached. This value corresponded to the point where the value of gain in the model exceeded that of absorption, i.e. net gain existed in the structure. Whilst this theory matches well with that known of gain in light emitting materials, i.e. laser emission will occur when net gain exceeds net loss, it meant that the model could not be used to obtain a quantitative feel for the amount of gain in each structure. It was found that the gain parameter could be increased by several orders of magnitude below the threshold point, and still fit the shape of the experimental data. For this reason, the amount of gain added to the structure to achieve the spectral shape is not quoted with the other fitting parameters used.

5.4 Results and Discussion.

5.4.1 Emission from Single and Multilayer p- Samples.

Sample 82Q

Figure 5.2 shows the experimental and calculated PL spectra of single layer p-sample 82Q, taken at an angle of 15 degrees to the normal. The sample, shown schematically in the inset, is of width 4.5 μm and porosity 81%, both values being calculated through gravimetric measurements. The experimental spectrum is seen to exhibit a peak at $\sim 715 \pm 5$ nm and has a FWHM of $\sim 160 \pm 10$ nm. The modelled PL spectrum was calculated using the Fabry-Pérot model described in section 3.3.3. Given the porosity and thickness of the layer, the modelling calculations were performed by simply varying the mean and standard deviation of the Gaussian distribution governing the position and intensity of the gain. To obtain a good match to the experimental data, values of 690 nm and 75 nm were

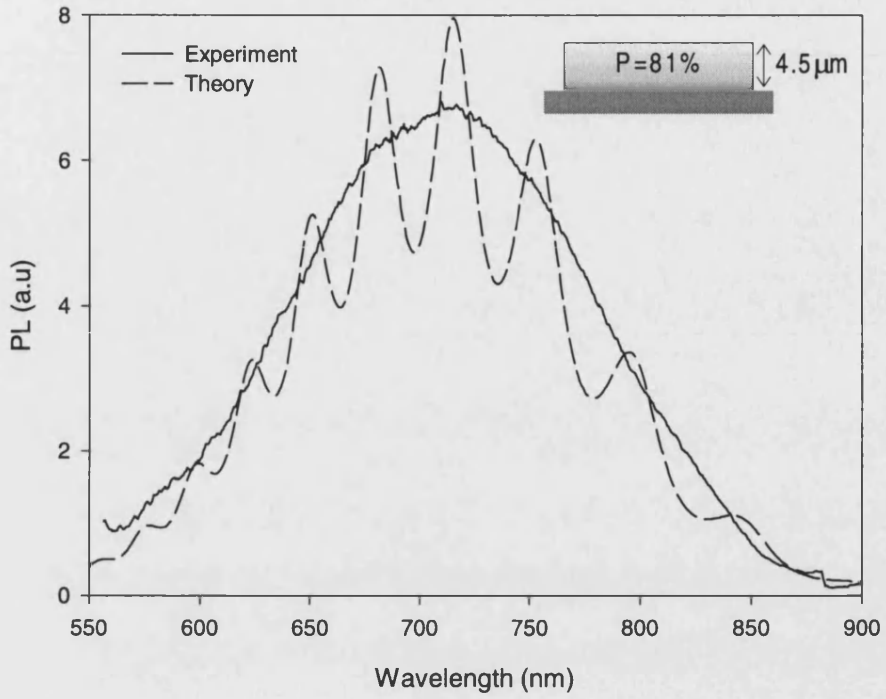

Figure 5.2: PL spectrum of single layer p- sample 82Q, and a fit to the experimental data. A schematic view of the sample structure is shown in the inset.

used for the mean and deviation respectively.

It is clear that the calculated spectrum shows high visibility Fabry-Pérot modes which are not observed in the experimental results. This lack of visible modes is probably due to diffuse reflections off a rough layer/substrate interface. The absence of any dominant propagation modes in the structure has thus resulted in the light being emitted over a broad distribution of wavelengths.

This spectrum is shown as an example to illustrate the difficulty encountered when modelling structures fabricated from p- material. Even though the structure was composed of a single layer of known thickness and porosity, it is clear that the shape of the calculated spectrum does not agree with that experimentally obtained. It is probable that the predominant effect responsible for this disagreement between results is that of light scattering due to interface roughness (section 1.4). The degree of roughness within p- samples is believed to be dependent on the initial surface state of the wafer [13], and thus due to its random nature could not be accounted for without the need for detailed modelling.

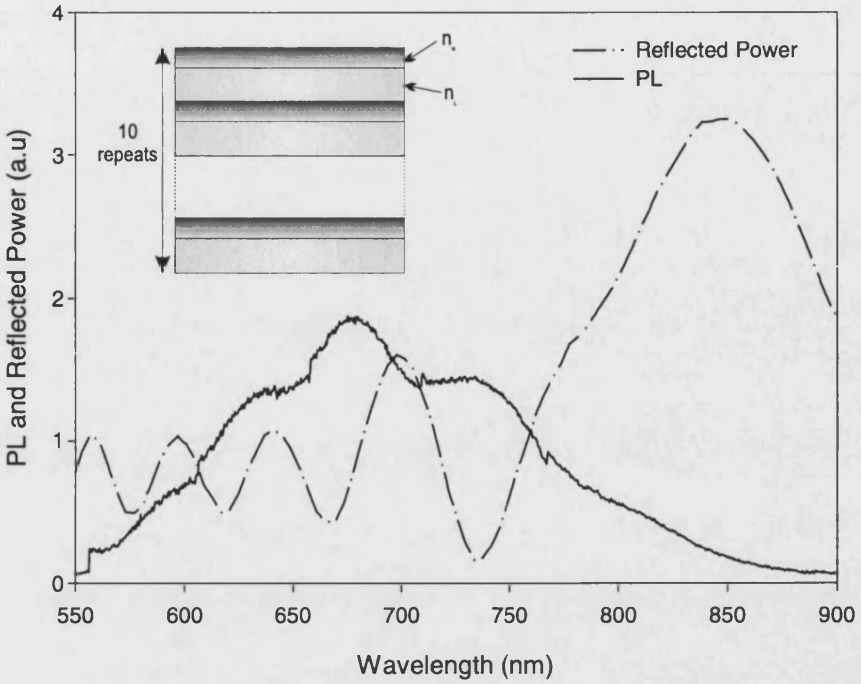

Figure 5.3: PL and reflected power spectra of p- multilayer mirror sample C147. The inset shows a schematic view of the sample structure.

Sample C147

Figure 5.3 shows the PL and reflectivity spectra of p- multilayer sample C147 an angle of 15 degrees. The reflectivity spectrum, taken at the same time as the PL spectrum, is a measure of reflected power only due to experimental difficulties (section 4.3.2). However, an earlier reflectivity measurement taken by a specrophotometer immediately after fabrication showed the peak reflectivity value to be ~75% at ~850 nm. A schematic view of the structure is shown in the inset. This sample was fabricated from a wafer of the same doping level, and has the same number of layers as p- sample C139, previously described in section 4.3.3. The only difference between these samples is that both high and low index layers in C147 have been etched for slightly longer thereby increasing the layer thicknesses to approximately 0.08 $\pm$ 0.02 μm and 0.12 $\pm$ 0.04 μm respectively.

Examining the reflectivity spectrum of figure 5.3, in comparison with that of C139 (figure 4.10) it can be seen that the weak stopband is now positioned at a longer wavelength of $\sim$ 850 nm which is consistent with the sample being

composed of layers of greater thicknesses. In comparison with the PL spectrum of sample 82Q similarities are observed in the overall spectral shape and emission bandwidth. However, whereas the spectrum of 82Q exhibits only a single peak, that of C147 exhibits 3 poorly defined peaks over the broad emission background. The central peak is observed to be of slightly higher intensity than the shoulder peaks but it does not dominate the spectrum. The maximum in the spectrum can be seen to approximately coincide with the dips in the reflectivity spectrum between $\sim 630 - 730$ nm, thus indicating that the light is being emitted into the transmission modes of the structure. Emission occurs preferably into these modes as they are positioned in the region where the majority of p-Si emission occurs for similar p- doped material as shown in figure 5.2.

The results of figure 5.3 have been presented in order to illustrate the difficulty in using p- doped material to obtain a structure capable of narrow bandwidth emission. The control of both the position and bandwidth of the light emission is of great importance when designing light emitting structures.

Although structures fabricated from p- material have a naturally higher emission efficiency than that of the p+ based structures [14], the high degree of interface roughness (section 1.4) present within p- multilayers means that it is much more difficult to fabricate samples with specific optical characteristics. It is thus clear that if the latter material is to be considered for device applications, sufficient work has to be done to control the formation of rough interfaces and thus improve the quality of the optical output.

5.4.2 Emission from p+ Samples.

Sample C154

Figure 5.4 displays the experimental PL and reflected power spectra of p+ sample C154 between the wavelengths of 650-800 nm. The spectra were taken at an angle of 15 degrees to the normal. The inset picture shows the absolute reflectivity spectrum for the sample taken by a spectrophotometer at an earlier date (figure 4.14). This sample, described in detail in section 4.3.3, is composed of 80 layers of alternating high/low refractive index material. The large number of mirror

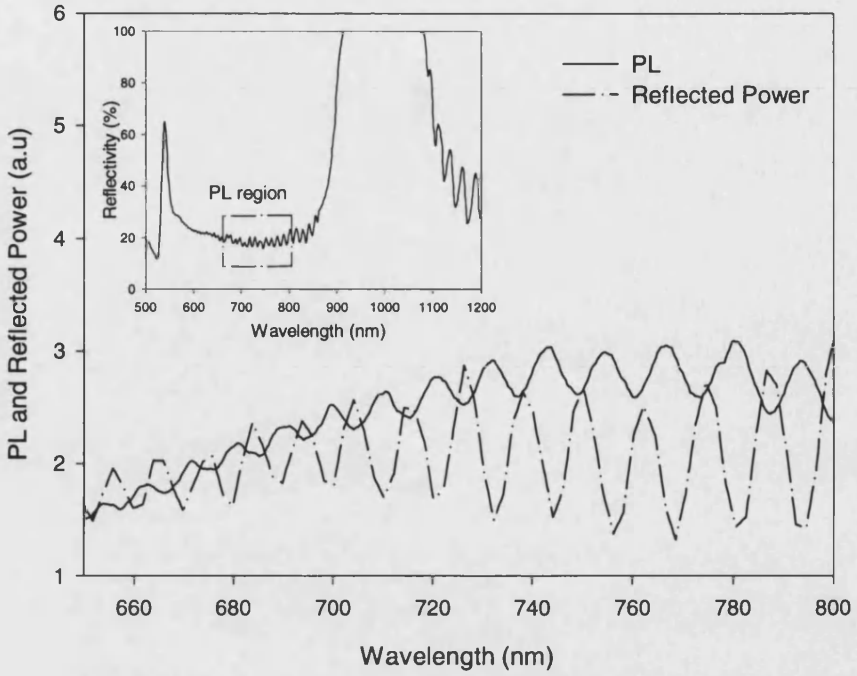

Figure 5.4: A portion of the PL and reflectivity spectra of p+ multilayer mirror sample C154. The complete absolute reflectivity spectrum of the structure is shown in the inset.

repeats N results in a total of $N-1$ structural resonances occurring between the first and second order stopbands.

As with sample C147 described above, the peaks in the PL spectrum are seen to coincide with the dips in the reflectivity spectrum thus showing that the light is exiting the sample via the structural transmission modes. Comparisons with the experimental PL spectrum of C147 shown in figure 5.3 show that in this case the stack resonances are clearly seen in both sets of data thus confirming the higher interface quality present in the p+ sample.

Figure 5.5 displays the experimental and calculated PL of this sample. It can be seen that the two curves are in good agreement between about 550 and 830 nm. Above $\sim$ 830 nm the calculated curve is consistently higher than the experimental. This is due to the photocathode within the detector reaching the high wavelength limit of its spectral response and thus experiencing a reduction in sensitivity.

In this figure the entire PL spectrum is shown, and similar to the results of pre-

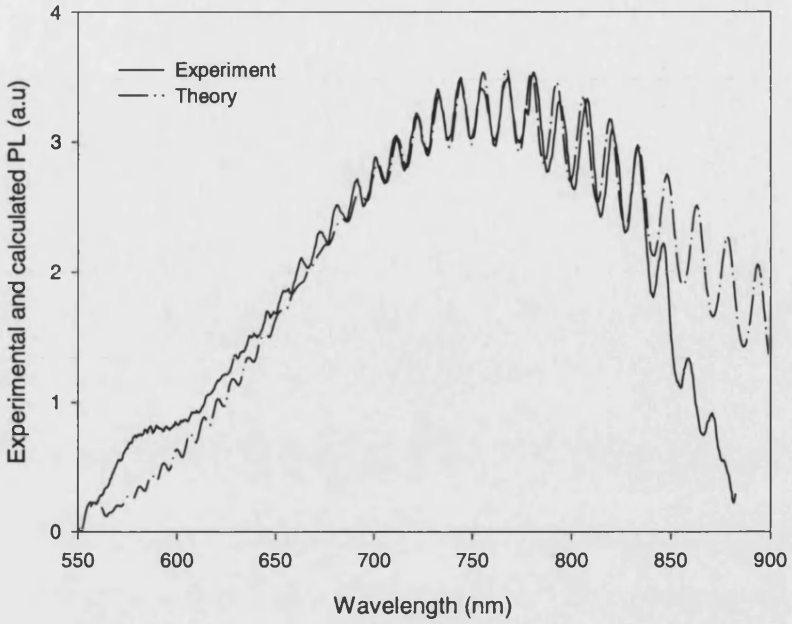

Figure 5.5: Experimental and calculated PL spectra of multilayer mirror sample C154.

vious plots, the spectrum exhibits resonance peaks distributed across a broad emission background. The experimental spectrum shows a peak of the background distribution at $\sim 780 \pm 5$ nm and has a FWHM of $\sim 180 \pm 10$ nm. The modelling calculations were performed using the same layer porosity and thickness values as those used to fit the reflectivity data of section 4.3.3. Values of 710 nm and 120 nm were used to represent the gain mean and standard deviation of the Gaussian distribution respectively.

In comparison with the mean and deviation used to calculate the spectra of sample 82Q (690 nm and 75 nm respectively), the mean of the calculated spectrum for C154 lies at a higher wavelength and the standard deviation is larger. The position of the p- layer mean at shorter wavelengths, and the smaller standard deviation it displays, are both consistent with previously obtained results which attribute these observations as due to p- material being composed of smaller crystallites of more uniform size [1].

Examining the two PL spectra of figure 5.5 it can be observed that although there exist many clear transmission modes into which emission can occur, it is again apparent that no one resonance is seen to dominate over the others. Studying the reflectivity spectrum of this sample shown in the inset of figure 5.4, or enlarged in

figure 4.14, it is seen that the resonances into which the emission is occurring are situated $\sim$ 200 nm from the short wavelength edge of the first order stopband. In this region approximately midway between stopbands, the emission is distributed evenly amongst the modes.

Given the nature of the observed emission from this sample, it is clear that this structure is also unsuitable for any device requirements. To obtain emission into a single mode and thus obtain narrower bandwidth and increased emission efficiency, it is necessary to position a dominant transmission mode over the region of peak material emission. The effects of achieving this are now discussed.

Sample C53

Figure 5.6 shows the PL and reflectivity spectrum of microcavity sample C53. This sample, described in further detail in section 4.3.3 is a microcavity sample composed of a high index cavity layer sandwiched between an upper 16 layer mirror and lower 5 layer mirror. In contrast to the PL spectra of sample C154 which exhibits emission equally distributed over a broad wavelength range, the emission spectrum of C53 exhibits a single strong mode. Both reflectivity and PL spectra for this sample were taken at a 10 degree angle to the normal. The structural details of this sample are described fully in section 4.3.3, but an SEM image of the sample is shown in the inset of figure 5.6.

Examination of the PL spectrum shows emission occurring into the first transmission mode positioned on the short wavelength edge of the first order stopband. Although this is a microcavity structure, the fact that emission occurs into this mode instead of the cavity resonance is not surprising for two reasons. Firstly, it is observed that the mirror transmission mode is situated at the peak of the p-Si material emission region whereas the cavity resonance is positioned at longer wavelengths, $\sim$150 nm away from the main mode. Secondly, the distribution of the electromagnetic wave intensity within the structure at the respective mode wavelengths will affect the amount of emission into them. As discussed previously (section 3.2), on the short wavelength edge of the stopband the electromagnetic wave intensity is found predominantly in the low index layers of a multilayered structure. At the cavity resonance wavelength the field will be in the defect layer, which in this case is a high index and highly absorbing layer. It can therefore be

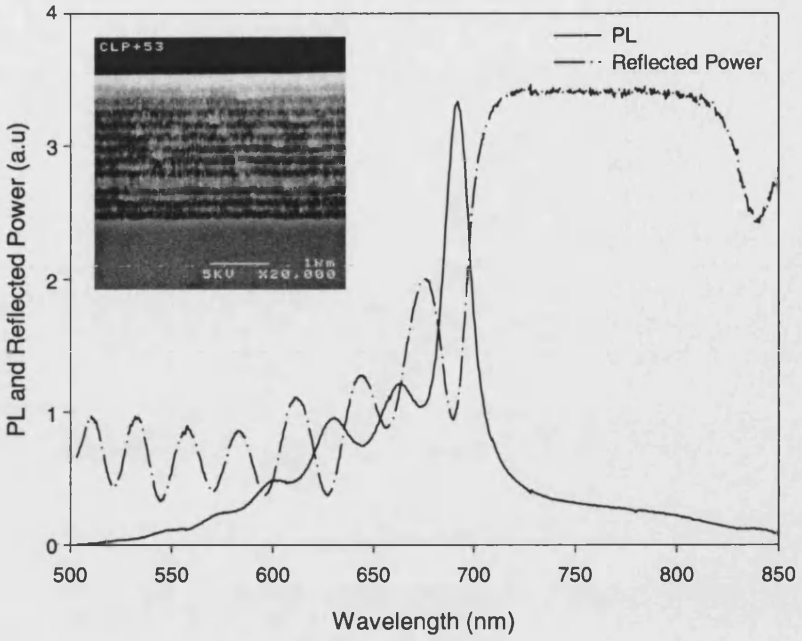

Figure 5.6: PL and reflected power spectra of single cavity sample C53. An SEM image of the structure is shown in the inset [57].

seen that more emission will be excited and emitted from the low index layers at the wavelength of the first transmission mode, than will occur at the resonance wavelength.

From figure 5.6 the peak of the main mode occurs at $\sim 690 \pm 1$ nm and the mode has a FWHM of $\sim 13 \pm 1$ nm. In comparison with the spectrum of sample 82Q the FWHM of this mode is an order of magnitude smaller. The reason for this is the effect that the two different structures have on the width and distribution of their respective transmission modes. Due to the nature of light propagation in each structure (see chapter 2), multilayered structures exhibit much narrower modes than those of a single layer. The manipulation of the structural design to create narrower mode widths is one feature of multilayered structures which can be exploited to design optimised structures.

In addition to the emission into the dominant mode, some emission is also seen to occur into the weaker side modes on the short wavelength side of the main peak. The degree of background emission is seen to be much less than that observed in the spectra of sample C154, (figure 5.5) due to the dominance of the main mode,

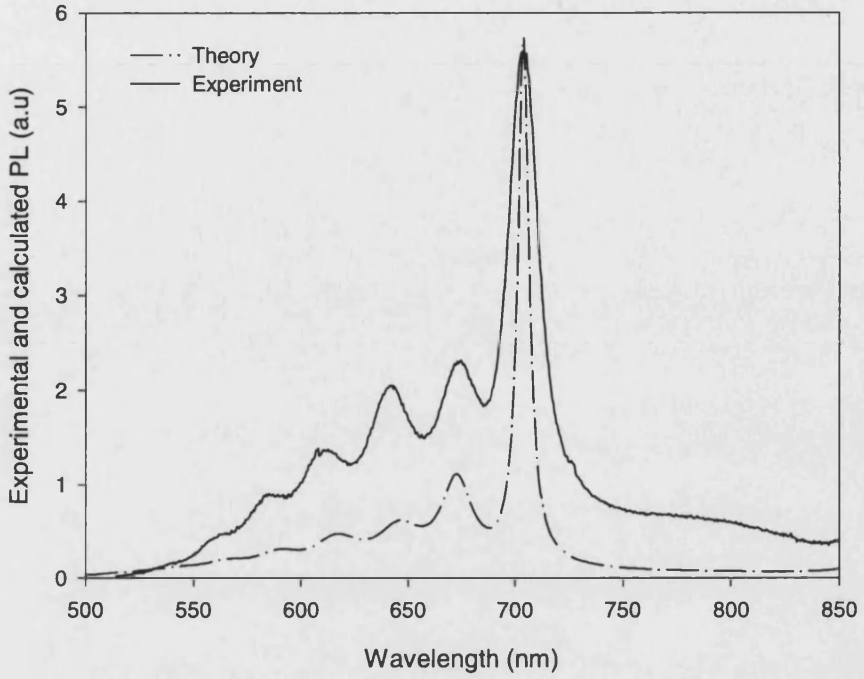

Figure 5.7: Comparison between experimental PL and modelling calculations for single cavity sample C53.

but it is still apparent that the material emission is still occurring over a broad wavelength range.

Figure 5.7 shows the comparison between the experimental and calculated PL spectra for this sample. Values of 730 nm and 130 nm were used for the mean and standard deviation of the calculation respectively. It is clear that although the two spectral shapes are very similar, the experimental data exhibits a much larger degree of background emission. Such high background emission in a microcavity spectrum has also been noted by Lérondel [84]. He interpreted it as being weak luminescence from the Bragg mirrors adding to that emitted from the defect layer, i.e. the entire structure is contributing to the total luminescence.

The discrepancy between the results shown in figure 5.7 can be interpreted in a similar fashion. Examining the layer distribution in sample C53, it can be seen that its cavity layer is composed of high index material. However, when modelling this structure, the computer calculations only account for emission from low index layers. Therefore, a large amount of potential emitting material is being ignored

by the model. The high level of background emission in the experimental PL spectrum which the model does not match (figure 5.7) thus indicates that the high index layers may also contribute to the overall emission spectrum.

Examining the emission from this sample in terms of photonic band gap theory, it is clear that the design of the structure does not allow it to emit light as efficiently as it could. In this sample emission occurs into modes on the short wavelength edge of the stopband, where, as previously discussed, the intensity of the electromagnetic wave is strongest in the low index layers (see section 3.2). Given the high proportion of high index material, i.e. material of higher absorption, in the stack it is apparent that this is an inefficient design.

An obvious means of improving the design of C53 would be to increase the amount of low index material in the structure, e.g. make the defect layer low index. Increasing the amount of this less absorptive material in the structure will thereby increase the light output. Emission from a structure fabricated from predominantly low index material is discussed next.

Sample C61

Figure 5.8 displays a combined plot showing the reflected power and PL spectra for double cavity sample C61, taken at a 10 degree angle. The inset of the figure shows an SEM image of the structure. The PL results show similarities with those of sample C53 in that a large portion of the emission is exiting the structure via a single dominant mode. However, in this case, the adjacent side mode on its short wavelength side is more prominent than that seen in the previous case. These two modes are the cavity resonance mode, positioned at a wavelength of $\sim 739 \pm 1$ nm with a FWHM of $\sim 12 \pm 1$ nm, and the first transmission mode on the short wavelength edge of the stopband at ~ 670 nm. For this sample, the cavity mode is situated towards the short wavelength edge of the stopband and is thus much closer to both the first transmission mode, and the peak of the p-Si material emission. The closer proximity of the modes therefore results in the emitted light being more evenly distributed between them. It should be noted that the sharp dip on the left edge of the cavity PL peak is an experimental artefact, whereas the pronounced shoulder on the right edge indicates a splitting of the cavity mode due to double cavity effects [83].

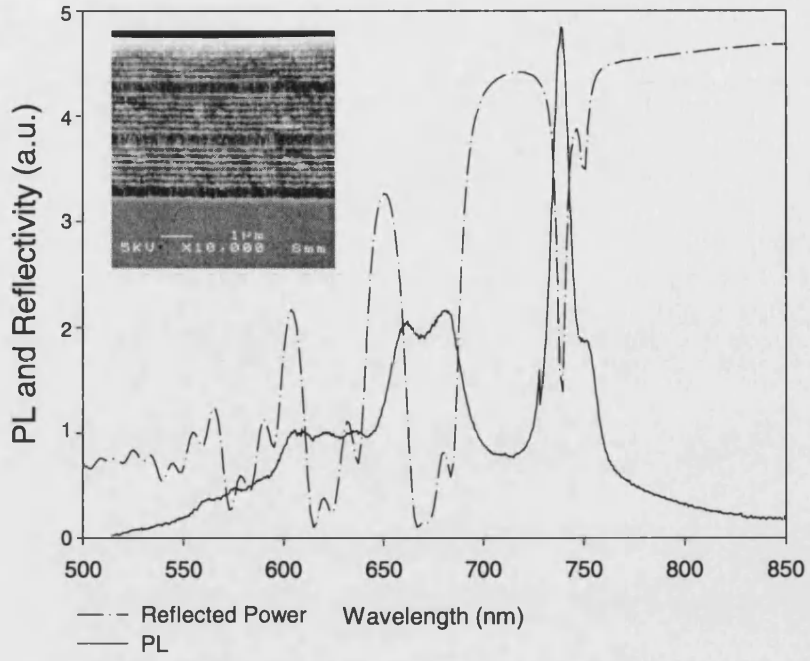

Figure 5.8: PL and reflected power spectra of double cavity sample C61. An SEM image of the sample is shown in the inset [57].

Figure 5.9 shows the comparison between experimental data and modelling calculations of the PL. As in the previous case it is observed that the spectral shapes are in good agreement, but with reference to figure 5.7, there is once again a background level between the modes which the calculated spectra does not match. The mismatch seen in figure 5.9 is far less significant than that observed in C53 because this sample is fabricated from predominately low index material (~67% of total thickness), and thus when modelling emission from the structure, the majority material is being taken into account. Furthermore, modelling calculations have shown the high index layers to be of lesser porosity (40%) than those in C53 (45%). It is possible that the higher proportion of material in these layers increases the amount of absorption in them, thereby significantly reducing any contribution they may make to the total luminescence.

As with previous calculations, to obtain the fit, the same porosity and layer thickness values used to calculate the reflectivity spectrum were entered into the program. Values used for the mean and standard deviation of the Gaussian distribution in this case were 730 nm and 100 nm respectively.

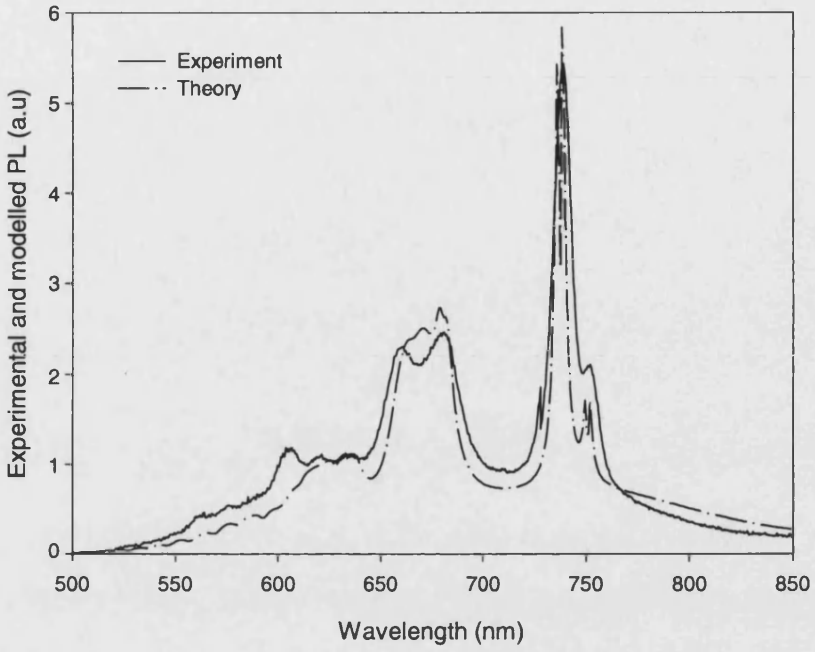

Figure 5.9: Comparison between experimental PL and modelling calculations for double cavity sample C61.

Examination of the field distribution in this sample shows that at the cavity resonance, the majority of the field intensity is situated in the main defect layer. In this case, the defect is fabricated from the less absorptive low index material and thus the layer composition of the structure cannot be significantly improved upon. The main improvement which could be made to this sample design in order to increase the light output would be to move the transmission modes further apart. Movement of the stopband to shorter wavelengths by decreasing the mirror layer thicknesses would result in the positioning of the cavity resonance mode coincident with the peak of the material PL. In addition, the cavity layer thickness could be adjusted in order to move the resonance dip away from the first mirror transmission mode and further into the stopband. This would then cause the emission to be channelled preferentially into the cavity mode.

5.5 Summary and Conclusions

In this chapter PL results taken from several different types of p-Si structure have been displayed and discussed. Excluding the calculated spectrum of the single layer p- sample, the modelled spectra were found to be in good agreement with the experimental data.

Examining the experimental results obtained from the p- samples, it is observed that they show significantly smaller fringe visibility in comparison with those of the p+ samples. As discussed previously in section 1.4, layered p- structures exhibit a high degree of interface roughness. The scattering of light caused by this roughness will affect the optical properties of the structure, i.e. reduce the reflectivity and lower the fringe visibility. The random nature of this occurrence means that it could not be accounted for in the modelling calculations and thus discrepancies between experimental and modelled results will be observed.

The main difference found between the experimental and calculated results for the p+ samples was that the modelled spectra indicated lower levels of background emission than that measured. This mismatch was far more evident in the p+ structure containing a large proportion of high index material and is interpreted as being due to the exclusion of emission from these layers when modelling the spectra. This problem could be overcome, and the modelling made more accurate, by the inclusion of a second Gaussian distribution within the computer program to model emission from the high index layers. A second distribution would be necessary as the high index layers will have a different mean and standard deviation value to that representing the low index layers. Furthermore, it should be taken into account that due to reduced confinement, it is probable that the quantum efficiency of emission from these layers will be lower than that from the low index layers.

The structures examined showed a wide variety of different PL spectra. Suggestions on how to improve these optical characteristics in order to increase the efficiency of light emission were presented. The results show the necessity for careful device design in order to place the dominant transmission mode of the structure both in the correct position and as far from adjacent modes as possible. This will result in the p-Si emission being channelled preferentially into this mode. The good agreement shown between modelling calculations and ex-

perimental data confirms that a good level of understanding has been obtained regarding the propagation of light in p-Si multilayered structures. The model can therefore be reliably used as an aid to designing future samples.

Chapter 6

Summary and Conclusions

Until the beginning of this decade it had not been possible to obtain efficient light emission from silicon, and thus it was rejected for use as an optoelectronic material. The demonstration in 1990 that p-Si can emit brightly in the visible spectrum [1] triggered worldwide interest aimed at fully integrating p-Si light emitting devices with existing silicon microelectronic technology. Initially, this research effort was concentrated in two main areas, firstly the understanding of the light emission process itself, and secondly, the development of p-Si light emitting structures which could operate with comparable efficiencies to existing semiconductor devices.

One of the main features of the spontaneous emission spectrum obtained from a single layer of p-Si is its broad width. This characteristic is undesirable in optical components where a narrow output bandwidth is required. A key point in the design of many p-Si optical devices is the modification of this spontaneous emission through the use of microstructuring. The effect of introducing structural periodicity is to create photonic band gaps, i.e. bands of wavelengths where light propagation is forbidden. The placement of a defect layer within the periodic multilayer structure, e.g to form a microcavity, will introduce a defect mode into the stopband, which corresponds to the cavity resonance mode. Due to the confinement effects of the cavity structure, the emitted mode is greatly narrowed and enhanced in comparison with the emission mode of a single layer.

P-Si microcavities differ from those commonly used within other structures, e.g

VCSELs, for two main reasons. Firstly, instead of emission being confined to the active central active only, it is possible for the entire structure to be emitting. Secondly, the light emission spectrum of the p-Si is in general wider than the stopband of the structure. Interesting effects will thus be observed in the optical spectra of cavity structures as light is coupled into both the cavity mode and mirror resonance modes either side of the stopband.

The purpose of this work has been to examine the process of light emission and propagation within many different one dimensional p-Si microstructures. Samples investigated include single layers, multilayer mirrors, and single and double microcavities. To achieve this aim, both experimental and theoretical techniques were used in to examine these issues from two different perspectives and thus gain a more complete picture. These methods included computer modelling of the optical properties of p-Si structures, and measurements of the reflectivity and photoluminescence spectra of fabricated samples.

Computer modelling was used for two purposes. Firstly, to aid in the design of different p-Si microstructures by predicting the optical characteristics of each. The experimentally obtained spectra from fabricated samples were then used in comparison with those calculated in order to assess the accuracy and validity of the assumptions made in the modelling process. Secondly, the model was used the compare the relative efficiencies of a variety of more complex structures. This method has enabled much valuable information regarding light propagation in various p-Si structures to be obtained quickly and without the need for fabrication.

The basic framework of the computer model uses either the Fabry-Pérot equations or a transfer matrix method to calculate the amplitude of an electromagnetic wave as it passes though a single layer or multilayer structure respectively. These calculations are used to predict the reflectivity, transmissivity and photoluminescence spectra of various p-Si structures. The computer code has been adapted to include features necessary to model porous materials in general and p-Si specifically. These features include accounting for dispersion effects in the material by calculating the real part of the refractive index using the Herzberger equation. Use of a simple mixing equation, the Looyenga formula, to calculate the effective dielectric function of a layer formed from a mix of two different materials. The effect of losses in the material due to absorption by the silicon are included in

the calculations as part of a complex refractive index. Furthermore, emission can also be added to the model through a negative absorption term in the complex refractive index.

Modelling of a set of four different p-Si structures, including a single layer, two different multilayer mirrors and a microcavity was performed. The two mirrors were designed to exhibit a particular feature of photonic band gap theory. This effect causes the electromagnetic field intensity of the mode to distribute itself within the low or high index layers of the structure depending on whether the wavelength of the propagation mode is positioned on the long or short wavelength edge of the reflectivity stopband respectively. Thus one mirror was designed so that the field stacked in the low index layers which should exhibit greater emission efficiency, and the other designed so that the field was in the high index highly absorbing layers. Results revealed that the first mirror can exhibit comparable efficiency to that of a microcavity, whilst the second mirror and single layer were much less efficient. It can therefore be concluded that the use of photonic band gap effects to manipulate the propagation of light within simple multilayer mirrors is a method which should be given much consideration when examining optimised device designs.

In conjuction with the computer modelling, experimental measurements were carried out in order to examine the reflectivity and photoluminescence of all fabricated p-Si samples. These samples comprised a wide variety of different structures including single layer, multilayer mirror, single and double microcavities. For almost all reflectivity and PL spectra examined, comparisons between experimental and calculated results were in very good agreement.

It was found that there existed two main instances where a good match was not obtained. The first was apparent when modelling p-Si structures fabricated from p- material. The computer model was found to produce spectra with highly visible fringes which did not agree with the smoother curves of the experimental data. These fringes, caused by the interference of multiply reflected waves within the structure, are not apparent in p- structures because of the significant interface roughness inherent in them. This results in the scattering of light from the interfaces and a subsequent reduction in reflectivity and loss of fringe visibility. This process can not be modelled due to its unpredictable nature. The second instance where disagreement between the data was observed, involved the exis-

tence of porosity gradients within the structure. These gradients, found in large p+ structures cause a widening and fragmentation of the stopband to occur. A modification to the computer model allowed the modelling of a large multilayer mirror containing a simple gradient. These results were in good agreement with those observed experimentally.

When examining the optical spectra of the samples, it was clear that the emission was propagating in the structural transmission modes. The placement of these modes with respect to the wavelengths of maximum material emission was observed to have significant effects on the shape of the spectral features. Furthermore, the proximity of the modes with respect to each other also had a large effect on the obtained lineshape. In larger mirror structures it was clear that the emission was distributing itself between many adjacent modes, thus reducing the light output from any one. This feature was also observed in the modelling data. Examining the luminescence spectra of the microcavity samples the spacing of the modes was also found to be of importance. If the cavity mode was positioned too close to the stopband edge, the emission would distribute itself amongst it, and its adjacent mirror resonance modes. It can thus be concluded that careful design and fabrication of p-Si microstructures is required to ensure the correct positioning of the structural modes with respect to the emission distribution of the material.

In conclusion, comparisons between modelling calculations and experimental measurements of the reflectivity and photoluminescence spectra of many different p-Si microstructures have exhibited very good agreement. The instances where mismatches between the two data have occurred have been explained, and in the case of porosity gradients, have also be modelled. These results show that an effective model can be created based on relatively simple assumptions. Furthermore, this model can be adapted to suit other porous semiconductor materials if required.

The results of this work have revealed two main issues which should be considered for further examination and development. The first issue concerns the comparison of the relative emission efficiency of different p-Si structures containing emitting material of equal total thickness and porosity. In order to achieve this degree of equality between samples a high degree of control is required over the etching process. One method of achieving this is through the use of optical methods to perform *in situ* measurements of the layer thickness and refractive index during

sample growth.

The second issue concerns the further development of the computer model in order to increase the accuracy of data fits. Areas which could be considered include the addition of interface roughness to allow the modelling of p- structures or samples comprised of both p- and p+ material, and to further examine the effects of porosity gradients on optical spectra. Furthermore, it would be important to consider the use of a fitting algorithm to aid in the data comparison process if the level of modelling detail, and thus number of parameters, were to increase.

The large variation of samples investigated in this work has provided much information regarding structural effects on the emission and propagation of light within them. The results obtained from experimental and theoretical data display an interplay of a wide variety of effects dependent upon the composition of the microstructures. It is hoped that the information obtained will assist in the further development of p-Si device designs.

References

[1] L.T. Canham, *Appl. Phys. Lett.*, **57**, 1046, (1990).

[2] A. Uhlir, *Bell. Syst. Tech. J.*, **35**, 333, (1956).

[3] K. Imai, *Solid State Electron.*, **24**, 159, (1981).

[4] R. Eisberg, R. Resnick, *Quantum Physics of Atoms, Molecules, Solids, Nuclei, and Particles*, 2nd ed, John Wiley and Sons, (1985).

[5] S.M. Sze, *Physics of Semiconductor Devices*, Wiley Interscience, 13, (1981).

[6] P.M. Fauchet, L. Tsybeskov, C. Peng, S.P. Duttagupta, J. von Behren, Y. Kostoulas, J.M.V. Vandyshev, K.D. Hirschman, *IEEE. J. Sel. Top. in Quan. Elec*, **1**, 1126, (1995).

[7] M. Stutzmann, J. Weber, M.S. Brandt, H.D. Fuchs, M. Rosenbauer, P. Deak, A. Höpner, A. Breitschwerdt, *Adv. Solid State Phys.*, **32**, 179, (1992).

[8] L. Pavesi, *Rivista Del Nuovo Cimento*, **20**, 1, (1997).

[9] U. Gösele, V. Lehmann, *Porous Silicon*, ed. Z.C. Chen, R. Tsu, World Scientific, (1994).

[10] V. Lehmann, U. Gösele, *Appl. Phys. Lett.*, **58**, 856, (1991).

[11] St. Frohnhoff, M.G. Berger, M. Thönissen, C. Dieker, L. Vescan, H. Münder, H. Lüth, *Thin Solid Films*, **255**, 59, (1995).

[12] Y.H. Seo, K.S. Nahm, M.H. An, E-K. Suh, Y.H. Lee, K.B. Lee, *Jpn. J. Appl. Phys.*, **33**, 6425-6431, (1994).

[13] G. Lérondel, R. Romestain, S. Barret, *J. Appl. Phys.*, **81**, 6171, (1997).

[14] A.G. Cullis, L.T. Canham, P.D.J. Calcott, *J. Appl. Phys*, **82**, 910, (1997).

[15] A.G. Cullis, L.T. Canham, O.D. Dosser, in *Light Emission from Silicon*, ed. by S.S Iyer, R.T. Collins and L.T. Canham, Materials Research Society, Pittsburgh, 7, 1992.

[16] D. Bellet, G. Dolino, M. Ligeon, P. Blanc, M. Krisch, *J. Appl. Phys.*, **71**, 145, (1992).

[17] A.G. Cullis, L.T. Canham, *Nature*, **353**, 335, (1991).

[18] M.I.J. Beale, J.D. Benjamin, M.J. Uren, N.G. Chew, A.G. Cullis, *J. Cryst. Growth*, **73**, 622, (1985).

[19] V. Lehmann, *J. Electrochem. Soc.*, **140**, 2836, (1993).

[20] H.W. Lau, G.J. Parker, R. Greef, M. Holling, *Appl. Phys. Lett.*, **67**, 1877, (1995).

[21] W.K. Chang, K.K. Gleason, *J. Electrochem. Soc.,* **144**, 1441-1446, (1997).

[22] L.T. Canham, A.G. Cullis, C. Pickering, O.D. Dosser, T.I. Cox, T.P. Lynch, *Nature*, **368**, 133, (1994).

[23] L.T. Canham, *J. Appl. Phys.,* **72**, 1558, (1992).

[24] P. Gupta, V.L. Colvin, S.M. George, *Phys. Rev. B.,* ,**37**, 8234, (1988).

[25] L.T. Canham, M.R. Houlton, W.Y. Leong, C. Pickering, J.M. Keen, *J. Appl. Phys.*, **70**, 422, (1991).

[26] P.M. Fauchet, L. Tsybeskov, S.P. Duttagupta, K.D. Hirschmann, *Thin Solid Films*, **297**, 254, (1997).

[27] J.F. Harvey, M. Shen, R.A. Lux, M. Dutta, J. Pamulapti, R. Tsu, *Mater. Res. Soc. Symp. Proc.*, **256**, 175, (1992).

[28] P.D.J. Calcott, K.J. Nash, L.T. Canham, M.J. Kane, D. Brumhead, *J. Phys. C :Condens. Matter*, **5**, L91, (1993).

[29] D.T. Jiang, I. Coulthard, T.K. Sham, J.W. Lorimer, S.P. Frigo, X.H. Feng, R.A. Rosenberg, *J. Appl. Phys.*, **74**, 6335, (1993).

[30] L.T. Canham, *Phys. Stat. Sol. B*, **190**, 9, (1995).

[31] P.M. Fauchet, E. Ettedgui, A. Raisanen, L.J. Brillson, F. Seiferth, S.K. Kurinec, Y. Gao, C. Peng, L. Tsybeskov, *Mater. Res. Soc. Symp. Proc.*, **298**, 271, (1993).

[32] F. Koch, *Mater. Res. Soc. Symp.*, **298**, 319, (1993).

[33] L.T. Canham, W.Y. Leong, T.I. Cox, M.I.J. Beale, K.J. Nash, P. Calcott, D. Brumhead, L.L. Taylor, K.J. Marsh, *Proceedings of the 21st International Conference on Physics of Semiconductors*, ed. P. Jiang and H.Z. Zhang, World Scientific, 1423, (1992).

[34] V. Lehmann, H. Cerva, U. Gösele, *Mater. Res. Soc. Symp. Proc.*, **256**, 3, (1992).

[35] C. Tsai, K.H. Li, J. Sarathy, S. Shih, J.C. Campbell, B.K. Hance, J.M. White, *Appl. Phys. Lett*, **59**, 2814, (1991).

[36] M.S. Brandt, H.D. Fuchs, M. Stutzmann, J. Weber, M. Cardona, *Solid State Commun.*, **81**, 307, (1992).

[37] R.W. Fathauer, T. George, A. Ksendzov, R.P. Vasquez, *Appl. Phys. Lett.*, **60**, 995, (1992).

[38] B. Hamilton, *Semicond. Sci. Technol.*, **10**, 1187, (1995).

[39] M.I.J. Beale, N.G. Chew, M.J. Uren, A.G. Cullis, J.D. Benjamin, *Appl. Phys. Lett.*, **46**, 86, (1985).

[40] W. Theiß, *Optical Properties of Porous Silicon*, PhD thesis, (1995).

[41] C. Delerue, G. Allan, M. Lannoo, *Phys. Rev. B.*, **48**, 11024, (1993).

[42] I. Sagnes, A. Hamimaoui, G. Vincent, P.A. Badoz, *Appl. Phys. Lett.*, **62**, 1155, (1993).

[43] J. von Behren, M. Wolkin, P.M. Fauchet, Conference presentation, *Porous Semiconductors-Science and Technology*, Mallorca, (1998).

[44] H. De. Neve., R. Baets, P. Demester, P. Van. Dalle., *IEEE Photon. Tech. Lett.*, **7**, 287, (1995).

[45] L. Pavesi, C. Mazzoleni, A. Tredicucci, V. Pellegrini, *Appl. Phys. Lett.*, **67**, 3280, (1995).

[46] M. Araki, H. Koyama, N. Koshida, *Jpn. J. Appl. Phys.* ,**35**, 1041, (1996).

[47] A. Einstein, *Z. Phys.*, **18**, 121, (1917).

[48] Y. Yamamoto, S. Machida, G. Björk, *Optical and Quantum Electronics*, **24**, S215, (1992).

[49] N. Koshida, H. Koyama, *Appl. Phys. Lett.*,**60**, 347, (1992).

[50] A. Loni, A.J. Simons, T.I. Cox, P.D.J. Calcott, L.T. Canham, *Electron. Lett.*, **31**, 1288, (1995).

[51] L.T. Canham, T.I. Cox, A. Loni, A.J. Simons, *Appl. Surf. Sci.*, **102**, 436, (1996).

[52] Melles Griot Catalog, (1997-98).

[53] J. Jewell, J.P. Harbison, A. Scherer, Y.H. Lee, L.T. Florez, *IEEE J. Quan. Electron.*, **27**, 1332, (1991).

[54] P.A. Snow, E.K. Squire, P.St.J. Russell, *submitted to J. Appl. Phys.*.

[55] E. Hecht, *Optics*, Addison-Wesley Publishing Company, (1987).

[56] P. Yeh, *Optics of Layered Media*, Wiley-Interscience Publication, (1988).

[57] SEM and TEM images provided by the Defence Engineering and Research Agency, St Andrews Road, Malvern, Worcs. British Crown Copyright 1999 - DERA.

[58] M.G. Berger, C. Dieker, M. Thönissen, H. Lüth, H. Münder, W. Theiß, M. Wernke, P. Grosse, *J. Appl. Phys.*, **27**, 1333, (1994).

[59] M. Thönissen, S. Billat, M. Krüger, H. Lüth, M.G. Berger, *J. Appl. Phys.*, **80**, 2990, (1996).

[60] M. Thönissen, M.G. Berger, S. Billat, R. Arens-Fischer, M. Krüger, H. Lüth, W. Theiß, S. Hillbrich, P. Grosse, G. Lérondel, U. Frotscher, *Thin Solid Films*, **297**, 92, (1997).

[61] M. Thönissen, M.G. Berger, M. Krüger, W. Theiß, S. Hillbrich, R. Arens-Fischer, S. Billat, H. Lüth, *Mat. Res. Soc. Symp.Proc.*, **452**, 643, (1997).

[62] V.S. Lin, K. Motesharei, K-P.S. Dancil, M.J. Sailor, M.R. Ghadiri,*Science*, **278**, 840, (1997).

[63] G. Lérondel, S. Setzu, M. Thönissen, R. Romestain, *J. Imaging Science and Technology*, **41**, 468, (1997).

[64] U. Keller, G.R. Jacobovitz-Veselka, J.E. Cunningham, W.Y. Jan, B. Tell, G. Livescu, *Appl. Phys. Lett.*, **62**, 3085, (1993).

[65] H. Yokoyama, K. Nishi, T. Anan, H. Yamada, S.D. Brorson, E.P. Ippen, *Appl. Phys. Lett.*, **57**, 2814, (1990).

[66] M. Tocci, M. Scalora, M.J. Bloemer, J.P. Dowling, C.M. Bowden, *Phys. Rev. A*, **53**, 2799, (1996).

[67] G. Björk, *IEEE J. Quan. Elec.*, **30**, 2314, (1994).

[68] M. Cazzanelli, L. Pavesi, *Phys. Rev. B.*, **56**, 15264, (1997).

[69] E. Yablonovich, *J. Opt. Soc. Am. B.*, **10**, 283, (1993).

[70] P. St. J. Russell, *Physics World*, 37, (August 1992).

[71] *Handbook of Optical Constants in Solids*, ed. by E.D. Palik, Academic Press, (1991).

[72] M. Herzberger, C. Salzberg, *J. Opt. Soc. Am. A*, **52**, 420, (1962).

[73] Constants: A=3.41696, B=0.138497, C=0.013924, D=-2.09$\times 10^{-5}$, E=1.48$\times 10^{-7}$, F=0.028.

[74] O.I. Russo, *J. Electrochem. Soc.*, **127**, 953, (1980).

[75] J. Sturm, P. Grosse, W. Theiß, *J. Phys. B: Cond. Matt.*, **83**, 361, (1991).

[76] W. Theiß, in *Festkörperprobleme/Advances in Solid State Physics*, **33**, ed. R. Helbig Vieweg, Branunschweig, Wiesbaden, (1994).

[77] J.C. Maxwell-Garnet, *Philos. Trans. R. Soc.*, **203**, 385, (1904).

[78] D.A.G. Bruggeman, *Annalen der Physik*, **24**, 636, (1935).

[79] H. Looyenga, *Physica*, **31**, 401, (1965).

[80] P.St.J. Russell, T.A. Birks, F. Dominic Lloyd-Lucas, *Confined Electrons and Photons*, ed. by E. Burstein, C. Weisbuch, Plenum Press, New York, 585, (1995).

[81] B.E.A. Saleh, M.C. Teich, *Fundamentals of Photonics*, Wiley-Interscience, 316, (1991).

[82] I.H. Malitson, *J. Opt. Soc. Am.*, **55**, 1205, (1965).

[83] L. Pavesi, G. Panzarini, L.C. Andreani, *Phys. Rev. B*, **58**, 15794, (1998).

[84] G. Lérondel, P. Ferrand, R. Romestain, *Mat. Res. Soc. Symp. Proc.*, **452**, 711, (1997).

Appendix A

Description of Mathematical Symbols

A.1 Roman Characters

a_j^N	amplitude of co-sinusoidal part of f_j^N
A_i	amplitude coefficient of incident wave
A_r	amplitude coefficient of reflected wave
A_t	amplitude coefficient of transmitted wave
b_j^N	amplitude of sinusoidal part of f_j^N
c	speed of light in vacuum
c-Si	bulk crystalline silicon
$\hat{d}$	dipole moment operator
d_{cav}	physical thickness of cavity layer
d_H	physical thickness of high index layer
d_L	physical thickness of low index layer
d_j	physical thickness of layer j
d_{opt}	optical thickness of layer
d_{phys}	physical thickness of layer
e	electron charge
E	electric field
E_q	energy required by holes to penetrate from wafer into porous layer

f_j	electric (TE) or magnetic (TM) field in medium j
f_S	fraction of silicon in layer
F	cavity finesse
$g(\lambda)$	gaussian distribution for gain
g_0	gain variable
H_{int}	interaction Hamiltonian
I	irradiance
I_r	intensity of reflected wave
J	etch current density
J_{crit}	critical value of current density
k_{ex}	extinction coefficient
k_j	cartesian component of wavevector $\mathbf{k}$ $(j = x, y, z)$
L	total thickness of structure
m	integer representing mode order
M	translation matrix (over one period) between layers of medium 1
n_{cav}	refractive index of cavity layer
n_{eff}	average refractive index
n_g	gain part of refractive index
n_j	refractive index of layer j
n_{jc}	complex refractive index of layer j
n_{Si}	refractive index of silicon
n_{SiO_2}	refractive index of silica
n_H	refractive index of high index layer
n_L	refractive index of low index layer
N	integer representing Nth period in multilayer stack
N_A	Avogadro's number
p_j	wavevector component in layer j, normal to layers
$p - Si$	porous silicon
P	polarisation
r	reflectivity amplitude coefficient
r_{etch}	etch rate during layer fabrication
R	reflectivity
T	transmissivity
x	coordinate along which nothing varies in two dimensions
y	coordinate perpendicular to layer interface
y_j^N	value of y at centre of layer of index n_j in Nth period
z	coordinate parallel to layer interface

A.2 Greek Characters

α	absorption coefficient
α_r	resonator loss
β	wavevector component along layers (z direction)
β_c	coupling coefficient
δ_I	imaginary part of phase term
δ_R	real part of phase term
ϵ	dielectric function
ϵ_H	dielectric function of high index layer
ϵ_L	dielectric function of low index layer
ϵ_0	dielectric permittivity of free space
ϵ_a	dielectric function of air
ϵ_{av}	average dielectric function
ϵ_{Si}	dielectric function of Silicon
Γ_{sp}	spontaneous emission rate
η	internal luminescence efficiency
λ_B	wavelength of Bragg condition
λ_0	mean of gain distribution
Λ	stack pitch ($= d_H + d_L$)
$\hat{\mu}$	dipole moment operator of transition
ν_{FWHM}	full width half maximum of emission peak
$\Delta\nu_m$	free spectral range of cavity modes
ν_m	frequencies of allowed cavity modes
ν_{Si}	valence of electrochemical reaction
θ_c	critical angle of incidence for a multilayer mirror
ρ	density of silicon
$\rho(\omega)$	photon density of states
σ	standard deviation of gain distribution
τ_{nonrad}	non radiative recombination lifetime
τ_p	photon lifetime
τ_{rad}	radiative recombination lifetime
τ_{sp}	spontaneous emission decay time
$\omega/2\pi$	optical frequency
ξ_j	$= 1$ for TE polarised light
	$= 1/n_j$ for TM polarised light

Appendix B

Sample listing

Sample name[1]	Fabrication date	Wafer doping[2]	Structure type	Number of layers
7MO	17/10/89	p+ (0.01-0.04 Ωcm)	single layer	1
82Q	17/10/89	p- (50-130 Ωcm)	single layer	1
CLNS 138	03/03/97	p- (0.5 Ωcm)	mirror	20
CLNS 139	03/03/97	p- (0.5 Ωcm)	mirror	20
CLNS 142	03/03/97	p- (0.5 Ωcm)	mirror	20
CLNS 144	03/03/97	p- (0.5 Ωcm)	mirror	20
CLNS 145	10/03/97	p- (0.5 Ωcm)	mirror	20
CLNS 147	10/03/97	p- (0.5 Ωcm)	mirror	20
CLNS 148	10/03/97	p- (0.5 Ωcm)	mirror	10
CLNS 149	10/03/97	p- (0.5 Ωcm)	mirror	30

[1]Samples in text referred to without 'LNS' or 'LP' prefix. Numbers remain the same.
[2]The p-Si structures are formed from a 5 μm thick epitaxial layer grown above the substrate.

CLNS 150	10/03/97	p+ (0.01-0.04 Ωcm)	mirror	20
CLNS 152	18/03/97	p+ (0.01-0.04 Ωcm)	mirror	40
CLNS 153	18/03/97	p+ (0.01-0.04 Ωcm)	mirror	80
CLNS 154	18/03/97	p+ (0.01-0.04 Ωcm)	mirror	80
CLNS 155	18/03/97	p+ (0.01-0.04 Ωcm)	mirror	800
CLP +51	01/05/98	p+ (0.04-0.08 Ωcm)	mirror	26
CLP +52	01/05/98	p+ (0.04-0.08 Ωcm)	mirror	26
CLP +53	01/05/98	p+ (0.04-0.08 Ωcm)	single cavity	16/dh/5[3]
CLP +54	01/05/98	p+ (0.04-0.08 Ωcm)	double cavity	76/dh/15/dh
CLP +55	13/05/98	p+ (0.04-0.08 Ωcm)	single layer	1
CLP +56	13/05/98	p+ (0.04-0.08 Ωcm)	single layer	1
CLP +57	13/05/98	p+ (0.04-0.08 Ωcm)	unknown	unknown
CLP +58	13/05/98	p+ (0.04-0.08 Ωcm)	double cavity	13/dl/13/dl
CLP +59	13/05/98	p+ (0.04-0.08 Ωcm)	double cavity	40/dl/41/dl
CLP +60	29/05/98	p+ (0.04-0.08 Ωcm)	single layer	1
CLP +61	29/05/98	p+ (0.04-0.08 Ωcm)	double cavity	13/dl/13/dl/13/dl
CLP +62	29/05/98	p+ (0.04-0.08 Ωcm)	double cavity	24/dl/25/dl/24/dl

[3]Represents number of repeats top mirror /defect (dh=low index, dh=high index)/ number of repeats bottom mirror.

Appendix C

Transfer Matrix Elements

The matrix $M_{s_{21}}$ relating the field in the 2nd layer to the field in the first layer of period N is:

$$\begin{pmatrix} a_2^N \\ b_2^N \end{pmatrix} = M_{s_{21}} \begin{pmatrix} a_1^N \\ b_1^N \end{pmatrix} = \begin{pmatrix} M_{11} & M_{12} \\ M_{21} & M_{22} \end{pmatrix} \begin{pmatrix} a_1^N \\ b_1^N \end{pmatrix}, \tag{C.1}$$

where:

$$\begin{aligned} M_{11} &= c_1 c_2 - (\xi_1 p_1 \Lambda / \xi_2 p_2 \Lambda) s_1 s_2, \\ M_{12} &= s_1 c_2 / (\xi_1 p_1 \Lambda) + c_1 s_2 / (\xi_2 p_2 \Lambda), \\ M_{21} &= -\xi_1 p_1 \Lambda s_1 c_2 - \xi_2 p_2 \Lambda c_1 s_2, \\ M_{22} &= c_1 c_2 - (\xi_2 p_2 \Lambda / \xi_1 p_1 \Lambda) s_1 s_2, \end{aligned} \tag{C.2}$$

and the terms s_j and c_j are shorthand for:

$$c_j = \cos(p_j d_j/2), \;\; s_j = \sin(p_j d_j/2)(j = 1, 2).$$

The matrix $M_{s_{12}}$ which relates the field in the 1st layer of the $(N+1)th$ period to the field in the second layer of the Nth period is written,

$$\begin{pmatrix} a_1^{N+1} \\ b_1^{N+1} \end{pmatrix} = M_{s_{12}} \begin{pmatrix} a_2^N \\ b_2^N \end{pmatrix} = \begin{pmatrix} M_{22} & M_{12} \\ M_{21} & M_{11} \end{pmatrix} \begin{pmatrix} a_2^N \\ b_2^N \end{pmatrix}. \tag{C.3}$$

Thus, the translation matrix M can be used to relate the field between two layers of refractive index n_1 where,

$$\begin{pmatrix} a_1^{N+1} \\ b_1^{N+1} \end{pmatrix} = M \begin{pmatrix} a_1^N \\ b_1^N \end{pmatrix} = M_{s_{12}} M_{s_{21}} \begin{pmatrix} a_1^N \\ b_1^N \end{pmatrix}. \tag{C.4}$$

Alternatively, M can relate the fields between layers of index n_2 where $M = M_{s_{21}} M_{s_{12}}$.

The matrix M_a relates the field between the incident medium and top layer of the multilayer stack, where

$$\begin{pmatrix} A_I \\ A_R \end{pmatrix} = M_a \begin{pmatrix} a_1^1 \\ b_1^1 \end{pmatrix} = \begin{pmatrix} M_{a_{11}} & M_{a_{12}} \\ M_{a_{21}} & M_{a_{22}} \end{pmatrix} \cdot \begin{pmatrix} a_1^1 \\ b_1^1 \end{pmatrix} \tag{C.5}$$

The matrix elements are:

$$\begin{aligned} M_{a_{11}} &= \frac{1}{2}[c_1 - (\xi_1 p_1 \Lambda / i\xi_a p_a \Lambda) s_1], \\ M_{a_{12}} &= -\frac{1}{2}[s_1/\xi_1 p_1 \Lambda + c_1/\xi_a p_a \Lambda], \\ M_{a_{21}} &= \frac{1}{2}[c_1 + (\xi_1 p_1 \Lambda / i\xi_a p_a \Lambda) s_1], \\ M_{a_{22}} &= -\frac{1}{2}[s_1/\xi_1 p_1 \Lambda - c_1/\xi a p_a \Lambda]. \end{aligned} \tag{C.6}$$

The matrix M_e relates the field between the final layer of the multilayer stack and the exit medium where,

$$\begin{pmatrix} A_{I_2} \\ A_T \end{pmatrix} = M_e \begin{pmatrix} a_2^N \\ b_2^N \end{pmatrix} = \begin{pmatrix} M_{e11} & M_{e12} \\ M_{e21} & M_{e22} \end{pmatrix} \begin{pmatrix} a_2^N \\ b_2^N \end{pmatrix}. \tag{C.7}$$

The matrix elements are:

$$\begin{aligned} M_{e11} &= c_2 + i\xi_s p_s \Lambda / \xi_2 p_2 \Lambda s_2, \\ M_{e12} &= c_2 - i\xi_s p_s \Lambda / \xi_2 p_2 \Lambda s_2, \\ M_{e21} &= \xi_2 p_2 \Lambda s_2 - i\xi_s p_s \Lambda c_2, \\ M_{e22} &= \xi_2 p_2 \Lambda s_2 + i\xi_s p_s \Lambda c_2. \end{aligned}$$

Appendix D

Deposition Conditions for Hydrogenated Amorphous Silicon/Silica Multilayer Structure

	$SiO_x : H$	$a - Si : H$
target	fused silica	non-doped Si
sputtering gas pressure (mTorr)	2.0	3.6
gas flow ratio		
total (sccm)	80	80
$H_2/(Ar + H_2)$ (%)	15	5
rf power (W)	400	400
layer thickness (nm)	304	12
substrate temperature (C)	180	180
number of layers	40	40
refractive index (@1.55 μm)	1.49	3.24